Dissertation
submitted to the
Combined Faculties for the Natural Sciences and for Mathematics
of the Ruperto-Carola University of Heidelberg, Germany
for the degree of
Doctor of Natural Sciences

put forward by
Dipl.-Phys. Nils Krah
born in Bremen

Date of oral examination: 08.05.2014

Visualization of air and water-sided concentration profiles in laboratory gas exchange experiments

Referees:
Prof. Dr. Bernd Jähne
Prof. Dr. Kurt Roth

Abstract

In this work, the transport of a tracer gas from air into water is studied experimentally under turbulent, wavy conditions imposed by a unidirectional wind field in a laboratory flume. To this end, a technique based on laser induced fluorescence recorded with cameras is developed to visualize the spatial tracer distribution in both phases simultaneously. Dedicated image processing procedures are developed to determine statistically averaged vertical profiles of absolute concentration in coordinates relative to the wavy water surface. A thorough characterization of the technique in terms of systematic errors is presented and a simple method to estimate the vertical probability distribution of turbulent eddies in water is proposed. Invasion experiments are performed in which supersaturation of acetone in the flume's air compartment is imposed giving rise to a vertical flux into the water. The equivalence of momentum and mass transport in air, presumed by many theoretical descriptions, is confirmed experimentally by comparing characteristic scaling properties of wind and concentration profiles. Results also suggest that surfactants suppress gas exchange by modifying the water-sided boundary conditions and altering the turbulent water flow close to the surface regardless of the wind regime. Furthermore, observed discontinuity of complete air-water concentration profiles leads to the hypothesis that kinetic processes on molecular scale at the interface must be considered additionally to fluid mechanical descriptions.

Zusammenfassung

In dieser Arbeit wird der Transport eines Spurenstoffgases von Luft in Wasser experimentell untersucht. Dazu werden in einem Windkanal Turbulenz und Wellen durch ein gerichtetes Windfeld erzeugt. Es wird insbesondere eine Technik zur gleichzeitigen bildhaften Darstellung der räumlichen Spurengasverteilung in beiden Phasen entwickelt, die auf dem Prinzip der laserinduzierten Fluoreszenz beruht, die von Kameras aufgenommen wird. Spezielle Bildverarbeitungsprozeduren werden entwickelt, um statistisch gemittelte vertikale Profile absoluter Konzentrationen in Koordinaten relativ zur welligen Wasseroberfläche zu bestimmen. Eine gründliche Charakterisierung der Technik in Bezug auf systematische Fehler wird vorgestellt und eine einfache Methode wird vorgeschlagen, um die vertikale Wahrscheinlichkeitsverteilung turbulenter Eddies im Wasser zu schätzen. In Invasionsexperimenten wird eine erhöhte Acetonkonzentration im Luftraum des Windkanals und dadurch ein Massenfluss ins Wasser erzeugt. Die Gleichwertigkeit von Impuls- und Massentransport in der Luft, die vielen theoretischen Beschreibungen als Annahme zugrunde liegt, wird bestätigt durch den experimentellen Vergleich der Skalierungseigenschaften von Wind- und Konzentrationsprofilen. Ergebnisse legen zudem nahe, dass oberflächenaktive Substanzen Gasaustausch unterdrücken, indem sie die wasserseitigen Randbedingungen und dadurch den turbulenten Fluss nahe der Oberfläche verändern, unabhängig vom Windstärkenbereich. Weiterhin führt die beobachtete Diskontinuität der vollständigen Luft-Wasser Konzentrationsprofile zur Hypothese, dass kinetische Prozesse auf molekularer Skala zusätzlich zu fluidmechanischen Beschreibungen beachtet werden müssen.

Contents

1

Introduction

1.1 Scientific context

System earth can be thought of as a set of interconnected compartments (e.g. atmosphere, ocean), containing various species of chemical substances. Some are produced naturally in the biosphere, some photochemically, others are of anthropogenic origin. Chemical reactions might cause depletion, creation, or conversion from one substances into another. Specific for each compartment, transport processes lead to a redistribution of matter, typically following the overall concentration gradient. Of importance for environmental mass budges is the flux across the interfaces which divide the compartments. The ocean assumes particular relevance as a huge reservoir acting as a sink or source (*Takahashi et al.*, 2009). For example, it takes up e.g. 30 to 40 % of the CO_2 originating from fossil fuel combustion (*Donelan and Wanninkhof*, 2002). The interface dividing atmosphere and ocean is obviously the water surface. Since it is virtually impossible to directly monitor fluxes globally and continuously, it is of interest to establish relationships with other easier to measure parameters. This has been topic of research for the past decades and continues to be.

The water surface acts as a phase boundary both in thermodynamic and fluid mechanical sense. For the transport of a substance from the ocean to the atmosphere or vice versa, thermodynamics describe the processes at the interface. Gas exchange eventually implies evaporation or condensation, respectively, leading to dependences e.g. on temperature, pressure, humidity. Within the fluid, mass is transported by molecular diffusion and by advection. Fluid mechanically, the surface constrains air and water flow, leading to a suppression of turbulence in proximity to the interface. For this reason, the otherwise comparatively inefficient diffusion becomes relevant very close to the phase boundary. To parametrize gas exchange across the ocean's surface, it is desirable to identify transport mechanisms and suitable measurable quantities which describe them.

Leaving aside heat-induced buoyancy, wind is the major source of mechanical forcing on the open ocean. In coastal regions, additional phenomena such as upwelling may play a role. Naturally, wind speed emerges as possible parameter describing the driving force. At low wind speeds, momentum transfer from the air flow into the water occurs by means of shear stress at the surface, motivating the so-called friction velocity as another characteristic parameter. For higher wind speed, some studies suggest an enhancement of gas transfer due to the presence of waves, where presumably the high frequency portion of the spectrum is most relevant (*Bock et al.*, 1999; *Jähne et al.*, 1984). The formation waves might indeed lead to flow structures too complex to be described as a unidirectional shear flow and consequently, neither wind speed nor friction velocity are adequate universal parameters. Under very energetic conditions, breaking waves and the associated white capping and bubbles open yet another transport channel, and similarly, rain is believed to have an impact on gas exchange (*Wanninkhof et al.*, 2009).

Experimental studies have shown that naturally occurring surface active material, e.g. originating from phytoplankton, interferes with the fluid mechanical interaction between wind and water at the surface, possibly by altering the fluid mechanical boundary conditions, leading to a suppression of small scale waves (ripples) and mass transfer rates (e.g. *Broecker et al.*, 1978; *Frew et al.*, 1990; *Hühnerfuss et al.*, 1987; *Lucassen*, 1982; *McKenna and Bock*, 2006). This has also lead to speculations whether wave attenuation is the cause for reduced gas exchange or whether both are independent symptoms of the modified surface dynamics (*Frew et al.*, 2004). In any case, the effect of surfactants is not captured by either of the above mentioned parameters.

1.2 Overview of previous studies

Research activity in the last decades has spanned quite a vast gamma of methodical approaches. Numerous field campaigns, most of them ship-based and some from platforms, have produced a great amount of empirically measured transfer rates for different types of gases, (e.g. *Frew et al.*, 2004; *Ho et al.*, 2006, 2011; *Nightingale et al.*, 2000a,b; *Wanninkhof and McGillis*, 1999), to name only a few. Partly due to low fluxes and cumbersome instrumentation, statistical scatter is rather prominent, as seen from the exemplary plot in Fig. 1.1. For this reason it is intricate to formulate quantitative relationships among parameters in a deductive way. Most empirical parametrizations are based on a power law dependence of transfer velocity and wind speed (*Ho et al.*, 2006; *Nightingale et al.*, 2000b; *Wanninkhof*, 1992; *Wanninkhof et al.*, 2009), others use sub-regimes based on wind conditions (*Liss and Merlivat*, 1986). Some techniques estimate the gas flux from measurements in the air by exploiting scaling properties of the turbulent airflow and the conceptual analogy between

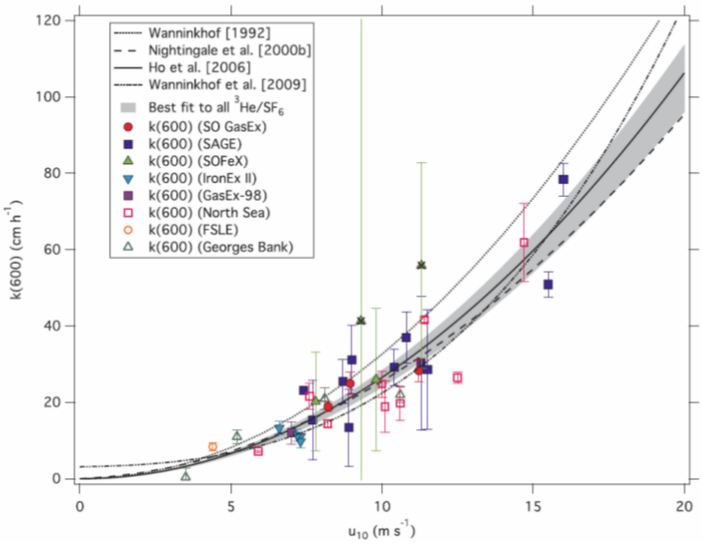

Figure 1.1 Exemplary plot of transfer velocities measured in field campaigns, depicted as a function of wind speed. Empirical parametrizations are shown as lines. The figure is taken from *Ho et al.* (2011).

momentum and mass transport (*Edson et al.*, 2004; *McGillis et al.*, 2001; *Roether*, 1983). The integrity of this approach has been verified by comparing results with mass fluxes obtained through independent complementary methods. To my best knowledge, however, the analogy of concentration and wind profiles, especially very close to the water surface, has not yet been directly investigated experimentally.

Another broad methodical field comprises studies of gas exchange in wind-water tunnels (*Alaee et al.*, 1995; *Broecker et al.*, 1978; *de Leeuw et al.*, 2002; *Frew et al.*, 1995; *Jähne*, 1985; *Jähne et al.*, 1987; *McGillis et al.*, 2000; *Ocampo-Torres et al.*, 1994). While certainly idealizing the complex variable conditions encountered on the ocean, such laboratory experiments allow to actively monitor and control parameters like wind speed, additional mechanical wave forcing, fetch (i.e. interaction length between wind and water), and not the least the presence or not of surface films. Instrumentation is considerably easier to deploy than on a ship.

Advances in digital camera technology have brought about an increased use of visualization techniques in laboratory and field experiments. A series of studies have focused on the small scale distribution of deliberately injected tracer gases in the uppermost centimeters below the water surface (e.g. *Duke and Hanratty*, 1995; *Friedl*, 2013; *Herlina and Jirka*, 2008; *Janzen et al.*, 2010; *Jirka et al.*, 2010; *Münsterer and Jähne*, 1998; *Schulz and Janzen*, 2009; *Woodrow and Duke*, 2001). In some cases, turbulence was created by wind forcing, in others through stirring of the water body. The effect of surfactants was explicitly investigated by *Frew* (1997); *Lee et al.* (1980); *McKenna and McGillis* (2004). Visualization techniques have also allowed to study geometrical and dynamical features of wind-induced wave fields (*Balschbach*, 2000; *Jähne and Riemer*, 1990; *Rocholz*, 2008), turbulent structures underneath waves (e.g. *Siddiqui et al.*, 2001, 2002) and on the surface (*McKenna and McGillis*, 2004).

Experimental studies have been complemented by direct numerical simulation (DNS) (*Shen et al.*, 2000; *Sullivan et al.*, 2000; *Tsai and Hung*, 2007; *Tsai*, 2001;

Tsai et al., 2013), and finally, a number of theoretical models have been proposed attempting to describe air-sea gas exchange from first principles. I will explain some of them in sec. 2.4.

1.3 Scope of this thesis

Within the spectrum of existing investigations on the matter of gas exchange, this thesis is placed among visualization based laboratory experiments. Different from previous studies, processes underlying the vertical mass transport in the air are of central interest. The scope of this thesis is therefore the development and optimization of an experimental technique to investigate the spatial distribution of a tracer gas in the turbulent airflow above the wind-driven wavy water surface. Initial efforts have already been undertaken by *Winter* (2011).

In this thesis, the technique is applied in wind tunnel experiments which allow to validate the developed methods. The purpose of these experiments is to record statistically averaged concentration profiles in the air and to analyze them in terms of analogy between mass and momentum transport.

The technique is extended to simultaneously visualize the distribution of a tracer gas in the water. The goal is to study the partitioning of transfer resistance across the interface (i.e. the macroscopic parameter describing the effectiveness of vertical mass transport from one compartment into the other) for different wind forcing conditions. In this context, also the effect of surfactants on the gas transfer is of interest.

The experimental results will also allow to deduce transfer coefficients for the used tracer gas, acetone, as a function of wind speed and friction velocity. It is stressed here, however, that the scope is not to provide empirical data to be transfered easily to field conditions, although this might be possible.

Other works have focused on the validation of specific transport models based on mean vertical concentration profiles in the water (*Friedl*, 2013; *Münsterer and Jähne*, 1998). This is not the scope of this thesis. Instead, characteristic physical parameters are used as phenomenological indication on the relevance of physical processes and their dependence on experimental conditions such as wind forcing and surface active material.

1.4 Structure of the thesis

This thesis is organized as follows:

- In chap. 2, I explain the basic physical notions and concepts necessary to describe the studied phenomena. In particular, I will outline the analogy between momentum and mass transport in boundary layer theory and I will elaborate the different scales relevant in water and air.

- Chapter 3 is dedicated to the employed visualization technique. Basic principles of laser induced fluorescence (LIF), the choice of tracer, and how concentration profiles are obtained from fluorescent brightness images are explained.

- Chapter 4 focuses on the technical aspects of the experimental set-up, i.e. the wind-wave tank, the main components, and their deployment. I also present a theoretical analysis of the optical effects at the water surface and their implications on the recorded concentration profiles.

- In chap. 5, I summarize a series of complementary experiments (and their results) conducted to characterize the wind and wave field and the pulsed laser system used in this work.

- The experimental procedures are explained in chap. 6.

- Chapter 7 summarizes the data processing approaches used to retrieve concentration profiles from recorded images and to convert them to absolute concentrations. I also explain how transfer velocities are calculated based on mass balance considerations and how streaks in the water are used to obtain an estimate on the vertical distribution of turbulent eddies.

- Chapter 8 presents the results of visualization experiments at a wind-wave tank on the invasion process of acetone from air into water.

- In chap. 9, I discuss three major aspects that emerged from the experimental results.

2

Theory

In this chapter, I will collect and describe the basic notions necessary to theoretically treat the transport of a passive admixture such as a gas in a turbulently mixed medium. Since this thesis deals with the processes occurring in close proximity to the air-water interface, the concept of a boundary layer, initially proposed by Ludwig Prandtl, is useful. The intention is not to give a comprehensive review of this certainly vast field and for more detailed explanations and derivations, I refer to common textbooks such as *Kundu* (2008); *Monin and Yaglom* (2007); *Schlichting* (2000).

I will further provide an overview over models used to describe gas exchange from a small-scale point of view and the different boundary conditions at the interface applicable to the air and water flow, respectively. Finally, I will quickly describe the conceptual influence of surface active material on gas exchange and the partitioning of transport resistances among the gaseous and aqueous phase according to the solubility of a gas.

Different terms are found in literature dealing with the transport of a gaseous substance in a fluid and through the phase boundary. These are gas exchange, gas transfer, mass transfer, mass transport. I will use them interchangeably throughout this thesis.

2.1 Basic fluid mechanical equations

In a Eulerian frame, a fluid flow is characterized by the velocity field $\vec{u}$ and the density ρ. For the frequency of pressure fluctuations occurring under realistic environmental conditions, e.g. on the ocean, both air and water can be treated as incompressible. In this case, the continuity equation reads

$$\nabla \cdot \vec{u} = 0, \tag{2.1}$$

It should be noted that close to a boundary, two-dimensional divergence can still occur and is indeed considered by some gas exchange models to be the principle transport mechanism.

The intermolecular forces on scales smaller than those considered in the continuum picture of fluid mechanics are described by the stress tensor,

$$\tau_{ij} = \underbrace{\mu \left(\frac{\partial u_i}{\partial x_j} + \frac{\partial u_j}{\partial x_i} \right)}_{\equiv \sigma_{ij}} - p\delta_{ij}. \tag{2.2}$$

Here, p is the normal pressure, μ the material specific viscosity, and σ_{ij} the viscous stress. Note that this is valid for air and water given their Newtonian nature. The stress is typically used as boundary condition at the surface, as will be explained in sec. 2.2.3.

Conservation of momentum in an incompressible fluid is described by the Navier-Stokes equation

$$\frac{\partial \vec{u}}{\partial t} + (\vec{u} \cdot \nabla)\,\vec{u} = -\frac{\nabla p}{\rho} + \vec{g} + \nu \Delta \vec{u}, \tag{2.3}$$

where $\nu \equiv \mu/\rho$ is the kinematic viscosity and g_i summarize the external forces. A characteristic number associated with this equation is the Reynolds number, $\mathrm{Re} \equiv UL/\nu$, where U and L are typical velocity and length scales of the considered flow. The Reynolds number quantifies the ratio of inertial to viscous forces.

Transport of a passive admixture, in this work a tracer gas, is described by the diffusion-advection equation,

$$\frac{\partial c}{\partial t} + \vec{u} \nabla c = \mathrm{D} \Delta c, \tag{2.4}$$

where D is the diffusion coefficient in the corresponding medium. As unit for the concentration, I use mol/L. Knowledge of the flow field $\vec{u}$ is necessary to describe the transport of a tracer in the fluid.

Viscous dissipation of momentum and diffusive dilution both refer to small scale processes. The ratio of the related coefficients in eq. (2.3) and eq. (2.4) is defined as the Schmidt number $\mathrm{Sc} \equiv \nu/\mathrm{D}$. For most gases in the air, it is of order 1 while in the water, it is typically of order 1000.

2.1.1 Reynolds decomposition

In a turbulent flow, the quantities $\vec{u}(\vec{x},t)$ and $c(\vec{x},t)$ will fluctuate in time when observed at a fixed point in space. Under stationary conditions and after sufficiently long observation, it should be possible to establish mean values $\langle\vec{u}\rangle(\vec{x})$ and $\langle c\rangle(\vec{x})$, characteristic e.g. for the distance to the fluid boundary such as the air-water interface. This motivates to separate the variables in a mean and a fluctuating contribution,

$$\vec{u} = \langle\vec{u}\rangle + \vec{u}' \tag{2.5}$$

$$c = \langle c\rangle + c', \tag{2.6}$$

In a strict sense, $\langle . \rangle$ denotes the average over all realizations in the statistical ensemble describing the stationary flow. By the ergodic principle, it is practically calculated by averaging over sufficiently long time periods. It should be noted that continuity is fulfilled also by the fluctuating term, i.e. $\nabla \cdot \vec{u}' = 0$. If the fluctuating component cannot be resolved in time technically, the mean term can still provide insight into relevant mechanisms. Indeed, this work deals with the visualization of mean concentration profiles.

2.1.2 Averaged equations

The Reynolds decomposition can be inserted in eq. (2.3) and eq. (2.4) and the average over all terms can be taken. This results in equations describing the mean velocity and concentration fields. The straight forward calculation can be found in all of the textbooks cited above. The resulting expressions in indexed notation are

$$\frac{\partial\langle u_i\rangle}{\partial t} + (\langle u_i\rangle \cdot \nabla)\langle u_i\rangle = -\frac{\nabla\langle p\rangle}{\rho} + g_i + \nu\Delta\langle u_i\rangle - \frac{\partial}{\partial x_j}\langle u_i' u_j'\rangle \tag{2.7}$$

$$\frac{\partial\langle c\rangle}{\partial t} + \langle\vec{u}\rangle\nabla\langle c\rangle = \mathrm{D}\Delta\langle c\rangle - \nabla\langle\vec{u}'c'\rangle = \nabla\left(\mathrm{D}\nabla\langle c\rangle - \langle\vec{u}'c'\rangle\right). \tag{2.8}$$

Einstein's convention for summing equal indices is intended. The additional term $\langle u_i' u_j'\rangle$ is often called turbulent Reynolds stress. Henceforth, I will simply denote the average quantities by $\vec{u}$ and c for the sake of notational simplicity.

2.1.3 Vertical transport equations

In certain situations, statistical homogeneity in the two lateral dimensions (x,y) can be assumed, i.e. $\partial/\partial x = 0$ and $\partial/\partial y = 0$, and the above equations simplify. In a unidirectional wind field (in x-direction), like in a linear wind-wave tank, the x-component of the mean velocity field u_x is of interest. The average vertical component, u_z, must be zero on the other hand. Similarly, if a macroscopic concentration gradient between the air and water compartment is imposed, e.g. by deliberately injecting a tracer gas, this will result in a vertical flux into the water. In the absence of pressure gradients and external forces, the following two expressions are obtained,

$$\frac{\partial u_x}{\partial t} = \frac{\partial}{\partial z}\left(\nu\frac{\partial u_x}{\partial z} - \langle u'_x u'_z\rangle\right) \tag{2.9}$$

$$\frac{\partial c}{\partial t} = \frac{\partial}{\partial z}\left(\mathrm{D}\frac{\partial c}{\partial z} - \langle u'_z c'\rangle\right). \tag{2.10}$$

Under stationary conditions, the time derivative is zero giving rise to expressions for the momentum and mass flux, respectively. I will, henceforth, adopt the notational convention in literature on gas exchange by which the horizontal and vertical velocity components are denoted by u and w, respectively.

$$\tau/\rho = -\nu\frac{\partial u}{\partial z} + \langle u'w'\rangle \tag{2.11}$$

$$j_m = -\mathrm{D}\frac{\partial c}{\partial z} + \langle w'c'\rangle. \tag{2.12}$$

The second terms on the RHS are the turbulent contribution to mass and momentum flux. Since they are associated to turbulent eddies, they are often called eddy covariance. Some experimental techniques seek to directly determine their value by measuring air flow and concentration at sufficiently high time resolution. A theoretical approach is to relate the covariance terms to mean quantities, thereby modeling the turbulent transport. I will explain this in more detail in sec. 2.2.2 and sec. 2.4.1.

2.2 Turbulent boundary layer

In high Reynolds number flows viscosity is negligible compared to inertial forces. On the other hand, Ludwig Prandtl showed back in 1905 that experimental findings on drag coefficients of solid objects could only be reconciled if a no-slip boundary condition was insisted on. Forcing the tangential velocity on a confining surface to zero leads to strong gradients and thus to non-negligible viscous forces in proximity of a boundary. This gives rise to the concept of a boundary layer, which is thin compared to other scales of the flow and within which forces are to be considered which are negligible otherwise.

A case relevant for this work in which boundary layer flow occurs is the unidirectional airflow in a wind-wave tank. The water surface is in good approximation rigid as timescales of deformation are much larger than those of the airflow. I will not go through all derivations which can be found e.g. in *Monin and Yaglom* (2007), but only state phenomenologically relevant facts as well as some formulæ.

2.2.1 Sublayers and scales

The turbulent boundary layer of a flow close to a smooth wall is subdivided into three distinct regimes: the viscous sublayer, the logarithmic sublayer, and the outer layer. Its overall thickness is given by δ.

Very close to the surface, viscous forces prevail, momentum flux is constant and according to eq. (2.11) the wind profile is linear. A characteristic velocity scale is given by the surface stress, i.e. momentum flux,

$$\tau_\mathrm{s} \equiv \rho u_*^2, \tag{2.13}$$

and together with the kinematic viscosity, this provides a characteristic length scale $^{\nu}/_{u_*}$, based on which the non-dimensional wall-coordinate is defined,

$$z^+ \equiv \frac{z u_*}{\nu}. \tag{2.14}$$

Note that this is conceptually a Reynolds number, but it does not describe the free flow. The viscous sublayer is found experimentally to extend to $z^+ = 11$. The term u_* is called friction velocity and can be determined from wind profiles (see sec. 5.1). It may be related to the water-sided equivalent value assuming continuity of momentum flux across the phase boundary, i.e.

$$\rho_\mathrm{water} u_{*\mathrm{water}}^2 = \rho_\mathrm{air} u_{*\mathrm{air}}^2 \quad \Rightarrow \quad u_{*\mathrm{air}} = u_{*\mathrm{water}} \sqrt{\frac{\rho_\mathrm{air}}{\rho_\mathrm{water}}}. \tag{2.15}$$

I used this scaling whenever water-sided friction velocities were needed. Of course it could also be measured directly from water-sided flow profiles, e.g. by particle imaging velocimetry (PIV), or by momentum budget considerations (*Bopp*, 2011), but that was not scope of this work.

Outside the viscous sublayer, dimensional analysis shows that the gradient of the mean velocity is proportional to u_*/z, leading to a logarithmic profile[1],

$$u(z) = \frac{u_*}{\kappa} \log z + C, \tag{2.16}$$

where κ and C are constants which were determined experimentally and are available

---

[1] I use log for the natural logarithm throughout this thesis, as common in mathematical notation.

as literature values.

The logarithmic sublayer is found experimental to extend to $0.15 \cdot \delta$. Yet above, the so-called outer layer is identified. No closed theoretical formulation for its shape has been found so far, but it has been confirmed experimentally that velocity profiles are self-similar. An empirical formula is proposed for example by *Hama* (1954),

$$U_0 - u(z) = B\,(z - \delta)^2 . \tag{2.17}$$

The parameter δ quantifies the overall thickness of the turbulent boundary layer. I used this expression to fit wind profiles (see sec. 5.1).

2.2.2 Turbulent viscosity

The term $\rho \cdot \langle u'w' \rangle$ in eq. (2.11) can be interpreted as turbulent contribution to the vertical momentum flux. Indeed, only if positive horizontal velocities u' appear prevalently in correlation with negative vertical velocities w', this results in a net downward flux. Often, the approach is to express the turbulent momentum transport in terms of mean quantities of the flow. In the turbulent viscosity approach, $\langle u'w' \rangle$ is expressed as the product of the gradient of the mean horizontal velocity profile and a height-dependent turbulent viscosity,

$$\rho \langle u'w' \rangle = \rho K_{\text{turb}}(z) \cdot \frac{\partial \bar{u}}{\partial z}. \tag{2.18}$$

The function $K_{\text{turb}}(z)$ was modeled for a turbulent pipe flow a long time ago by *Reichardt* (1951). Because it is relevant for my thesis, I give a short summary of the concepts here. In his analysis, he uses dimensionless coordinates, scaled with the viscous length, i.e. $z^+ = {}^{z u_*}/_{\nu}$. Very close to the smooth surface, turbulence should be negligible and viscosity is the only mechanism of momentum transport, i.e. $K_{\text{turb}}(z^+) + \nu \to \nu$ for $z^+ \to 0$. Further away from the surface, $K_{\text{turb}}(z)$ should assume a form such to reproduce the logarithmic velocity profile of eq. (2.16), i.e.

$$K_{\text{turb}}(z^+)/\nu = \kappa z^+ . \tag{2.19}$$

Reichardt proposes a parametrization that interpolates between both forms, given a certain scale z_ℓ^+,

$$\frac{K_{\text{turb}}(z^+) + \nu}{\nu} = 1 + \kappa \left(z^+ - z_\ell^+ \tanh\left(\frac{z^+}{z_\ell^+} \right) \right). \tag{2.20}$$

For small z^+, the hyperbolic tangent decays linearly so that the second term becomes zero, just as required. For large z^+, the linear term dominates, reproducing the logarithmic shape upon integration. The parameter z_ℓ^+ was determined experimentally to be ≈ 11 and describes the scale of transition between the viscous and the logarithmic sublayer.

Under stationary conditions, momentum flux τ is independent of height and may in particular be taken as the flux at the surface τ_s. The velocity profile can be recovered from eq. (2.20) upon integration, following eq. (2.18) and eq. (2.11),

$$\bar{u}(z^+) = \frac{\tau_s}{\rho u_*} \int_0^{z^+} \frac{\nu}{\nu + K_{\text{turb}}(z^+)} dz^+. \tag{2.21}$$

Using the definition of $z^+ = {}^{zu_*}/_{\nu}$, this can also be written in dimensional form as

$$\bar{u}(z) = \frac{\tau_s}{\rho \nu} \int_0^{z} \frac{\nu}{\nu + K_{\text{turb}}(z)} dz. \tag{2.22}$$

2.2.3 Boundary conditions and surfactants

When describing the fluid flow theoretically or by means of DNS, certain assumptions about the boundary conditions must be made. I will not discuss the ample question in all its completeness, but collect some conceptually important arguments and refer to the free and the rigid boundary as two limiting cases. Here, the phase boundary is always the air-water interface. General explanations are found in textbooks on fluid mechanics, cited above, and also in publications related to gas exchange which I cite where appropriate.

For flat water, the surface is usually set to $z = 0$. In the presence of waves, the water height is a function of space and time, $\eta(x, y, t)$, and the boundary conditions have to hold on $z = \eta$. Some authors use curvilinear, locally orthogonal coordinates relative to the water surface (see e.g. *Sullivan et al.*, 2000; *Troitskaya et al.*, 2010; *Tsai and Hung*, 2007; *Tsai et al.*, 2013), others linearize and apply boundary conditions anyhow at $z = 0$ (see e.g. *Coantic*, 1986; *Shen et al.*, 2000; *Tsai*, 1996).

Kinematic boundary conditions concern the value of the three velocity components at the water surface. For a non disrupted water surface, it is commonly assumed that the vertical component w of the flow be zero at $z = \eta$. The no-slip condition, already mentioned in sec. 2.2, also requires u and v to be zero everywhere. Consequently, also the derivatives ${}^{\partial u}/_{\partial x} = 0$ and ${}^{\partial v}/_{\partial y} = 0$ have to vanish, and by the continuity eq. (2.1), also the gradient of the vertical component, ${}^{\partial w}/_{\partial z} = 0$. As a result, divergence and convergence are suppressed close to the surface. This is a valid approach for air above the water since the latter has much higher density and thus inertia. From the point of view of the water, the air is much less dense and does not create inertial resistance upon tangential replacement of water parcels at the surface. In this case, u and v are generally not zero at $z = \eta$ and the same geometric interface does not pose rigid wall conditions on the water.

Secondly, dynamic boundary conditions require equilibrium of stress (forces) at the surface. According to eq. (2.2), this poses conditions on the derivatives of the velocity field at the surface. For a body of free water, no external forces act so that the components of the internal viscous stress have to vanish at $z = \eta$ (see e.g. *Shen et al.*, 2000). Over a wind-driven surface, they have to equilibrate those imposed by the wind field, which in turn depend on the surface shape and dynamics. In principle, the full coupled system of air and water flow would have to be solved. In DNS like the one of *Tsai and Hung* (2007), an empirically motivated modulation of the wind stress along the phase of the most prominent wave component is used.

Surface active material modifies the surface tension of clean water, σ_0, by an additional term σ, i.e. $\Pi = \sigma_0 - \sigma$. The exact chemico-mechanical understanding for many substances is still field of active research. Generally, the surfactant-induced tension σ depends on the local structure of the surface film. In a simple visco-elastic approach, used e.g. by *McKenna and McGillis* (2004) and *Tsai* (1996), a so-called Marangoni stress is deduced from horizontal gradients in the surface tension, much like a dilated or compressed spring. This has to locally match the shear stress in the fluid,

$$\mu \frac{\partial u}{\partial z} = \frac{\partial \sigma}{\partial x}. \tag{2.23}$$

McKenna and McGillis (2004) provide good explanations of the involved effects. Conceptually, surface tension gradients counteract tangential displacement in the fluid and thereby immobilize the water, leading to a reduction of divergence and vorticity close to the surface. In this sense, surfactant covered water resembles a rigid wall. Examples of experimental studies regarding the effect of surface films on the turbulent flow structure are (*Hirsa et al.*, 1995; *Lapham et al.*, 2001; *McKenna and McGillis*, 2004). DNS have been performed by *Tsai* (1996). The modified and reduced surface tension also leads to a suppression of small-scale waves, or ripples. This has been studied by many investigators, e.g. by *Asaki et al.* (1995); *Frew et al.* (1995); *Wu* (1989)

2.3 Transfer resistance and transfer velocity

The mass flux j across the air-water interface depends on the macroscopic concentration difference Δc. It is therefore natural to introduce a specific flux,

$$k \equiv \frac{j}{\Delta c}. \tag{2.24}$$

Since it has the units of length over time, it is commonly called transfer velocity. Its inverse is referred to as transfer resistance,

$$R \equiv \frac{1}{k}. \tag{2.25}$$

The fluids on either side of the phase boundary pose a certain resistance to a scalar quantity transported from the air-sided to the water-sided well-mixed bulk, or vice-versa, much in the same way as a solid body creates resistance to heat transfer or a wire to electric current. Indeed, the latter example provides a good analogy that I will lean upon in the following to summarize the concept of gas transfer resistance.

According to Ohm's law, a potential difference is related to the current by the electrical resistance, $\Delta U = R \cdot I$ and for a series of N electrical elements, the individual resistances add up as

$$U_{\text{tot}} = I \cdot \sum_{i=0}^{N} R_i. \tag{2.26}$$

Also, the contribution of an element to the total resistance is equal to the proportional potential difference at this element, i.e.

$$\frac{R_i}{R_{\text{tot}}} = \frac{\Delta U_i}{U_{\text{tot}}}, \tag{2.27}$$

with $R_{\text{tot}} = \sum R_i$. In gas exchange, the concentration plays the role of the potential and the current is replaced by the mass flux. If transport is statistically homogeneous in x and y, then one can assign a differential resistance $\mathrm{d}c(z)$ to each height element dz, such that, under stationary conditions,

$$\mathrm{d}c(z) = \frac{\partial c}{\partial z}\,\mathrm{d}z = j \cdot \mathrm{d}R(z). \tag{2.28}$$

The concentration profile normalized by the mass flux j is therefore the integrated resistance up to height z,

$$\frac{c(z) - c(z=0)}{j} = \frac{1}{j}\int_0^z c(z')\,\mathrm{d}z' = \int_0^z R(z')\,\mathrm{d}z = R(z). \tag{2.29}$$

In this sense, a concentration profile is equivalent to a resistance profile times the flux. In particular, it describes the vertical distribution of resistance.

In general, when stating the value of a transfer resistance at given flow conditions, the reference height to which this applies has to be specified.

$$\frac{c(z_2) - c(z_1)}{j} = \frac{1}{j}\int_{z_1}^{z_2} c(z)\,\mathrm{d}z = \int_{z_1}^{z_2} R(z)\,\mathrm{d}z = R(z_1, z_2). \tag{2.30}$$

If in a field experiment, concentration samples are taking in discrete heights, say, 2 and 5 m above the water surface, then one is really probing the transfer resistance associated with this layer. It has to be scaled up to the entire layer of interest assuming a certain resistance distribution. In a laboratory gas exchange experiment, in which the transfer resistance is deduced from mass balance considerations (see sec. 7.4), the entire turbulent boundary layer contributes to the result. The lower boundary in eq. (2.29) in this case is $z_1 = 0$ and the upper boundary is $z_2 = \delta$ (see sec. 2.2). In experiments that visualize the scalar concentration profile, effectively the contribution of each layer in the fluid to the total resistance is obtained, potentially providing a more detailed insight in the transport processes involved.

2.4 Short review of gas transfer models

Several models have been developed starting almost from the beginning of the last century in an attempt to describe gas transfer through the air-water interface based on measurable parameters. A comprehensive review would certainly go beyond the scope of this chapter and I will only outline some of the basic concepts of the different approaches. I will pay particular attention to the turbulent diffusivity model as it provides a conceptually valid description of the air-sided transport process.

Most models share the peculiarity of a characteristic scaling with the diffusion constant, or the Schmidt number Sc depending on the boundary condition.

2.4.1 Turbulent diffusivity

In analogy to the momentum transport, the $\langle c'w' \rangle$ term in eq. (2.11) can be replaced by a mean expression, relating the turbulent scalar transport to the mean concentration gradient,

$$j = -\mathrm{D}\frac{\partial c}{\partial z} + \langle c'w' \rangle = -\left(\mathrm{D} + K_{\mathrm{diff}}(z)\right) \cdot \frac{\partial \bar{c}}{\partial z}. \tag{2.31}$$

A model for $K_{\mathrm{diff}}(z)$ has been proposed by *Deacon* (1977) by extending Reichardt's description from momentum to scalar transport. He assumes the turbulent mixing of a tracer gas to be identical to the turbulent mixing of momentum density, i.e. he assumes the so-called turbulent Schmidt number $\mathrm{Sc}_{\mathrm{turb}} = K_{\mathrm{turb}}(z)/K_{\mathrm{diff}}(z)$ to be one. By replacing the kinematic viscosity ν with its equivalent for scalar transport, the diffusion constant D, the turbulent diffusivity becomes

$$\frac{K_{\mathrm{diff}}(z^+) + \mathrm{D}}{\mathrm{D}} = 1 + \mathrm{Sc} \cdot \kappa \left(z^+ - z^+_\ell \tanh\left(\frac{z^+}{z^+_\ell} \right) \right). \tag{2.32}$$

Compared to eq. (2.20), the turbulent contribution is additionally scaled by the Schmidt number, $\mathrm{Sc} = \nu/\mathrm{D}$. It is this scaling that causes the transport resistance to be distributed differently on the water and on the air-side, respectively. For acetone, the tracer used in this work, the air-sided Schmidt number is $\mathrm{Sc}_{\mathrm{air}} = 0.15\,\mathrm{cm^2/s} / 0.105\,\mathrm{cm^2/s} = 1.43$, while for the water side it is $\mathrm{Sc}_{\mathrm{water}} \approx 1 \times 10^{-2}\,\mathrm{cm^2/s} / 1 \times 10^{-5}\,\mathrm{cm^2/s} = 1000$.

It should be noted that Deacon's parametrization is valid for a rigid wall boundary (see sec. 2.2.3). For the airflow over the water surface, this is certainly satisfied. For the waterflow, this is presumably a good description in the presence of surfactants, but only approximative for clean water. Here, the purpose of the comparison is to illustrate the different scales involved in air and water.

Figure 2.1 (a) shows the ratio $\mathrm{D}/(\mathrm{D}+K_{\mathrm{diff}}(z))$ as a function of dimensionless distance z^+ from the air-water interface. The distance $z^+_{1/2}$ at which $\mathrm{D} = K_{\mathrm{diff}}(z)$ provides a

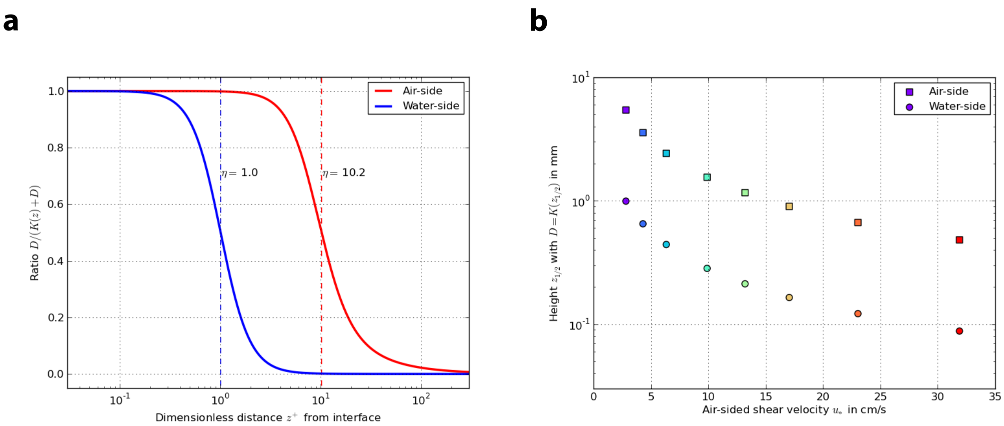

Figure 2.1: (a) Ratio ${}^{\mathrm{D}}/_{\mathrm{D}+K_{\mathrm{diff}}(z)}$ as a function of dimensionless distance z^+ from the air-water interface. The two curves show the molecular contribution to the overall diffusivity for the air side (red) and water-side (blue). The distance $z^+_{1/2}$ at which $\mathrm{D} = K_{\mathrm{diff}}(z)$ is indicated by a dashed line. (b) Comparison of $z_{1/2}$ for typical friction velocities of the wind-wave tank used in this work.

scale closer to which molecular diffusion prevails over turbulent mixing. Due to the larger Schmidt number in water, $z^+_{1/2}$ is about one order of magnitude smaller in dimensionless coordinates. It can be re-scaled to physical coordinates according to eq. (2.2.1) and by exploiting eq. (2.15). A comparison of the resulting values of $z_{1/2}$ is shown in Fig. 2.1 (b) for typical friction velocities of the wind-wave tank used in this work. This sets a requirement on the scales necessary to resolve in the visualization experiments on the air and water side, respectively.

Theoretical concentration profiles can be calculated by integrating eq. (2.32) and eq. (2.31).

$$c(z^+) = \frac{j_s \mathrm{Sc}}{u_*} \cdot \int_0^{z^+} \frac{\mathrm{D}}{\mathrm{D} + K_{\mathrm{diff}}(z^+)} dz^+ \tag{2.33}$$

The result is shown in Fig. 2.2 for the water and air side separately for typical values of u_*. The profiles are normalized to vary between 0 and 1 and depicted in a way to reflect an invasion experiment. The air and water-sided Schmidt numbers of a typical gas differ by about 3 orders of magnitude and this has been seen in Fig. 2.1 to have a significant impact on the scales up to which molecular diffusion is a relevant transport mechanism. Consequently, the resistance in air and water is expected to be distributed in a much different way. Figure 2.3 shows resistance profiles, $R(z) = {}^{c(z)}/_{j_s}$, according to eq. (2.33) for $\nu_{\mathrm{air}} = 0.15\,\mathrm{cm}^2/\mathrm{s}$, $\nu_{\mathrm{water}} = 1 \times 10^{-5}\,\mathrm{cm}^2/\mathrm{s}$, $\mathrm{D}_{\mathrm{acetone,air}} = 0.105\,\mathrm{cm}^2/\mathrm{s}$, $\mathrm{D}_{\mathrm{acetone,water}} = 1.29 \times 10^{-5}\,\mathrm{cm}^2/\mathrm{s}$, and typical values of the friction velocity u_*. Both sets of profiles show a logarithmic dependence on height further away from the surface, although for the water profiles, this is less pronounced compared to the increase of resistance within the diffusive sublayer. Indeed, in the water, the contribution of the logarithmic sublayer to the overall resistance is negligible. This is

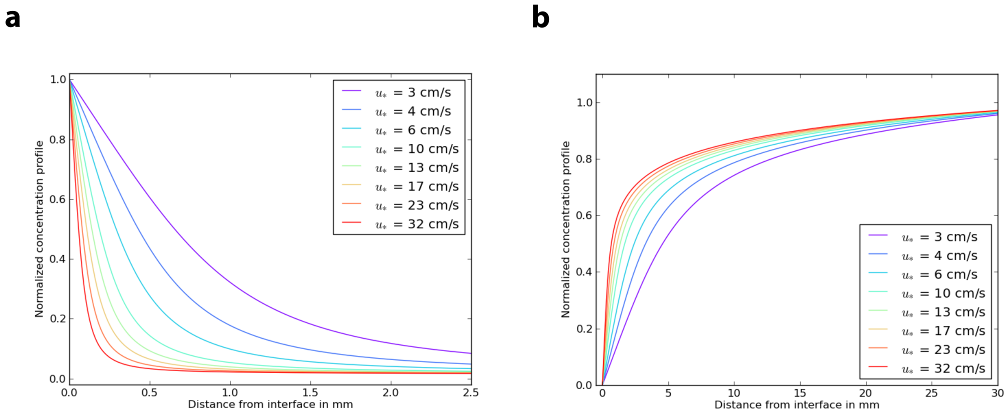

Figure 2.2: Theoretical water-sided (a) and air-sided (b) profiles, normalized to vary between 0 and 1 at surface and bulk, respectively. The profiles are depicted in a way to reflect an invasion experiment.

due to the much larger Schmidt number and reason for the common assertion that the water-sided diffusive sublayer dominates the transfer resistance. It should be mentioned though that on larger scales, i.e. further away from the phase boundary, other physical phenomena might play a role not considered here, such as stratification, thermal layering etc. which create a notable resistance. In the here presented analysis, only near-surface turbulence and diffusion are taken into account.

Contrarily, on the air-side, contributions of the diffusive and logarithmic sublayers are of similar orders of magnitude (not including the outer layer). Indeed, from Fig. 2.3 it can be seen, that up to a distance of 1 m from the water surface, the total resistance reaches already twice its value right above the diffusive sublayer. In a laboratory experiment, the width of the logarithmic layer will be limited and flow above a certain height will always be dominated by boundary conditions posed by the tank's geometry. On the other hand, in a well developed turbulent flow like above the open ocean, the turbulent boundary may easily grow to larger width. Under such conditions, the air-sided diffusive sublayer is expected to contribute negligibly to the overall resistance. To study and verify the scaling properties of the air-sided mass boundary layer was in part scope of this thesis.

It should be noted that although analogy of momentum and mass transport in the air is generally accepted in literature, experimental data on the latter is scarce. In particular, to my best knowledge no concentration profiles have so far been observed down to the diffusive sublayer.

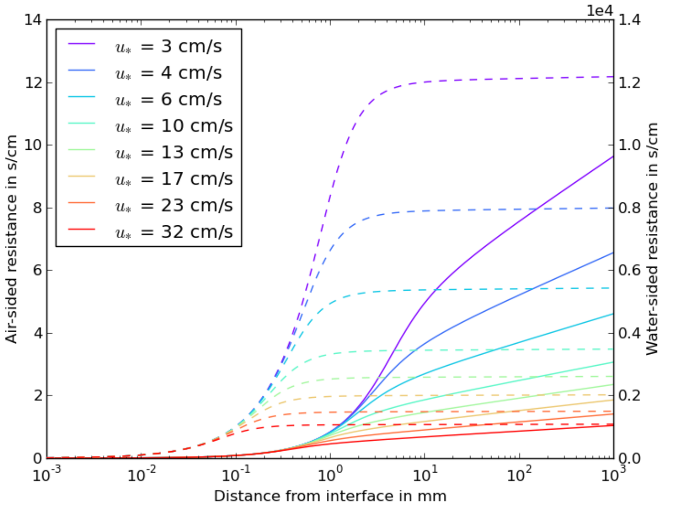

Figure 2.3 Comparison of theoretical air and water-sided acetone concentration profiles according to the turbulent diffusivity model for typical friction velocities u_* used in this work.

2.4.2 Two layer stagnant film model

An idealized model for gas exchange is the film model, initially proposed by *Lewis and Whitman* (1924) and applied as a two layer model to gas transfer over open waters by *Liss and Slater* (1974). It assumes a purely diffusive region close to the interface of a certain thickness d and an instantly mixed bulk underneath. In this way, the diffusion equation $\dot{c} = D\Delta c$ has a stationary solution with the boundary condition $c(z=0) = c_s$ and $c(z=d) = c_b$, which is simply a linear decay. The transfer velocity is then entirely given by this diffusive layer as $k = {}^{D}\!/_{d}$. The model is certainly idealized as it requires an infinite flux at $z = d$. Also, the model does not provide any means to deduce the layer thickness d from fluid mechanical considerations.

Also, as pointed out by *Jähne et al.* (1987), the model overestimates fluxes and depends linearly on the diffusion constant contrary to other models.

2.4.3 Surface renewal

Another conceptual model was proposed by *Higbie* (1935) and elaborated by *Danckwerts* (1951) based on the intermittent nature of turbulence. He assumes the mass transport to be diffusion controlled close to the surface. According to the diffusion equation, a non-stationary concentration profile will then form characterized by an increasing thickness and a flux which decreases in time. Turbulence is thought to randomly cause patches on the surface to be entirely cleared and washed down into the well-mixed bulk. This process is statistically associated with a renewal rate s. Danckwerts finds the following relationship for the transfer velocity

$$k = (\mathrm{D}s)^{1/2} \quad \text{or} \quad R = (\mathrm{D}s)^{-1/2}. \tag{2.34}$$

Different from the film model, it depends on the square root of the diffusion constant. By replacing the covariance term in eq. (2.9) with a renewal term, $s \cdot c$, *Jähne* (1985) obtains an expression for the mean concentration profile (assuming gas flux into the water)

$$c(z) = c_\mathrm{b} + (c_\mathrm{s} - c_\mathrm{b}) \exp\left(-\frac{z}{z^*}\right). \tag{2.35}$$

The characteristic scale is defined as $z^* \equiv \sqrt{D/s}$. Under the assumption that transport is governed by diffusion at the surface and that this profile also provides a valid description on those scales, it has to obey Fick's law, $j = -D\partial c/\partial z$ and the transfer velocity or resistance can be retrieved as

$$k = \frac{\mathrm{D}}{z^*} \quad \text{or} \quad R = \frac{z^*}{\mathrm{D}}. \tag{2.36}$$

This surface renewal model does not incorporate any fluid mechanical boundary conditions. Nonetheless, if renewal events are thought to be related with turbulent eddies reaching the surface, the model appears conceptually compatible with a free surface.

2.4.4 Eddy renewal and surface divergence

A series of models, extensions, and refinements are based on a concrete description of surface renewal by turbulent eddies distributed underneath the surface. *Fortescue and Pearson* (1967) were the first to propose a so-called large-eddy model. *Lamont and Scott* (1970) depart from similar concepts, but allowed also smaller eddies in their eddy-cell model. They found a dependence of the resistance on Schmidt number as $R \propto Sc^{1/2}$ for a free surface and $R \propto Sc^{2/3}$ for a rigid surface. In both models, divergences are attributed to eddies which are sourced by the shear flow.

Csanady (1990) points out that according to experimental results, shear induced divergence is too small at higher wind speeds and that instead divergence generated by breaking wavelets could be responsible. He proposes a model based on divergent two-dimensional stagnation point flow at a free plane surface. The model has a free parameter characterizing the fractional divergence coverage of the surface.

Interest in surface divergence as possible parameter to describe gas exchange has grown recently. This also owes to an enormous increase in computational power allowing to study small scale flow patterns in the water in detail. Examples include the works by *Tsai and Hung* (2007); *Tsai et al.* (2013) and *Banerjee et al.* (2004). Likewise, thermographic imaging is a promising tool to visualize surface flow structure, possibly in parallel with other techniques (*Asher et al.*, 2012; *Haußecker et al.*, 1995).

2.5 Solubility

A quantity of importance for gas exchange is the so-called solubility, also known as partition coefficient. Given a fixed temperature and pressure and assuming thermodynamic equilibrium, to each mole fraction of substance A mixed into substance B there will be a corresponding mixing ratio in the gas phase. This is usually shown in a so-called binary phase diagram. Generally, this is a non-linear function depending on the properties of the substances involved. Henry's law is the tangential approximation to the binary phase diagram for the limit of very dilute mixture.

The partition coefficient, or solubility, is then the ratio of concentration in the gas and liquid phase,

$$\alpha_\mathrm{H} \equiv \frac{c_\mathrm{water}}{c_\mathrm{air}}. \tag{2.37}$$

In literature, also the inverse is found. In the above definition, α_H is dimensionless and the concentration is usually given in mol/L. Alternatively, the gas phase fraction can be given in terms of a partial pressure p. By the ideal gas law, this is related to a concentration in mole per volume as $c = {}^{p}\!/_{RT}$, where R is the universal gas constant and T the temperature. I use the dimensionless version of Henry's law throughout the thesis.

In air-sea gas exchange, the solubility is used to relate air and water-sided concentrations in the transport process. For a concentration c_water measured in the water, its air-equivalent value is ${}^{c_\mathrm{water}}\!/_{\alpha_\mathrm{H}}$. Consequently, the air-equivalent difference of two concentrations of which one is measured in the water and one in the air, is $\Delta c = c_\mathrm{air} - {}^{c_\mathrm{water}}\!/_{\alpha_\mathrm{H}}$. This leads to a partitioning of transport resistances among the gaseous and aqueous phase which depends on solubility, as explained by *Liss* (1971).

The resistances attributed to the transport in the air and water, respectively, are

$$R_\mathrm{a} = \frac{c_\mathrm{b}^\mathrm{air} - c_\mathrm{s}^\mathrm{air}}{j} \quad \text{and} \quad R_\mathrm{w} = \frac{c_\mathrm{s}^\mathrm{water} - c_\mathrm{b}^\mathrm{water}}{j}, \tag{2.38}$$

where c_b and c_s stand for bulk (well-mixed) and surface concentration, respectively, and j is the stationary flux. The air-equivalent values are obtained by dividing the second of the above equations by α_H. The air-equivalent resistance attributed to the aqueous phase is then ${}^{R_\mathrm{w}}\!/_{\alpha_\mathrm{H}}$ and total (air-equivalent) sum is given by

$$R_\mathrm{tot} = R_\mathrm{a} + \frac{1}{\alpha_\mathrm{H}} R_\mathrm{w} \tag{2.39}$$

When matching air-sided and water-sided concentrations, I will always express them as air-equivalent values.

Equation (2.39) shows that for a gas with high solubility, the water-sided resistance becomes relatively less important. In Fig. 2.3, I illustrated based on the turbulent diffusivity model that the water-sided resistance for acetone is roughly larger than the air-sided one by a factor of 1000. On the other hand, its solubility is about 800 (see sec. 3.1.4) and accordingly both phases are expected to contribute to similar proportion to the overall resistance, i.e. $R_\mathrm{a}/R_\mathrm{tot} \approx R_\mathrm{w}/R_\mathrm{tot}$. Following the line-of-thought in sec. 2.3, this also implies that the (air-equivalent) concentration differences between bulk and surface should be similar in the water and in the air. In particular, the air-sided concentration is expected to decay to about half its bulk value at the water surface. For gases with low solubility, the air side is effectively irrelevant in terms of resistance and their transport is said to be controlled by the water side.

3

Visualization technique

The visualization technique used in this work is based on the principle of LIF. A tracer gas, mixed into the air-compartment of a wind-wave tank, is illuminated with laser light and from the emitted fluorescent light intensity observed with a camera, the concentration of the tracer gas in deduced. In this chapter, I explain the visualization technique from the physics point of view. The experimental implementation of the entire set-up can be found in chap. 4.

In view of the vast literature available on the topic of LIF, I present only those aspects relevant for this study. In particular, I introduce some important characteristic parameters, review criteria for the suitability of a tracer gas, and summarize the properties of the selected substance, acetone.

In the last section, I explain the method used in this work to deduce tracer concentration from quotient images and explain how saturation effects can thereby effectively be taken into account.

For further reading on the principles of fluorescence, I refer e.g. to *Lakowicz* (2006).

3.1 Laser induced fluorescence

3.1.1 Principles of fluorescence

A simple conceptual model for the absorption and emission processes leading to fluorescence is a two-level (or possibly three-level) atomic system, comprised of a singlet ground state, S_0, and excited singlet state, S_1, and possibly an excited triplet state T_1. Such an exemplary Jablonski diagram is depicted in Fig. 3.1. While situations might require more complicated models, this scheme is used here to explain the

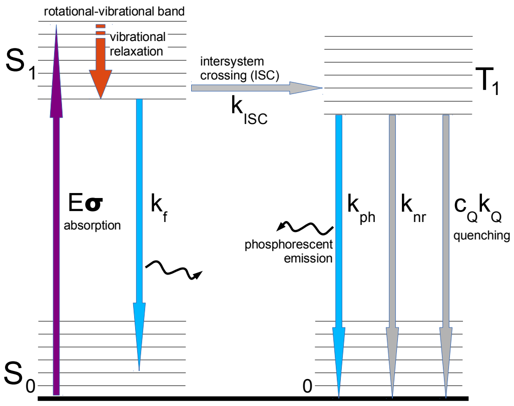

Figure 3.1
Jablonski diagram for a three-level molecular energy structure with some possible transitions. S_0 is the ground state, S_1 and T_1 are the excited singlet and triplet states, respectively. Transition rates are indicated by k_X. For polyatomic molecules, rotational-vibrational modes create a quasi continuous band.

basic principles relevant for this thesis.

Each possible transition is symbolized by an arrow and characterized by a rate constant k_i which has the unit s^{-1}. Its inverse can be interpreted as the lifetime of the related state, $\tau_i = k_i^{-1}$. Rate constants for parallel transitions add up to a total rate constant and accordingly the total (and observable) lifetime is given by the sum of the inverse individual lifetimes, $\tau^{-1} = \sum_i \tau_i^{-1}$. Consequently, the fastest transitions dominates the lifetime of a state. Similarly, the relative occurrence of a transition i is given by the ratio $^{k_i}/_{\sum k_i}$.

Absorption of photons of a given energy $^{hc}/_{\lambda}$ cause atomic electrons to move from S_0 to S_1. If de-excitation occurs back to the ground state accompanied by the emission of a photon, this radiation is observed as fluorescence light. For excited states broadened, e.g., due to a band of vibrational energies, an electron can dissipate energy internally (transiting trough vibrational states) prior to the re-emission of a photon. This effect is commonly known as Stokes shift and causes the emission spectrum to be red-shifted. In radiometric applications of LIF, a negligible overlap of absorption and emission spectrum, i.e. a large Stokes shift, is desirable to exclude the effect of re-absorption. By the so-called intersystem crossing (ISC), electrons can move from S_1 to T_1. The transition from T_1 back to the ground state S_0 is quantum mechanically suppressed leading to a comparatively small rate constant k_{phos}, or equivalently long lifetime τ_{phos}. The light emission related to this suppressed transition is commonly referred to as phosphorescence. In the presence of other modes of energetic relaxation, e.g. non-radiative decay k_{nr} or collisional quenching k_{Q}, the phosphorescence intensity is further suppressed, $^{k_{\mathrm{ph}}}/_{k_{\mathrm{nr}}+k_{\mathrm{Q}}+k_{\mathrm{phos}}}$. Several other decay modes exist, but a complete overview would be beyond the scope of this chapter. The mechanisms specifically relevant for acetone are discussed in sec. 3.1.4.

3.1.2 Measurement principle

The measurement principle by which the tracer concentration is determined through LIF in this thesis is based on the dependence of the emitted fluorescent light intensity on the tracer concentration. This is easily analyzed in the regime of weak excitation, i.e. when the majority of electrons are in ground state and only a small fraction is excited. For higher laser irradiance, the relation becomes non-linear, but within certain limits, this can still be taken into account through an appropriate normalization procedure. I explain this in detail in sec. 3.1.6 and discuss the effect of saturation and its relevance for this visualization technique in sec. 3.1.5. A general weak regime expression for the relationship between fluorescent brightness F recorded by a camera, laser irradiance I, i.e. incident energy per time and unit area, and tracer concentration c can e.g. be found in *Thurber* (1999),

$$F = \frac{I}{hc/\lambda} \eta_{\mathrm{opt}} \, \mathrm{d}V c_{\mathrm{tracer}} \sigma_{\mathrm{cs}}(\lambda, T) \Phi_{\mathrm{f}}(\lambda, T, P), \tag{3.1}$$

where η_{opt} is the overall efficiency of the recording optics and camera (including vignetting), σ_{cs} the absorption cross section, and Φ_{f} the quantum efficiency. While the cross section quantifies the probability of an incident photon to be absorbed by the tracer molecule, Φ_{f} gives the ratio to which this absorption eventually leads to the re-emission of a photon. Both functions depend on wavelength of the incident light, and generally on temperature and pressure. Ideally, the latter two dependencies are small or negligible for the purpose of retrieving the tracer concentration. Direct calculation of the absolute tracer density from the above equation would require exact knowledge of all the contributing terms. Instead, the approach used in this thesis is to relate the signal to a reference image with known concentration c_{ref} , i.e. to regard the relative signal

$$\frac{F}{F_{\mathrm{ref}}} = \frac{c}{c_{\mathrm{ref}}}. \tag{3.2}$$

A more rigorous derivation is given in sec. 3.1.6 and implementation of the procedure in the data processing routine is explained in sec. 7.1.1. Equation (3.1) is nonetheless useful as it contains all the terms to take into consideration when selecting a suitable tracer substance. This is done in the next section.

3.1.3 Choice of tracer

A tracer gas must meet certain criteria to be usable in a LIF-based visualization experiment of scalar transport across the air-water boundary layer in a wind-wave tank. These are explained here and a choice of tracer is deduced thereof.

For the visualization of scalar distributions in air, and possibly water, close to the air-water interface, the absorption spectrum of a suitable tracer should be accessible with a commercially available laser system and offer at least a reasonable quantum yield. The Stokes shift (see sec. 3.1.1) should be large enough to avoid overlap between absorption and emission spectrum, i.e. to avoid self-excitation. Fluorescence in the visible range of the spectrum is preferred as this allows to easily monitor an experiment by eye and to employ standard cameras and optics as opposed to UV-transmissive elements. Tracers with self-quenching properties have the disadvantage of introducing non-linear, implicit relations between tracer concentration and observed brightness. Fluorescence lifetime should be short (on the order of ns) to minimize the effect of collisional quenching typical for long-lived, phosphorescent tracers and to avoid complications due to saturated stimulation, as explained in sec. 3.1.5.

In terms of thermodynamic properties, a suitable tracer should be sufficiently volatile to allow for good seeding in the air-flow during an invasion experiment. On the other hand, the solubility needs to be high ($\alpha_H \geq 500$) for the air-side to contribute significantly to the overall resistance (see sec. 2.5). Not the least, toxicity has to be carefully considered.

An experimental study of possible tracers in this kind of experimental setting has already been performed by *Winter* (2011). A comprehensive literature review of tracers for planar LIF can be found in *Lozano* (1992). While Lozano's application is in the field of flow visualization in flames and combustion, thus at much higher temperatures than relevant for an environment-like experiment, his very systematic analysis provides useful information also for the application in this work. I will follow his structure, stating conclusions in a rather compact way, and in part refer to Winter's results.

Diatomic molecules can be ruled out, mainly due to technically demanding excitation, quenching, and sometimes toxicity. As exception, NO has been used in planar laser induced fluorescence (PLIF) experiments, but is potentially lethal when inhaled. Polyatomic molecules, in general, have wide rotational-vibrational (henceforth rovibrational) bands so that absorption and emission spectra are typically continuous. Since thermal relaxation of an excited state within the rovibrational manifold is fast compared to the radiative decay, the Stokes shift is often large and overlap of absorption and emission spectra is small or negligible. Inorganic polyatomic molecules used for LIF are rare, with the exception of NO_2 and SO_2, where the former is lethal already in small amounts and the latter shows strong self-quenching.

Another group of polyatomic molecules are aromatic compounds. They often have exceptional quantum efficiency of $\Phi_f \geq 0.5$, but volatility (and solubility) is unacceptably low due to the size and structure of the molecules. Benzene and derivatives represent the smallest (and thus most volatile) candidates in this category, but usually they are carcinogenic. Additionally, solubility is too low. Among small organic, non-aromatic compounds, aldehydes, (di-)ketones, and amines show luminescence. Lozano provides a list with some physical parameters. In general, these substances are interesting as their boiling point is low and their volatility is fairly high. Some of these molecules are ruled out because of (self-)quenching, others due to their toxicity, such as formaldehyde and acetaldehyde.

From this analysis, two potential LIF tracers emerge, acetone and diacetyl. The

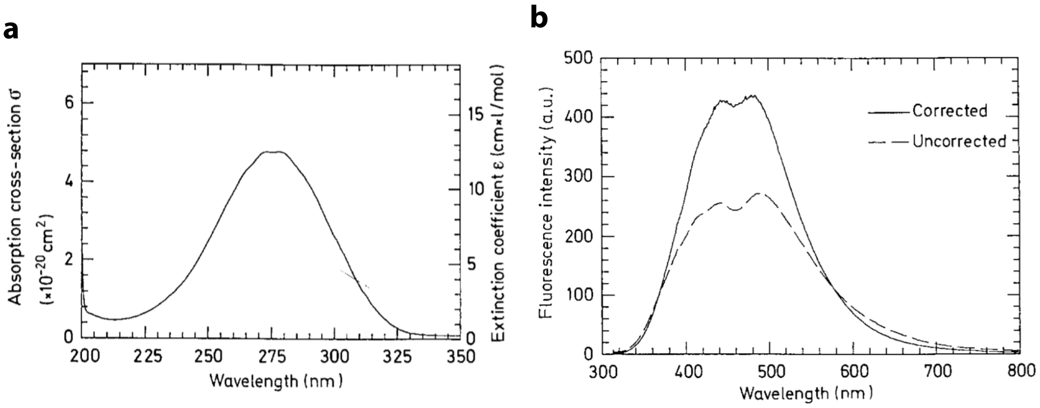

Figure 3.2: (a) Absorption spectrum of acetone, taken from *Lozano et al.* (1992). (b) Emission spectrum of acetone corrected for detector response. Units are normalized to the maximum value. Figure taken from *Bryant et al.* (2000).

former has already been tested by *Winter* (2011) and found to be rather applicable.

Notably, diacetyl has a very high phosphorescence yield of $\Phi = 0.15$, about 60 times greater than its fluorescence yield. On the other hand, the long lifetime of 1.5 ms suggests strong susceptibility to quenching. Indeed, in air and under standard atmospheric pressure, the phosphorescence signal is suppressed by a factor of ≈ 6000 requiring, e.g, a nitrogen atmosphere. Anyhow, the long lifetime might create difficulty when attempting to record frozen images of the turbulent airflow. Diacetyl has therefore been rejected as tracer substance.

In this thesis, acetone was selected as tracer gas, since it meets nearly all of the above listed requirements. Its properties are described in the following section.

3.1.4 Properties of acetone

A summary of physical properties of acetone is given in Tab. 3.1 and the electronic levels schematically correspond to the Jablonski diagram in Fig. 3.1.

Acetone can be excited in the UV regime, e.g. at $\lambda = 266\,\mathrm{nm}$, and in this work, a frequency quadrupled neodymium-doped yttrium aluminum garnet (Nd:YAG) laser with $\lambda_{\mathrm{emission}} = 266\,\mathrm{nm}$ was used. Therefore, all wavelength dependent parameters are provided for this value. An absorption spectrum, taken from *Bryant et al.* (2000), is shown in Fig. 3.2 (a). The extinction coefficient at $\lambda = 266\,\mathrm{nm}$ is $\epsilon_{266\,\mathrm{nm}} = 11.7\,\mathrm{cm\,L/mol}$. The broadband character is evidence for the dense rovibrational manifolds in the excited and ground states.

The ISC of acetone is close to 100 %, so that most excited electrons are in the T_1 state from where the phosphorescent radiative decay is quenched. Of the remaining ones in the S_1 state, many decay radiation-less and only a small portion actually causes luminescent light emission. This is the reason for the relatively low quantum yield of $\Phi_f = 0.2\,\%$. An emission spectrum is given in Fig. 3.2 (b) and shows a brought peak in the blue range of the visible spectrum. This allows to employ standard optics

Table 3.1: Summary of relevant physical properties of acetone at T = 25 °C and p = 1 atm

Parameter	Value	Source
abs. cross section σ_{cs}	4.4×10^{-20} cm^2	*Lozano et al.* (1992)
extinction coefficient ϵ_{air}	11.7 L/(mol cm)	*Lozano et al.* (1992)
extinction coefficient ϵ_{water}	15.2 L/(mol cm)	*Feigenbrugel et al.* (2005)
diffusion constant D$_{water}$	1.29×10^{-9} m^2/s	*Grossmann and Winkelmann* (2005)
diffusion constant D$_{air}$	0.105 cm^2/s	*Lugg* (1968)
fluorescence life time τ	2.7(3) ns	*Breuer and Lee* (1971)
vapor pressure	0.27 atm	*Ambrose et al.* (1974)
quantum yield of Φ_f	0.2 %	*Lozano et al.* (1992)
Solubility α_H	732, 800	*Benkelberg et al.* (1995) *Betterton* (1991)

and cameras.

Thurber (1999) and *Bryant et al.* (2000) show that there is no appreciable dependence of cross section and fluorescence yield on temperature in a range of $T = (23 \pm 10)$°C, so that this effect can be neglected for the visualization experiments presented in this work.

Ambrose et al. (1974) report a vapor pressure of acetone at room temperature of 0.27 atm. This high value indicates that injection into the wind-wave tank can easily be achieved, e.g. by flushing air through a bubbling flask. Indeed, I adopted this simple but efficient technique in the visualization experiments (see sec. 6.1.1). On the other hand, the high vapor pressure guarantees condensation of acetone in the tank not to be a relevant phenomenon even if some elements of the tank structure were cooler than the air by some centigrade.

Acetone is known to dissociate to some degree under the influence of UV radiation (*Gandini and Hackett*, 1977; *Hansen and Lee*, 1975; *Heicklen*, 1959; *Ho et al.*, 1975). In particular, the molecule dissociates to produce an acetyle radical,

$$\mathrm{CH_3COCH_3} + h\nu \longrightarrow \mathrm{CH_3CO} + \mathrm{CH_3}.$$

Two radicals can then recombine to form diacetyl

$$\mathrm{CH_3CO} + \mathrm{CH_3CO} \longrightarrow \mathrm{CH_3COCOCH_3}.$$

In a small, static cell, *Lozano* (1992) observed some build-up of diacetyl when exposed to the light of a 308 nm XeCl excimer laser, although the scope of his experiment was merely to illustrate the effect qualitatively. An estimate on the relevance of photolytic diacetyl formation during the visualization experiments presented in this thesis can be made based on the diacetyl production yield of 0.2 given in *Gandini* *and Hackett* (1977). For typical concentrations of acetone of 10^{-3} mol/L, a lifetime of 2.7 ns, and a laser irradiance of 50 mJ/pulse, about 10^{16} photons are absorbed along a distance of 90 mm in the tank. For a production yield of 0.2, this corresponds 2×10^{-9} mol/pulse of produced diacetyl, or 4×10^{-8} mol/s with a laser frequency of $f_{\text{laser}} = 2\,\text{Hz}$. To produce a total amount of 10^{-3} mol diacetyl, equivalent to $^1/_{20}$ of the assumed acetone concentration for an air volume of 220 L, would require about on the order 100 hours of constant irradiation under these conditions. Diacetyl formation can therefore be neglected for visualization experiments especially since acetone is constantly transported into the water and re-flushed into the air compartment of the tank.

3.1.5 Saturation

In eq. (3.1), the weak excitation limit was assumed, i.e. most electrons are in ground state and only a few are excited. For high enough laser irradiance, this is not true anymore and the emitted brightness is less than proportional to the incident photon flux. In the extreme case of infinite photon flux, state occupation is in equilibrium and no additional laser photon can be absorbed. Fluorescence then becomes fully independent of laser irradiance. The effect of saturation is well-described e.g. in *Crimaldi* (2008).

More generally, the fluorescence intensity is related to the laser irradiance by

$$F(c, I) \propto c \cdot I \, \frac{I_{\text{sat}}}{I_{\text{sat}} + I}. \tag{3.3}$$

Here, I_{sat} is a constant defined by $^{F(I_{\text{sat}})}/_{F(I \to \text{inf})} = 1/2$, which depends on the tracer. From this definition and analyzing the rate equations which describe the radiative decay, the saturation irradiance in $\text{J/m}^2\text{/s}$ can be related to the cross section σ_{cs} and the lifetime of the emitting state τ as

$$I_{\text{sat}} = \frac{1}{\sigma_{\text{cs}} \tau} \cdot \frac{hc}{\lambda}, \tag{3.4}$$

with $^{hc}/_{\lambda}$ the energy of a single photon.

Note that for $I \ll I_{\text{sat}}$, eq. (3.3) reduces to $F \propto c \cdot I$, i.e. the weak regime expression. The absorption cross section of acetone at $\lambda = 266\,\text{nm}$ can be read from Fig. 3.2 (a) as $\sigma_{\text{cs}} = 4.4 \times 10^{-20}\,\text{cm}^2$ and the fluorescence lifetime is given in Tab. 3.1 as $\tau = 2.7\,\text{ns}$, so that $I_{\text{sat}} \approx 2 \times 10^8\,\text{J/mm}^2\text{/s}$. For a pulse duration of 8 ns, this corresponds to

$$I_{\text{sat}} \approx 0.5\,\text{J/mm}^2\,\text{/pulse}. \tag{3.5}$$

To verify the assumption $I \ll I_{\text{sat}}$, I numerically calculated the expected fluorescence signal based on this value for a realistic beam geometry. The result helped to estimate and exclude systematic influences of the laser irradiance on the extracted

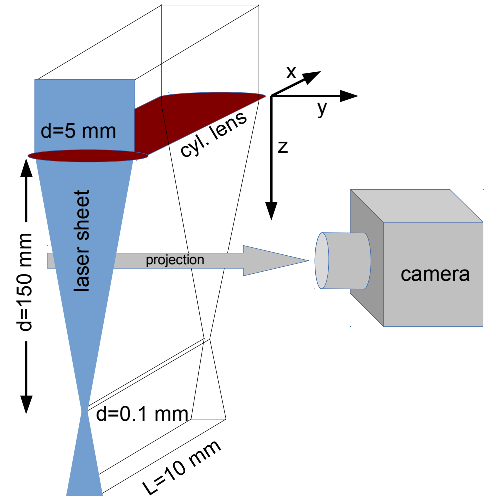

Figure 3.3
Sketch of the model set-up used to simulate the attended effect of laser saturation.

concentration profiles and to appropriately choose a data processing approach (see sec. 7.1.1). The sketch of the idealized set-up used for this analysis is shown in Fig. 3.3.

I assume a laser sheet of length 10 mm and initial width d of 5 mm which narrows linearly to 100 µm at 150 mm distance and then diverges again linearly. This is certainly idealized because real (Gaussian) laser beams have a characteristic waist around their focal plane reciprocal to the beam convergence (*Träger*, 2007). For the purpose of modeling the effect of saturation here, this geometric approximation seems adequately precise, however. The water height in an experiment would coincide with the focal plane. The emitted fluorescence is observed with a camera at 90° and image recording is modeled by projecting, i.e. integrating, the emission density along the line of sight (assumed as the y-axis). The problem is treated as homogeneous in x-direction. This geometry closely resembles the experimental set-up presented in sec. 4.3.1.

In the following, small curly letters indicate density and capital letters its projection along the y-axis, e.g. $I(z) = \int \iota(y,z)\,\mathrm{d}y$. The origin of the vertical z axis is set to the initial position of the unfocused sheet with z increasing towards the focus point. The maximum power of the used laser system is 50 mJ / pulse so that the irradiance at $z = 0$ is $\iota_0 = 1 \times 10^{-3}\,\mathrm{J/mm^2}$ /pulse. A homogeneous concentration of realistic value $c\epsilon_{\mathrm{air}} \approx 2\,\mathrm{mm}^{-1}$ is assumed and Lambert-Beer absorption is treated as a mono-exponential decay, i.e.

$$I(z)/I_0 = \exp\left(-\epsilon_{\mathrm{air}} c z\right), \tag{3.6}$$

and a Gaussian sheet profile in y-direction is assumed,

$$\iota(y,z) = N(z) \cdot \exp\left(-\frac{y^2}{2d^2}\right), \tag{3.7}$$

with N chosen such that $\int_{-2d}^{2d} \iota(y,z)\,\mathrm{d}y = I(z)$.

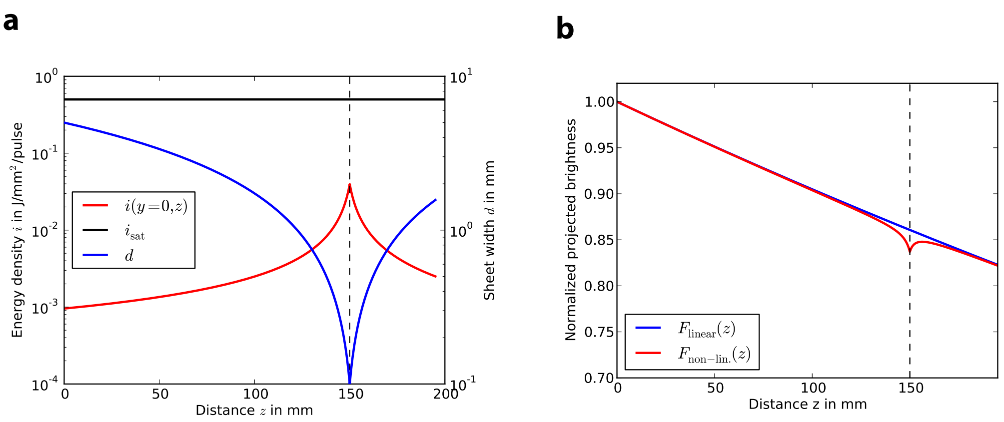

Figure 3.4: (a) Modeled irradiance for a laser sheet of length $L = 10\,\mathrm{mm}$ and Gaussian shape in y-direction. The width d as a function of z is plotted relative to the right ordinate. The horizontal line gives the saturation irradiance for comparison. The red line depicts the local irradiance in the center of the laser sheet, i.e. at $y = 0$. (b) Modeled projected fluorescence signal, according to eq. (3.8) (red) and in linear approximation $F \propto c \cdot I$ (blue). The maximum systematic deviation is about 2 %.

The modeled fluorescence signal $F(z)$ is then calculated according to eq. (3.3) as

$$F(z) = c \int_{-2d}^{2d} \iota(y,z) \cdot \frac{\iota_{\mathrm{sat}}}{\iota_{\mathrm{sat}} + \iota(y,z)} \, \mathrm{d}y. \tag{3.8}$$

Note that for notational consistency, I used small letter ι_{sat} instead of I_{sat}, as in eq. (3.3).

In the left panel of Fig. 3.4, the irradiance $\iota(y = 0, z)$ in the sheet center is shown as a function of vertical coordinate z. For reference, the sheet width d is plotted relative to the right ordinate. As expected, the decreasing width causes a strong increase in irradiance which however does not exceed the value ι_{sat}. Also, the change in irradiance due to Lambert-Beer is small compared to the impact of beam geometry. The right panel shows the projected fluorescence signal $^{F(z)}/_{F(z=0)}$, according to eq. (3.8) (red) and in linear approximation $F \propto c \cdot I$ (blue). The maximum systematic deviation in the focal plane is about 2 %. This shows that saturation effects are still weak for the such a beam geometry and laser power, but should be taken into account in the procedure by which tracer concentration is deduced from images.

3.1.6 Relative brightness images

In this section, I outline the principle of retrieving tracer concentrations from relative fluorescent brightness. I use the same notation as in the previous section, but the considerations are obviously valid also for a real, non-idealized laser beam. I will also note some not so obvious subtleties and how expressions can be simplified. The implementation of the normalization principle in the data processing routines is explained in sec. 7.1.1.

An effective way to deduce the concentration distribution $c(z)$ from the fluorescence signal is to record reference images without water in the wind-wave tank and consequently homogeneous tracer distribution, i.e. $c_{\mathrm{ref}}(z) = c_{\mathrm{ref}}$, and to match them with data images (i.e. with water, $c(z) \neq \text{const.}$) according to the brightness in the bulk region away from the water surface. The brightness ratio can then be calculated from eq. (3.8) as

$$\frac{F(x,z)}{F_{\mathrm{ref}}(x,z)} = \frac{\int_{-2d}^{2d} c(x,y,z)\cdot\iota(x,y,z)\,\frac{\iota_{\mathrm{sat}}}{\iota_{\mathrm{sat}}+\iota(x,y,z)}\,\mathrm{d}y}{c_{\mathrm{ref}}\int_{-2d}^{2d}\iota_{\mathrm{ref}}(x,y,z)\,\frac{\iota_{\mathrm{sat}}}{\iota_{\mathrm{sat}}+\iota_{\mathrm{ref}}(x,y,z)}\,\mathrm{d}y}, \tag{3.9}$$

where I have added explicitly the horizontal coordinate x to account for the 2D character of the image. As on average, concentration depends on the vertical coordinate z only, $c(y,z)$ can be pulled out of the integral[1].

As a first subtlety one should note that in general saturation effects related to the reference image need not be the same as for the data image because local fluctuations of $c(z)$ with respect to c_{ref} lead to different absorption, thus to different irradiance and thus to different degrees of saturation. However, Fig. 3.4 (a) shows that for the here assumed realistic acetone concentrations the influence of Lambert-Beer absorption on the irradiance modulation is small compared to the sheet geometry. The saturation effect arising from ${}^{\iota_{\mathrm{sat}}}/_{\iota+\iota_{\mathrm{sat}}} < 1$ will therefore be a function of height z, well-mixed bulk concentration c_{b}, and laser power P only, i.e. $\mathrm{Sat}(z; c_{\mathrm{b}}, P)$. It is not important to specify the functional relationship, but sufficient to observe that only macroscopic parameters are involved. In a quotient image, this function will then cancel out.

As a second subtlety one should observe that in the presence of water, the acetone concentration might decay to half of its bulk value within the boundary layer, (see sec. 2.5) causing absorption to be weaker and consequently $\iota(z \approx z_{\mathrm{surf}}) < \iota_{\mathrm{ref}}(z \approx z_{\mathrm{surf}})$. The relative systematic error induced by this approximation is expected to be on the order ${}^{\Delta\iota}/_{\iota} \approx \epsilon c_{\mathrm{b}}\delta$, with δ an estimate for the turbulent boundary layer thickness. For typical values of these parameters, $\epsilon \approx 1\,\mathrm{L\,mm/mol}$, $c_{\mathrm{b}} \approx 1\times10^{-3}\,\mathrm{mol/L}$, and $\delta \leq 10\,\mathrm{mm}$, this is only about 1 %. Summarizing, Lambert-Beer absorption can be well described based on the bulk concentration c_{b} and treated as independent of local fluctuations.

---

[1] Note that spatially averaging is equivalent to ensemble averaging in an ergodic sense.

A last subtlety regards the projection integral. While irradiance in theory is a local quantity expressing photon or energy flux per unit area, all data in the camera-based visualization experiment in this work are projected values. Therefore, and in view of the above mentioned approximations, the fluorescence brightness $F(z)$ is written as a multiplicative function of projected factors. Equation (3.9) then reads

$$\frac{F(x,z)}{F_{\mathrm{ref}}(x,z)} = \frac{c(z)}{c_{\mathrm{ref}}} \cdot \frac{I(x,z;c_{\mathrm{b}})}{I(x,z;c_{\mathrm{ref}})} \cdot \frac{\mathrm{Sat}(z;c_{\mathrm{b}},P)}{\mathrm{Sat}(z;c_{\mathrm{ref}},P)}, \tag{3.10}$$

and by the matching condition $c_{\mathrm{ref}} = c_{\mathrm{b}}$,

$$\frac{F(x,z)}{F_{\mathrm{ref}}(x,z)} = \frac{c(z)}{c_{\mathrm{b}}}. \tag{3.11}$$

To summarize: By calculating the quotient of a data image and a reference ground truth image, concentration profiles normalized to their bulk value can be retrieved.

4

Experimental set-up

The experimental set-up consists of the following main components:

- A wind-wave tunnel with a turbine to generate wind
- A pulsed laser pointing downwards from the top through the air and water
- Two cameras looking cross-wind to observe the tracer distribution in the air and water, respectively
- An optical set-up to form a focused laser sheet
- Readout and trigger electronics

In the following, I will first describe the main components in sec. 4.1 and then, before explaining their deployment in sec. 4.3, I will present some theoretical considerations regarding the optimal arrangement and systematic limitations in sec. 4.2. Finally, I will explain two methods to verify and monitor the beam profile in-situ in sec. 4.4.

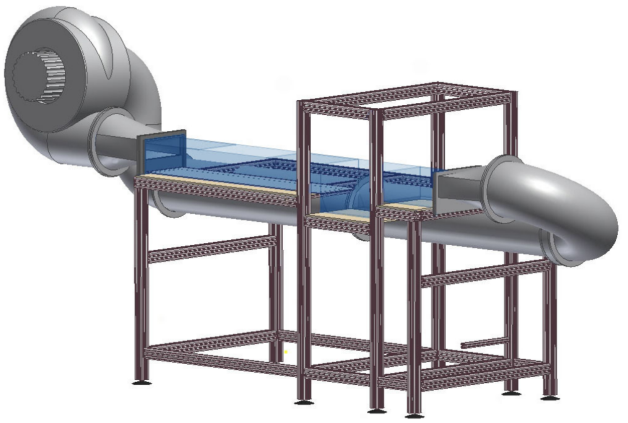

Figure 4.1
Overview sketch of the wind-wave tank with the turbine to the left, the experimental section, and the tubing for air back flow. From *Warken* (2010).

4.1 Main components

4.1.1 Wind-wave tank

The wind-wave facility is described in detail in *Warken* (2010) and *Winter* (2011). Here, I will only summarize the most important aspects relevant for this work. Figure 4.1 shows an overview sketch of the wind-wave tank with the turbine to the left, the experimental section in the center, and the tubing for air back flow. The turbine is fitted with a honeycomb homogenizer to achieve a well defined homogeneous wind profile.

A sketch of the experimental section of the tank is shown in Fig. 4.2 including the geometric dimensions. The total air volume is about $V_{\mathrm{air}} = 220\,\mathrm{L}$ and the water volume at standard filling height of 3.5 cm is $V_{\mathrm{water}} = 23\,\mathrm{L}$. Walls, top, and bottom are made from Schott Borofloat 33©glass allowing for easy optical access. The top lid in the experimental section has two windows made from fused silica glass with high UV transmittance. The laser sheet is introduced through one of them.

Results of experiments to characterize the wind field and water waves under operating conditions are presented in chap. 5.

4.1.2 Pulsed Q-switched laser

A pulsed frequency quadrupled Nd:YAG laser with a wavelength of 266 nm was used as illumination source for LIF. The model CFR200 by Quantel BigSky lasers offers a maximum repetition rate of 20 Hz, a maximum power of 50 mJ / pulse, and a pulse duration of about 8 ns. The laser is actively Q-switched and output power can be adjusted by changing the Q-switch (QS) delay. The relation between the delay value and the output power is non-linear and not specified by the manufacturer, but was characterized in the framework of this thesis (see sec. 5.4). The laser can be externally triggered with a standard TTL signal. An experimental characterization of the laser was performed and is presented in sec. 5.4.

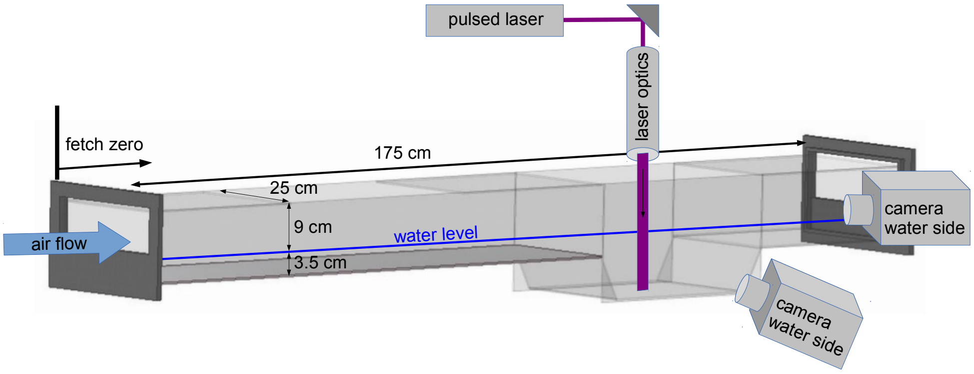

Figure 4.2: Sketch of the experimental section of the tank including the geometric dimensions. Adapted from *Warken* (2010). The cameras' axis is perpendicular to the direction of the wind.

4.1.3 Cameras, lenses, and triggering

Two monochrome scientific CMOS cameras (pco.edge by PCO, Kelheim, Germany) were used in rolling shutter mode to minimize readout noise. This 16 bit camera technology offers very high dynamic range (27000:1) and very low noise (1.1 electrons) at the same time. Both are valuable properties for the purpose of recording the dim air-sided LIF signal in proximity of the bright water surface. Pixel size is $6.5 \times 6.5 \mu m^2$.

Both cameras were controlled with a frame grabber card in exposure control mode. In this modality, the frame grabber issues a high signal during the entire exposure time (35 ms) and a low signal in between frames, thus controlling both, exposure time and recording frequency (2 Hz). The trigger signal was also looped trough a function generator into the pulsed laser. In this way, synchronization was guaranteed and illumination of the entire image was achieved by appropriately delaying the laser trigger on the output channel of the function generator with respect to camera exposure.

On both cameras, a Nikon Micro Nikkor, 105 mm, 1:2.8, was used. For the air-side, aperture was set to 4.0 as a compromise between maximum signal intensity and low optical aberration. For the water-side, an additional Canon 500D close-up lens was used to allow for a sufficiently short working distance of about 20 cm. Since image brightness was less critical than optical aberration, aperture was set to 8.0.

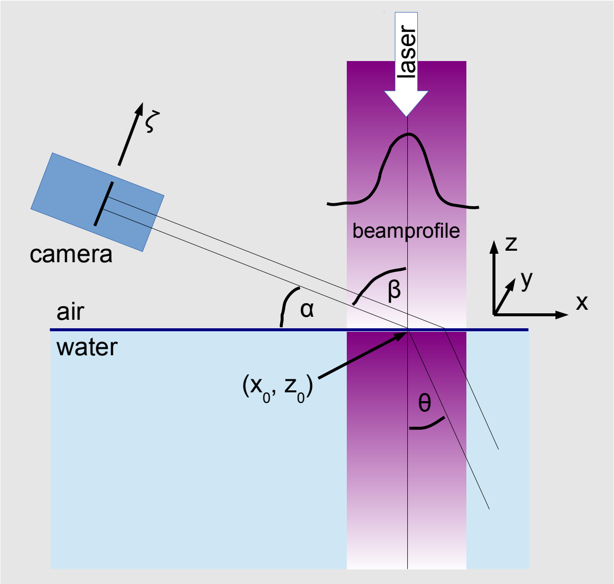

Figure 4.3
Sketch to illustrate the optical refraction at the water surface. The laser sheet is described by a Gaussian profile across and treated as homogeneous in the long direction y.

4.2 Theoretical analysis of optical properties at the water surface

The scope of the air-sided visualization set-up was to obtain acetone concentration distributions as a function height as close as 100 µm to the water surface (see sec. 2.3). To this end, I present a few careful definitions and preliminary considerations which are necessary to define an optimal set-up. A sketch which graphically complements the explanations is shown in Fig. 4.3 with flat water for simplicity.

Acetone vapor in the air is excited by laser light shaped to a sheet of finite length and width. As reasonable approximation, I assume the sheet to be homogeneous in the long direction and Gaussian shaped in the short cross-direction. The width in Fig. 4.3 is exaggerated for clarity. The camera observes the scene as a projection of fluorescent light across the laser sheet onto the camera sensor along the light-of-sight.

Profiles should be expressed in terms of relative height above the wavy water surface. As origin for this coordinate system, the intersection of the water surface and the central laser sheet plane, (x_0, z_0), is an appropriate choice. The coordinates x and z in the laboratory frame are related to the vertical coordinate on the camera sensor by $\zeta = \cos z$ and $\zeta = \sin x$. To avoid optical shading by wave crests adjacent to this point, the camera needs to point downwards by some angle α. In such a setting, even for a point with $z > z_0$, light originating from the water will be projected onto the camera sensor, as seen in Fig. 4.3, overlaying in this way the air-sided signal. Given the solubility of acetone of $\alpha_H \approx 750$ (see sec. 3.1.4), the water-sided tracer concentration, and thus the fluorescent brightness density, is expected to be 750 times higher than in the air leading to a very high dynamic contrast in the image. The recorded air-sided profiles are therefore biased below a certain minimal distance from the water surface which depends on laser sheet width σ and viewing angle α. Also, the refraction at the water surface will pose a limit on the precision by which the point (x_0, z_0) can be determined from the images.

To analyze and quantify this systematic effect, I calculated the attended brightness observed by the camera based on a modeled fluorescent light distribution as follows: The shape of the beam profile is described by a Gaussian function of width σ and the brightness decay in the water is modeled by a mono-exponential function with characteristic scale z^*. The problem is treated as homogeneous in the direction parallel to the long axis of the laser sheet (y-axis in Fig. 4.3).

The fluorescent brightness density in the water is then given by

$$F(x,z) \propto \exp\left(-\frac{x^2}{2\sigma^2}\right) \cdot \exp\left(\frac{z}{z^*}\right), \tag{4.1}$$

with the origin at (x_0, z_0). This brightness density is projected onto the water surface under an angle θ, defined through Snell's law of refraction ${}^{\sin(90°-\alpha)}\!/_{\sin(\theta)} = n_\text{water}$, with $n_\text{water} = 1.33$ the refractive index of water. This can indeed be solved analytically by appropriate straight forward substitution of variables and completion of the square, but since the calculation is lengthy and irrelevant for the conclusion, I only state the result.

The projected fluorescent brightness P^w at a point x_s on the water surface is

$$P^\text{w}(x_\text{s}) \propto \frac{1}{b}\sqrt{\frac{\pi}{2}} \exp\left(-\frac{x_\text{s}^2}{2\sigma^2} + \frac{a^2}{2b^2}\right) \cdot \operatorname{erfc}\left(\frac{a}{b\sqrt{2}}\right), \tag{4.2}$$

with $a = {}^{x_\text{s} \sin\theta}\!/_{\sigma^2} + {}^{\cos\theta}\!/_{2z^*}$ and $b = {}^{\sin\theta}\!/_{\sigma}$.

For the air side, I used Deacon's model, described in sec. 2.3, for a friction velocity of $u_* = 20\,\text{cm/s}$ and modulated the light intensity in x-direction according to the Gaussian laser sheet profile. After sec. 2.5, the surface concentration is set to half the bulk value, $c_\text{s} = 0.5c_\text{b}$ as an estimate. I calculated the projected fluorescent brightness P^a numerically by interpolating and summing in the direction given by the angle α.

The vertical brightness profile observed by the camera is then given by a superposition of P^w and P^a. Following the considerations further above, the water-sided surface brightness density is set to $\alpha_\text{H} = 750$ times the air-sided bulk brightness density.

At this point, it still has to be considered that only a portion of the light originating from the water is transmitted through the surface while another portion is reflected. Therefore, the transmittance T, following from Fresnel's equation for dielectric media, has to be applied as an additional factor. With the here defined angles, this is given by (*Jackson*, 1998)

$$T = \frac{\tan\theta}{\tan\beta} \cdot \left[\left(\frac{2n_\text{water}\cos\theta}{n_\text{water}\cos\theta + \cos\beta}\right)^2 + \left(\frac{2n_\text{water}\cos\theta}{\cos\theta + n_\text{water}\cos\beta}\right)^2\right]. \tag{4.3}$$

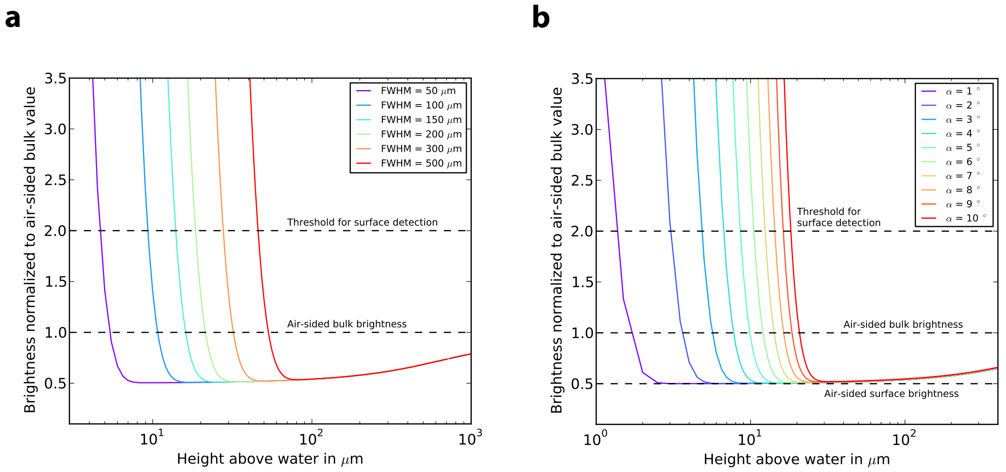

Figure 4.4: Selection of brightness profiles observed by the camera, (a) for a viewing angle of $\alpha = 5°$, a decay scale of $z^* = 200\,\mu\text{m}$, and varying laser sheet thickness, and (b) for a full width at half maximum (FWHM) of 80 µm and varying viewing angle.

The brightness profile observed by the camera is then

$$P(\zeta) = P^{\mathrm{a}}(\zeta) + \alpha_{\mathrm{H}} \cdot T \cdot P^{\mathrm{w}}(\zeta). \qquad (4.4)$$

In Fig. 4.4 (a), I show a selection of such profiles for a viewing angle of $\alpha = 5°$, a realistic decay scale of $z^* = 200\,\mu\text{m}$, and varying laser sheet thickness. The profiles are normalized to the air-sided bulk brightness and for clarity, only a section close to the water surface is shown. The plot underlines the importance to adequately focus the laser in order to record an unbiased brightness as close to the surface as possible. For the set-up used in this work, beam profile measurements yielded a FWHM of the laser sheet of about 80 µm, i.e. $\sigma = 35\,\mu\text{m}$ (see sec. 4.4), and the observing angle was $\alpha = 5°$.

Figure 4.4 (b) show the brightness profiles observed by the camera for a FWHM of 80 µm and varying viewing angle. The following conclusions can be drawn from this plot. First, the surface can be defined to very good precision by a simple threshold criterion, indicated as a dashed line. The implementation of the automatic surface detection is explained in sec. 7.1.3. Second, given the dependence on the viewing angle with respect to the water surface, the precision with which the position (x_0, z_0) can be estimated is intrinsically limited in the presence of waves regardless of the surface detection algorithm. For the here used realistic laser sheet width and admitting the non-ideal conditions in a real experiment, the zero point in a profile should anyhow be precise up to a few ten µm. Third, the observed minimal air-sided brightness close to the surface does not significantly depend on the viewing angle so that the presence of waves should not have any relevant influence.

It should be noted that in the eventually employed set-up, the laser was tilted with respect to the mean water surface in order to be perpendicular to the camera

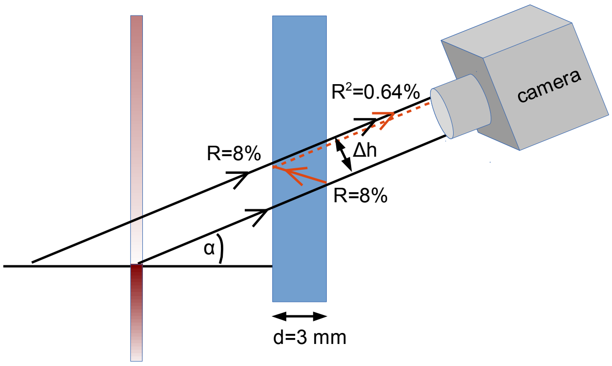

Figure 4.5
Sketch to illustrate the effect of optical ghosting at the side glass pane of the wind-wave tank. The non-zero reflectivity leads to double internal reflections that appear shifted in height in the camera image.

axis (see sec. 4.3.1). This slightly changes the geometrical consideration presented here. As the length of the projection integral within the slanted water-sided laser sheet in this case decreases, the projected light intensity originating from the water is systematically lower. The estimates on the minimal unbiased distance observable in the air given here can thus be regarded as upper bounds.

The recording optics introduce some optical aberration, especially at the open aperture end. This blurring will cause the harsh brightness gradient at the surface to be slightly washed out. Regardless, of the refractive properties at the surface, additional interference with the air-sided signal is therefore expected.

The pulsed CFR200 UV laser used in this work does not have a Gaussian beam profile (see sec. 5.4.1), but shows higher spatial modes resulting in non-zero irradiance even at greater lateral distance from the focus ($> 5\sigma$). To suppress this effect, I used a spatial filter set-up explained in sec. 4.3.2. Beam profile measurements showed that the resulting laser sheet was indeed very clean in the focal plane (see sec. 4.4) so that the principle conclusions drawn from the theoretical analysis presented in this section should safely apply also for the real laser set-up.

4.3 Deployment

In the following, I explain the deployment of the various components at the wind-wave facility along with some optical considerations. Related overview sketches of the set-up are shown in Fig. 4.2 and Fig. 4.6.

4.3.1 Optical ghosting and air-sided camera

Optical ghosting occurs at the sidewalls of the wind wave tank due to double reflection within the glass panes. This is illustrated in Fig. 4.5. For the reflectivity at 450 nm wavelength (blue fluorescent light) of Borofloat 33 glass of 8 %, still 0.64 % of the initial brightness reaches the camera after being reflected twice within the 3 mm thick panes. As a result, the camera captures a second “ghost” scene attenuated by about a factor 100, shifted upwards by $\Delta h = 2d\tan(\alpha)$, which for $\alpha = 5°$ would

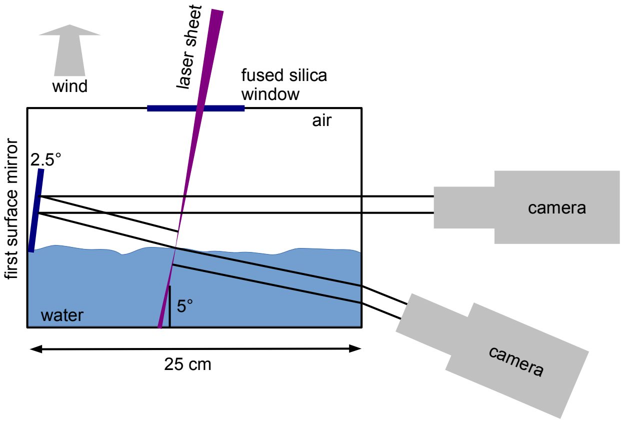

Figure 4.6
Sketch of the camera set-up in a cross-sectional, i.e. long-wind view. Drawing is not to scale.

amount to $\Delta h = 0.5\,\text{mm}$. On the other hand, the brightness contrast at the water surface for acetone is typically also on the order 100. This seemingly negligible optical effect can therefore significantly modify the observed air-sided brightness profile. As a remedy, the camera was positioned with its optical axis perpendicular to the tank wall because in this case, $\tan(\alpha = 0) = 0$, and image and ghost image precisely overlap. To anyhow observe the water surface under a slanted viewing angle of 5°, a first-surface mirror was positioned on the opposite sidewall of the tank with an angle of 2.5°. This is shown in Fig. 4.6.

Magnification of the air-sided camera was 21.2 µm/px with a field of view of $21 \times 54\text{mm}^2$. The extension in the vertical direction was necessary to capture the entire turbulent boundary layer whose thickness under the used conditions was about 40 mm (see sec. 5.1).

4.3.2 Laser set-up and spatial filtering

The laser was formed to a slightly divergent sheet of average length 10 mm and focused to the water surface. The optical set-up is illustrated in Fig. 4.7. A sheet (2D) was preferred over a beam (1D) geometry for several reasons. First, focusing the laser in two directions rather than only one would have led to a much higher irradiance and consequently difficult to treat saturation effects (cf. sec. 3.1.5). Second, images obtained with a laser sheet contain valuable two-dimensional information, e.g. about the surface shape. Third, in particular on the water-side, a sheet geometry facilitates surface detection because the total reflection is visible at every point (cf. sec. 7.2.1). For a thin laser beam, on the other hand, this is not always the case at higher winds impeding easy detection (*Friedl*, 2013).

Focusing and sheet formation was achieved with a plano-convex (f=200 mm) and a cylinder lens (f=63 mm), both made from fused silica for UV transmittance. A short-pass filter was placed in front of the laser to remove residual green light (532 nm) remaining after wavelength doubling. A slit filter, placed in the focal plane of the plano-convex lens, helped to filter out higher spatial modes by narrowing

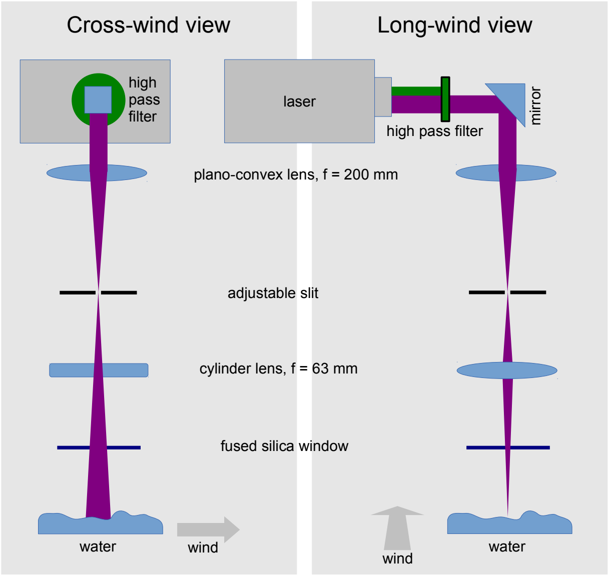

Figure 4.7
Sketch of the optical set-up used to form the laser sheet and to focus it onto the water surface, seen from cross-wind (left) and long-wind (right) direction.

down the slit width (note that the focal plane is equivalent to the optical Fourier plane). This led to a cleaner beam profile and effectively minimized brightness halos in the focal plane on the water surface.

For technical reasons, the laser was positioned horizontally and deviated downwards by a mirror. The two-axis mirror mount also allowed to precisely align the laser beam with the central axis of the optical set-up. While the distance between plano-convex lens and slit had to be kept fixed for the spatial filter to work properly, the cylinder lens could be displaced to focus the sheet onto the water surface.

The laser sheet was slanted by 5° to be oriented perpendicular to the air-sided camera axis. This allowed for a sharp image at any height despite the shallow depth-of-field given the large aperture of 4.0. For the purpose of recording mean concentration profiles, a slanted laser sheet is absolutely admissible since the scalar transport is assumed to be statistically homogeneous in the cross-wind direction. This also allowed to avoid optical components such as a Scheimpflug set-up which in this case would not have brought any advantage yet significant technical complications.

4.3.3 Water-sided camera

The camera was mounted beneath the water level pointing upwards by 15°, corresponding to 11.5° in the water due to refraction at the sidewall of the tank. According to the wave slope measurements presented in sec. 5.3, this value guaranteed optical shading by waves not to occur. As an additional advantage of air-sided mirror set-up (cf. sec. 4.3.1), the laser sheet was slanted towards the water-sided camera rather than away from its axis, thus improving the depth-of-field. This is clear from Fig. 4.6. Magnification of the water-sided camera was 12.0 µm/px with a field of view of $12 \times 31 \mathrm{mm}^2$.

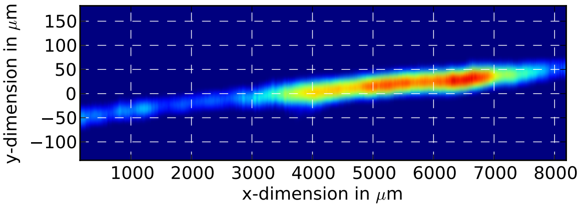

Figure 4.8
Profile of the laser sheet recorded in-situ with a PCO Sensicam UV. From a Gaussian fit, the across-width was determined as $\sigma = 35\,\mu\text{m}$ or a FWHM of 82 µm.

4.4 Beam profiling

In sec. 4.2 I showed that a well-focused laser sheet is important in order to avoid the water-sided fluorescence to systematically bias the air-sided measurements. To assess the performance of the laser optics, beam profiles were measured in-situ in two ways.

In a first approach, a UV sensitive camera (PCO Sensicam UV) was mounted inside the empty wind-wave tank facing upwards at the position of the laser sheet. The vertical position of the camera was adjusted so that the sensor plane matched the mean water level. Neutral density filters were placed in front of the bare sensor without any other optics. In this way, the Sensicam effectively served as a beam profiling unit. A recorded profile image in shown in Fig. 4.8. Although the pixel resolution is limited to 8 µm, this allowed to estimate the quality of the beam focus. From a Gaussian fit, the across-width was determined as $\sigma = 35\,\mu\text{m}$ or a FWHM of 82 µm.

To obtain a qualitative impression of the beam profile prior to an experiment with the entire set-up mounted, an Allied Vision Guppy F503B Pro camera with a 50 mm lens was placed on the cover lid of the experimental tank section and pointed downwards to observe the water surface through the second window. Some acetone was given into the water together with ascorbic acid as strong absorber in the UV regime. In this way, laser light was absorbed quickly and fluorescence light was emitted only from the uppermost surface layer. The laser imprint on the water could then easily be observed with the camera from above providing an in-situ measured laser sheet profile. I used this auxiliary set-up as guidance for fine-tuning the laser optics.

5
Auxiliary experiments

To be able to compare the experimental results of this thesis with data of other studies and with numerical simulations, it was desirable to retrieve certain fluid mechanical parameters characteristic for the used wind-wave tank. In particular, knowledge of the wind profiles provided the air-sided friction velocity which in turn served as characteristic scale. For the wave field, the slope distribution and the typical wave amplitudes were determined from which mean square slope (mss) could be calculated. A wave age parameter was determined with the help of the estimated wave phase speed.

Additionally, the pulsed laser system used in this work was characterized in terms of output power and intensity fluctuations.

5.1 Wind profiles

A simple and well-established instrument to measure flow velocities in the air is the so-called Pitot tube. Essentially, it measures the stagnation pressure at the tip and the static pressure along the side walls. From their difference, the air speed can be calculated following Bernoulli's law. A step-motor driven vertical translation stage allowed to automatically record wind speed profiles in steps of 1 mm for the entire ranges of wind turbine settings used in this work. A collection of such profiles is shown in Fig. 5.1 (a).

To determine the friction velocity u_*, a fit to the data in the range of the logarithmic sublayer would be necessary according to eq. (2.21). This would require wind speed data to be available below 5 to 7mm which in the presence of waves is not possible. Instead, the self-similar properties of the outer wake portion of the turbulent boundary layer were exploited to match wind profiles at different wind

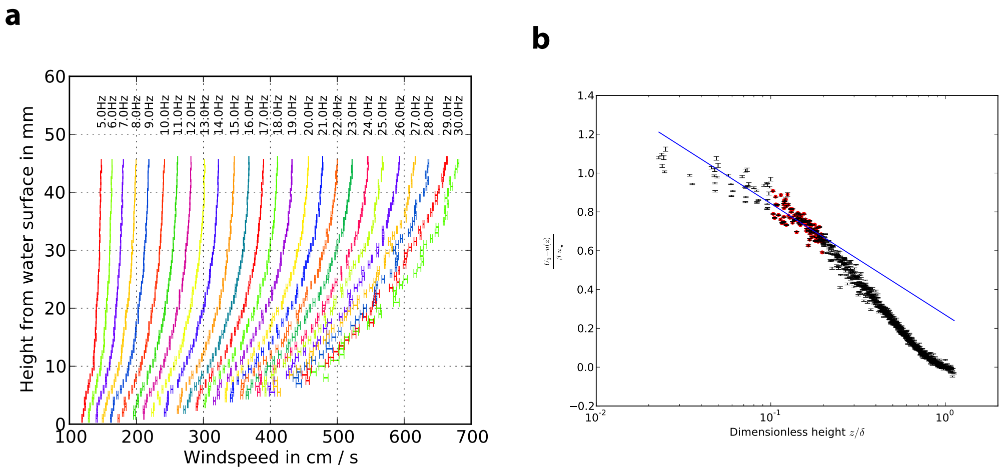

Figure 5.1: (a) Wind speed profiles as a function of height above the mean water surface measured with a Pitot tube. (b) Scaled wind speed profiles $(U_0-u(z))/\beta u_*$ as a function of dimensionless height $\eta = z/\delta$ above the mean water surface measured with a Pitot tube. The plot shows data points from a total of 25 profiles for bulk wind speeds ranging from 150 to 650 cm/s.

speeds and to recover u_* from a simultaneous fit. This approach is used e.g. in *Troitskaya et al.* (2010).

In a first step, according to eq. (2.17), the following function was fitted to the data $u(z)$:

$$u(z) = U_0 - \beta u_* \left(z - \delta\right)^2, \tag{5.1}$$

with the free parameters U_0, (βu_*), and δ, where the latter determines the overall thickness of the turbulent boundary layer. While the wake portion of the profile readily provides the bulk velocity U_0, u_* alone may not be extracted.

By scaling the wind speed profiles with the determined wake parameters, i.e. $U_0 - u/\beta u_*$ as a function of z/δ, they collapse onto each other, underlining their self-similar properties. This is shown in Fig. 5.1 (b). The following logarithmic expression was fitted to the scaled profiles simultaneously:

$$\frac{U_0 - u(\eta)}{\beta u_*} = \frac{1}{\beta}\left(\frac{U_0}{u_*} - \frac{1}{\kappa}\log(\eta)\right) = -\frac{1}{\beta\kappa}\log\left(\frac{\eta}{\eta_0}\right), \tag{5.2}$$

with κ the von Karman constant, and β and η_0 free fit parameters. For each wind speed, u_* was calculated from the wake portion as $u_* = (\beta u_*)/\beta$. The roughness parameter $z_0 = \delta \cdot \eta_0$ was calculated as

$$z_0 = \delta\eta_0 = \delta \exp\left(\frac{\kappa U_0}{u_*}\right). \tag{5.3}$$

It should be noted that by this method, the friction velocity u_* is not directly determined from the logarithmic sublayer for higher wind speeds, but effectively

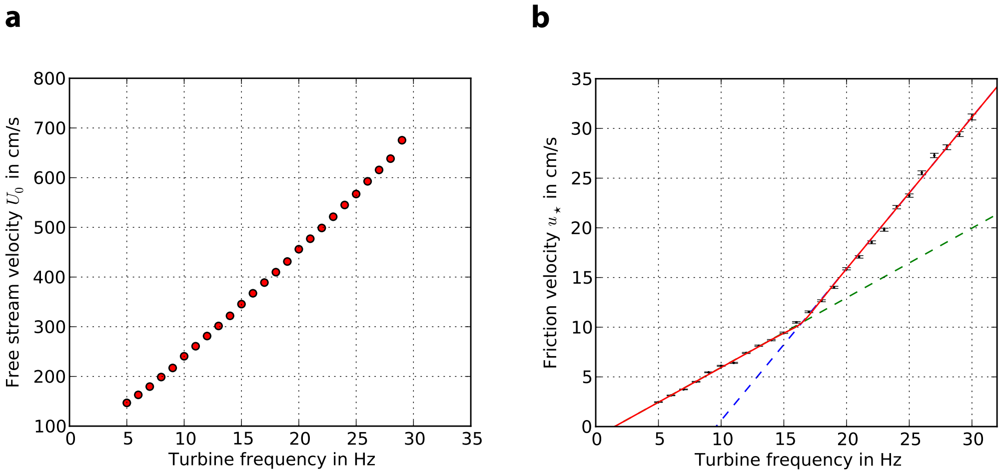

Figure 5.2: (a) Free stream velocity U_0 as a function of turbine frequency. (b) Friction velocity u_* as a function of turbine frequency f_{wind}.

extrapolated based on the self-similar scaling properties of the turbulent boundary layer. An explicit experimental determination would require, e.g., PIV measurements which were beyond the scope of this work. For the purpose of establishing u_* as scaling parameter, the here outlined approach was sufficient.

The left panel of Fig. 5.2 shows U_0 as a function of turbine frequency f_{wind} with a nearly linear relation. The right panel depicts u_* as a function of the turbine frequency f_{wind}. The value of u_* starts to grow stronger with turbine frequency at around $f_{\mathrm{wind}} = 15\,\mathrm{Hz}$ which can be attributed to the onset of waves and the increased momentum dissipation. This is indicated in the figure by the two linear functions chosen to match at the transition point.

Figure 5.3 shows the roughness parameter z_0 (a) and the thickness of the turbulent boundary layer δ (b) as a function of turbine frequency. Again, the increase starting at around $f_{\mathrm{wind}} = 15\,\mathrm{Hz}$ coincides with he onset of waves and demonstrates how the increased roughness acts as a source of turbulence. This tendency played an important role in the interpretation concentration profiles at higher wind speeds.

5.2 Wave-age

As another characteristic parameter, the wave-age c/u_* was determined for turbine frequencies above $f_{\mathrm{wind}} = 21\,\mathrm{Hz}$ by relating the friction velocities to the wave's phase velocity. The latter was measured by observing the time needed for a wave to travel a predefined, marked distance in the wind-wave tank. For all turbine settings, the wave-age was found to be on the order of $c/u_* \approx 1-2$. This parameter was particularly useful for the comparison of experimental concentration profiles with the results of numerical simulations of the turbulent flow of a wavy surface.

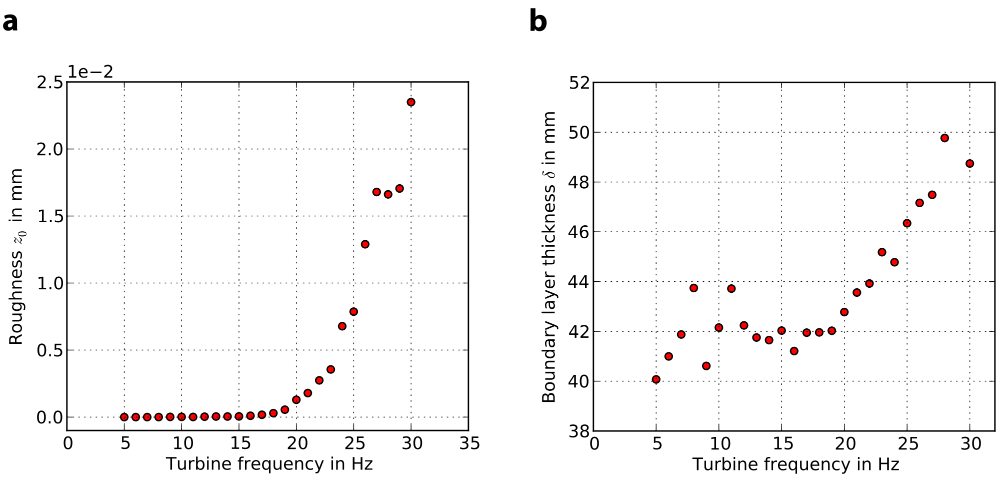

Figure 5.3: (a) Roughness parameter z_0 as a function of f_{wind}. (b) Thickness δ of turbulent boundary layer as a function of turbine frequency f_{wind}.

5.3 Wave slope measurements

For the air-sided turbulent flow, the wavy water surface acts as a rough moving boundary. To estimate its impact on the flow at least qualitatively, the characteristic steepness of the waves for a given wind speed is needed. For the water-sided near-surface flow wave slopes provide a way to qualitatively compare to results of numerical simulations and to estimate the occurrence of micro-scale wave breaking. Various techniques are available to visualize the momentary wave slopes, even over an entire 2-dimensional surface patch (*Balschbach*, 2000; *Rocholz*, 2008). For the mere purpose of obtaining statistical slope distributions, the well-established technique called laser-slope-gauge (LSG) was used (*Lange et al.*, 1982; *Tober et al.*, 1973). The experimental work was performed within a bachelor thesis that I supervised during my PhD (*Platt*, 2011) and I refer to that document for a detailed description. Here, I will only outline the peculiarities of the experimental implementation at the wind-wave tank and report the results relevant for this thesis.

The principle of a LSG is to have a laser beam penetrate the wavy water surface from the air-side and to visualize its impinging point underneath the tank (through the glass bottom) on a frosted glass pane. The lateral deviation $(\Delta x, \Delta y)$ from the center point depends on the water surface slope and the water height at the point of penetration. To account for the latter, in general, a telecentric optical set-up is used between the bottom of the tank and the frosted glass pane. As the small amplitudes of up to 3 mm occurring in the wind wave tank at maximum wind speed induce a negligible systematic error, this optical element was avoided.

Typically, an LSG is implemented in a radiometric fashion in so far as the camera integrates accumulated brightness at each point on the frosted pane. This will be proportional to the probability of the laser to imping the pane in this particular coordinate, i.e. to the related water surface slope. This approach, however, requires

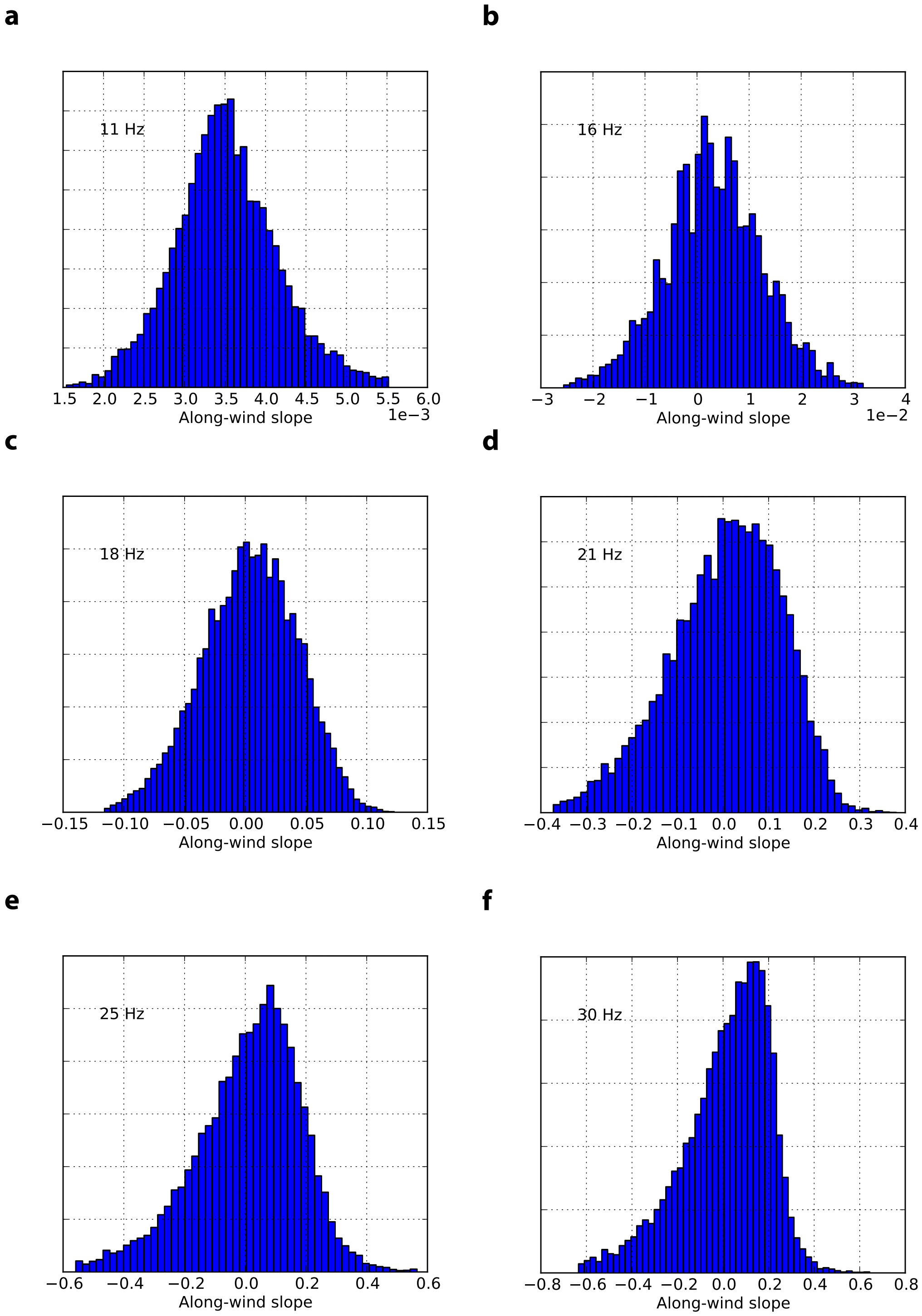

Figure 5.4: (a)-(f) Exemplary wave slope distributions, along-wind, for different settings of the wind turbine. Slopes ak begin to be appreciable at around 15 Hz. In (e) and (f), the skewness is quite noticeable, manifesting the appearance of small scale gravity and capillary waves.

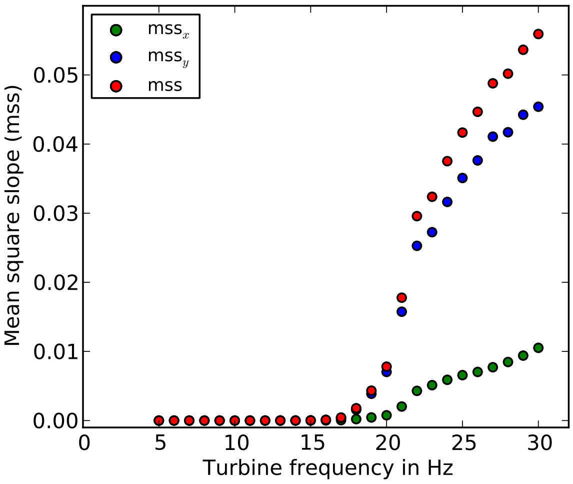

Figure 5.5
Mean square slope as a function of turbine velocity f_{wind}. Slopes grow rapidly above $f_{\text{wind}} = 15\,\text{Hz}$, consistent to the development of the surface roughness and thickness of the turbulent boundary layer δ shown in Fig. 5.3.

a precise radiometric calibration of the camera set-up and of the emission characteristics of the frosted glass. To avoid this complication, we measured in a binary, position-detection mode. The camera was operated at a sufficiently short integration time of $T = 10\,\text{ms}$ to minimize motion blur. The laser was set to maximum power to deliberately saturate the image around the center of the laser spot on the frosted glass to allow for a simple threshold-based detection and segmentation. For each image, the center of mass (center of mass)center of mass\relax of the spot was then easily retrieved and a series of images yielded a series of lateral deviation $(\Delta x, \Delta y)$. Local curvature of the water surface generally leads to geometrical distortion of the laser beam profile at the point of penetration. This will cause the laser spot on the frosted pane not to appear circular, as assumed by the coordinate determination based on the center of masscenter of mass\relax . To avoid this effect, the laser was focused on the water surface to a FWHM of about 100 μm, which was smaller than the typical scales of surface curvature, $\sqrt{\left({}^{\partial^2\eta}/_{\partial x_i \partial x_j}\right)^{-1}}$.

Figure 5.4 shows a series of exemplary along-wind slope distributions for different settings of the wind turbine frequency f_{wind}. Up to about $f_{\text{wind}} = 16\,\text{Hz}$, the water surface is merely undulated and slopes are below $ak = 0.01$. For higher wind speeds, slopes rapidly increase and reach values of $ak \approx 0.2$. This is in coherence with the observed wind speed profiles and the flow parameters deduced thereof in sec. 2.2. From about $f_{\text{wind}} = 21\,\text{Hz}$ onwards, skewness of the slope distributions becomes apparent. This is to be attributed to the appearance of small scale gravity and capillary waves and their characteristic asymmetric shape. Together with observations of the wave field by eye, this suggests that micro-scale wave breaking might set-in in this regime.

The parameter mss is essentially defined as the variance of the slope distribution. Its dependence on wind speed is shown in Fig. 5.5, where the along-wind, cross-wind, and total mss is depicted. This is in excellent agreement with the measured

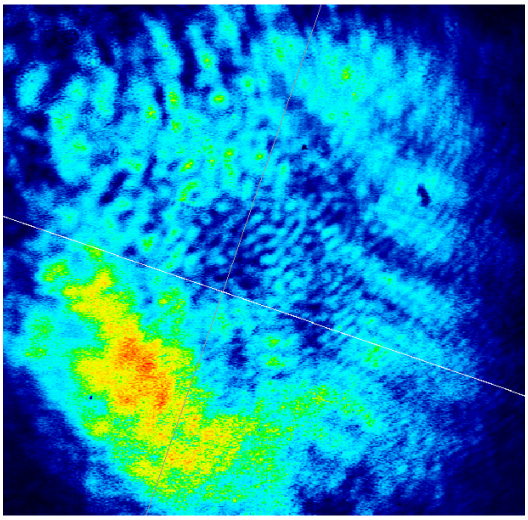

Figure 5.6
Lateral unfocused beam profile of the CFR200 pulsed UV laser measured with a Dataray WinCamD beam profiler. The overall diameter is about 5 mm.

roughness parameter z_0 and the air-sided boundary layer thickness δ in Fig. 5.3. Cross-wind mss reaches a maximum of 0.01 at $f_{\mathrm{wind}} = 30\,\mathrm{Hz}$, corresponding to a slope of $ak = 0.1$. This serves as a lower limit for the optimal air-sided camera viewing angle (see sec. 4.3.3).

5.4 Characterization of the pulsed UV laser

As light source for the LIF experiments, a pulsed Q-switched laser[1] was used (see sec. 4.1.2). To provide quantitative information for an efficient design of the experiments, the laser was characterized in terms of beam shape, power output, and intensity fluctuations.

5.4.1 Beam profile

To measure the lateral beam profile, a UV sensitive beam profiler (Dataray WinCamD) was used[2]. A combination of several absorbing and reflecting filters was needed to attenuate the intensity of the laser in order to avoid damage to the beam profiler sensor. Figure 5.6 shows the profile of the unfocused beam with an overall diameter of 5 mm at about 50 cm distance from the laser head.

The non-uniform, non-Gaussian shape of the profile is evident and indicates the existence of multiple higher spatial modes. In terms of Fourier optics, these show up in the focal plane as higher order maxima around the center of the focused beam. To anyhow obtain a clean laser sheet profile, I used a spatial filter set-up, as explained in sec. 4.3.2. I also verified the quality of the beam focus in-situ before every experiment (see sec. 4.4).

---

[1] Model CFR200 by Quantel Lasers

[2] In kind collaboration with Dr. Andreas Rudolf of TU Darmstadt/GRK-1114

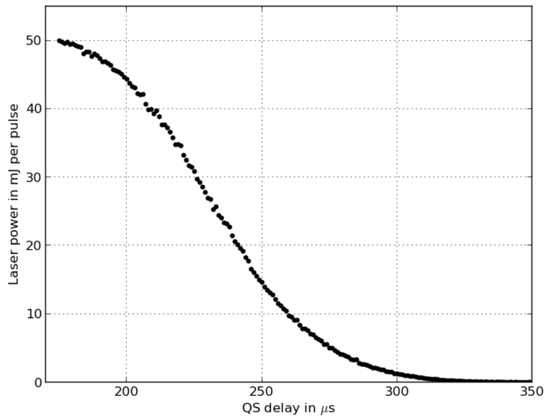

Figure 5.7
The dependence of the induced fluorescent brightness of a white paper target illuminated with the pulsed UV laser was measured. By relating the maximum brightness to the maximum energy output of 50 mJ/pulse, this provided a one-point calibration of the laser power output in terms of Q-switch delay.

5.4.2 Power output

The power of a Q-switched pulsed laser can be modulated by adjusting the QS delay with respect to the flash pump (see sec. 4.1.2). The correspondence is in general non-linear and not specified by the manufacturer of the laser system. To estimate, e.g, the effect of saturation, it was desirable to obtain a calibration curve to relate QS delay to laser output power. In principle, the output power of a laser system can be determined with the help of a so-called power meter which in essence measures the increase in temperature on an internal surface due to the impinging laser beam. In the case of the pulsed UV laser used in this thesis, the maximum spatial power density would have exceeded the destruction threshold typically indicated by the manufacturer. Indeed, the maximum power output can be estimated as $^{50\,\mathrm{mJ}}/_{8\,\mathrm{ns}} \approx 6 \times 10^5\,\mathrm{W}$ for a pulse length of 8 ns. Assuming a circular profile of radius $r = 2.5\,\mathrm{mm}$, this amounts to an average spatial power density of $3 \times 10^5\,\mathrm{W/mm^2}$. Instead, the output power calibration was performed in the following alternative way. The laser beam was expanded by a concave fused silica lens to a diameter of about 1 m, reducing the maximum averaging power density to only $8\,\mathrm{W/mm^2}$, and shone onto a standard white paper sheet. Due to the presence of optical brightening agents, commercial paper emits blue fluorescent light induced by UV radiation, which for the expanded beam could safely be assumed to be proportional to the incident laser power. The emitted fluorescent light was recorded with a camera and the average image brightness was determined as a function of Q-switch setting of the laser. By relating the maximum brightness value to the highest nominal energy output of 50 mJ/pulse, this provided an effective one-point calibration, shown in Fig. 5.7.

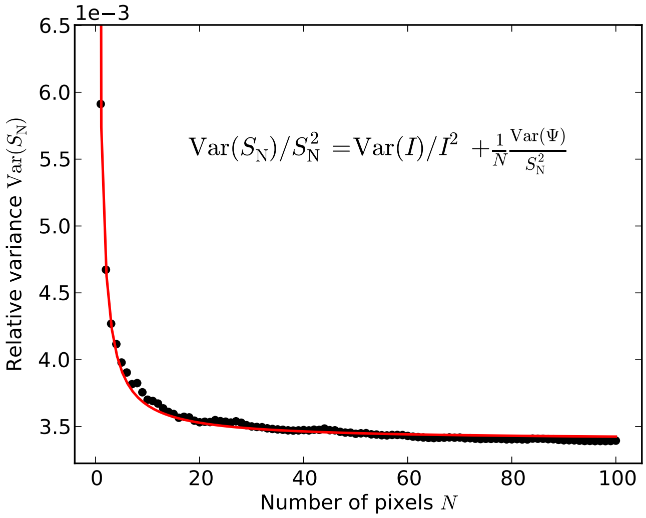

Figure 5.8
The variance of the image brightness over an otherwise homogeneous fluorescent scene was determined by first calculating the average over N pixels in each individual image. While the camera noise contribution decays with $1/N$, the contribution due to laser intensity fluctuations is constant in each image.

5.4.3 Intensity fluctuations

The calibration routine for the air-sided images required a brightness-based matching to reference images. To minimize inaccuracies in this procedure due to variable illumination, it was useful to quantify the intensity fluctuations of the laser system. To this end, the set-up explained in sec. 4.3 was used. In general, the brightness variation over a series of images originates from different independent sources of fluctuations. Based on the following rationale, the contribution of the laser could nonetheless be extracted.

The image brightness S can be thought of as a sum of fluorescent signal $I \cdot c$ and some camera noise Ψ, i.e.,

$$S = I \cdot c + \Psi, \tag{5.4}$$

with $\langle S \rangle = \langle I \cdot c \rangle$ and $\langle \Psi \rangle = 0$. Here, $\langle . \rangle$ indicates the average over a long series of images. Consequently, the variance is given as

$$\mathrm{Var}(S) = c \cdot \mathrm{Var}(I) + \mathrm{Var}(\Psi), \tag{5.5}$$

where the acetone gas is assumed to be well-mixed and constant in time, i.e. $\mathrm{Var}(c) = 0$. The second term, indicating the camera noise, is thought to be independent for each individual pixel. Statistically, in terms of camera noise, it is therefore equivalent to average over N different pixels in one single image, or over one single pixel in N images. The laser intensities, on the other hand, are identical for different pixels in one single image. Therefore, the relative variance of the image brightness averaged over N pixels in each image of a series, is given as

$$\mathrm{Var}(\langle S \rangle_{\mathrm{N-pixel}})/\langle S \rangle^2 = \mathrm{Var}(I)/\langle I \rangle^2 + \frac{1}{N}\frac{\mathrm{Var}(\Psi)}{c \cdot \langle I \rangle^2}. \tag{5.6}$$

Following this approach, I recorded a series of 500 images without water in the tank and acetone vapor well-mixed at high turbine frequency. Since the tank was kept closed, the concentration remained constant in time. By fitting eq. (5.6) to the variance data obtained from the 500 images, the relative laser fluctuation could be determined to be about 15 %. This is shown in Fig. 5.8.

6

Experimental procedure

Experiments were conducted as a gas invasion, i.e. the air was initially supersaturated with acetone causing a flux into the water. This chapter briefly describes the procedure of the visualization experiments.

6.1 General procedure

Before each run, the wind-wave tank was thoroughly rinsed to remove any unwanted surfactants which might have accumulated over time and to guarantee for the initial water-sided tracer concentration to be zero. The tank was then filled with fresh, demineralized clean water. The wind turbine was turned on to the desired frequency a few minutes prior to the experiment. Considering the small size and fetch of the tank, this was certainly long enough to assume the wave field to be in equilibrium, as confirmed by observation. Continuous tracer injection was started, as will explained in sec. 6.1.1, and kept on for typically 20 min. In this way, a presumably stationary condition was reached with a roughly constant air-sided concentration governed by the equilibrium of injection rate, flux into the water, and losses to the release tube. Subsequently, injection was stopped, effectively turning the tank into a closed system, and data acquisition continued for typically another 15 min. Concentrations recorded during this phase were used to calculate transfer resistances from mass balance considerations, explained in sec. 7.4. Leakage under neutral pressure conditions was determined by *Niegel* (2013) and could be neglected to about 2-3 % precision.

6.1.1 Tracer injection

Acetone was injected into the back flow tubing of the tank in order that any plume first passed once through the turbine before getting in contact with the water surface in the experimental section. Liquid acetone was filled in a 250 ml bubbling flask through which dry pressurized laboratory air was flushed. To compensate for the strong cooling due to acetone's negative evaporation enthalpy, the flask was kept in an actively temperature-controlled water bath at about 23 ° °C. To keep pressure constant during injection, a release tube was connected to the exhaust system of the wind-wave facility.

Injections rates were determined by measuring the weight difference of the liquid acetone in the flask after 10 min of flushing. Typical values were 11 ml/min or, equivalent at room temperature and atmospheric pressure, 0.13 mol/min. Exact values varied dependent on the filling height of the flask and consequently the rising time of the bubbles. The here given average value is estimated to be precise to about 10 %.

6.1.2 Data recording

The components and their deployment was described in detail in chap. 4. Images of the fluorescent brightness in the water and air were recorded simultaneously. The two cameras were electronically coupled to the pulsed laser for proper synchronization. A recording frequency of $f = 2$ Hz as compromise between data volume and sufficient time resolution. Note that typical decay times after closing the tank could be estimated to be on the order of 1-5 min. For higher recording frequency, the resolved structures in the water would have overlapped from on image to the other. Treating each of them as independent statistical realization would anyhow have been questionable. Temperature was monitored manually and remained constant at 25(1) °C.

6.1.3 Reference images

Reference images (see sec. 3.1.6) were recorded with the same recording procedure. The tank was dried and no water was filled in. Acetone was injected over a course of about 10 min as explained in sec. 6.1.1, while images were recorded. Concentrations, and consequently image brightness, increased at a decreasing rate owing to the losses to the pressure release tube. Afterwards, injection was turned off and the tank was connected to the actively pumped air-exhaustion system causing concentrations to gradually fall back to zero. This is shown in Fig. 6.1. In this way, reference images covered the entire range of concentrations encountered during an invasion experiment.

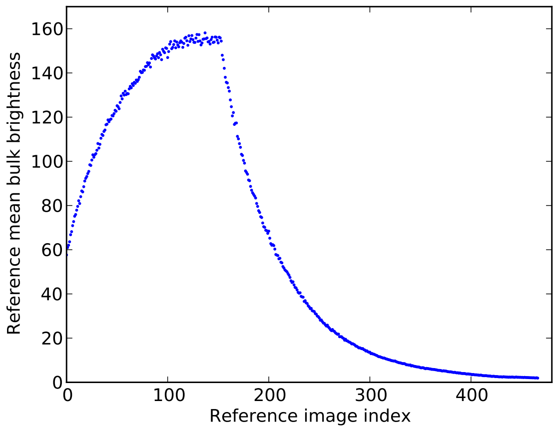

Figure 6.1
Mean bulk brightness of reference images given in gray value (GV).

6.2 Modulated wind conditions

A few experiments were conducted under modulated wind conditions. To this end, the turbine was switch to e pre-chosen low and high setting in periods of 50 s-50 s. Modulation was synchronized to image recording.

6.3 Surfactant: Triton-X

Experiments were conducted to investigate the effect of surfactant on gas exchange and the typical vertical distribution of tracer. As surface active material, Triton-X[1], was chosen. It is a soluble detergent commonly used in laboratories and has been employed in the past in gas-exchange experiments, e.g. by *Krall* (2013); *Kräuter* (2011). An amount of 250 mg was first dissolved in demineralized water and then added to the water in the tank. This quantity was chosen to guarantee effective suppression of waves even at the higher wind speed setting.

---

[1] IUPAC name: polyethylene glycol p-(1,1,3,3-tetramethylbutyl)-phenyl ether

7
Data processing

7.1 Air-sided profiles

The data processing procedure for the air-sided images consists of the following subsequent steps, which I explain in detail in the following sections:

1. To each data image, a matching reference images with homogeneous tracer distribution is selected.
2. From these two, a quotient image is formed which directly provides the relative tracer distribution ${c(x,z)}/{c_\mathrm{b}}$.
3. The water surface is automatically detected in each images with a dedicated low-level image processing routine.
4. From each image, a vertical concentration profile is obtained by horizontally averaging in coordinates relative to the surface.
5. An intrinsic calibration allows to convert relative to absolute concentration values.

7.1.1 Quotient images and relative concentration

After sec. 3.1.2, the local fluorescence brightness intensity depends on the tracer concentration and the laser irradiance. I showed in sec. 3.1.2 that for the pulsed Nd:YAG laser used in this work, small systematic effects of saturation occur close to the focal plane of the laser sheet and in sec. 3.1.6 I explained how this can be effectively accounted for by regarding the relative brightness of two images. For typical tracer concentrations of 1×10^{-3} mol/L, the saturation effect can be described as multiplicative damping term. Here, I explain the implementation of this approach in the data processing routine.

Reference images were recorded without water in the tank as described in sec. 6.1.3. They were averaged over subsequent 20 frames, equivalent to 10 s and the mean bulk brightness was calculated from image pixels corresponding to a fixed reference height about 40 mm above the water. This set of bulk brightness values covered a range from virtually 0 gray value (GV) to about 160 GV in steps of about 1.5 GV (see Fig. 6.1 in sec. 6.1.3).

From each data image, i.e. with water in the tank, bulk brightness was computed for the same image pixels and the reference image with the closest matching value was selected, i.e. $c_{\mathrm{ref}} \approx c_{\mathrm{b}}$. Following from sec. 3.1.6, the ratio of such two images is given as

$$\frac{F(x,z) - \Psi}{F_{\mathrm{ref}}(x,z) - \Psi} = \frac{c(x,z) \cdot I(x,z;c_{\mathrm{b}}) \cdot \mathrm{Sat}(z;c_{\mathrm{b}},P) \cdot \mathrm{Vig}(x,z)}{c_{\mathrm{ref}} \cdot I(x,z;c_{\mathrm{ref}}) \cdot \mathrm{Sat}(z;c_{\mathrm{ref}},P) \cdot \mathrm{Vig}(x,z)} \tag{7.1}$$

Obviously, the non-zero noise signal Ψ of the camera (dark image) was subtracted before calculating the quotient. From here on, I will simply drop the noise term in any equation for simplicity. It should be noted here, however, that any other diffuse background light contributes an additive term to the observed signal and causes the multiplicative factors not to cancel precisely. In other words, background light leads to unwanted residual artifacts in the quotient image so that the visualization technique only works in dark conditions. The $\mathrm{Vig}(x,z)$ factor describes shading by the camera optics, i.e. vignetting. This term automatically cancels in the quotient image and radiometric camera calibrations are unnecessary with this approach. Likewise, the $\mathrm{Sat}(z;c_{\mathrm{b}},P)$ and $\cdot I(x,z;c_{\mathrm{b}})$ terms cancel if $c_{\mathrm{ref}} = c_{\mathrm{b}}$.

Summarizing, relative concentration images were obtained as

$$\frac{c(x,z)}{c_{\mathrm{b}}} = \frac{F(x,z) - \Psi}{F_{\mathrm{ref}}(x,z) - \Psi}. \tag{7.2}$$

An example for air raw image and the corresponding quotient image is shown in Fig. 7.1. Since outside of the laser sheet brightness quickly drops to zero, the quotient image becomes very noisy in that region. Only the inner portion, indicated by the two red lines, is used for further processing.

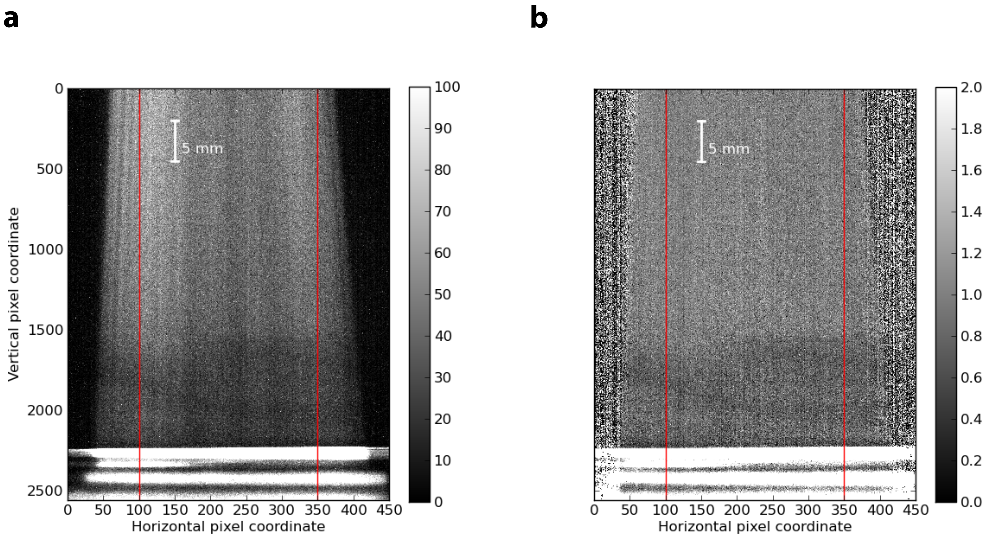

Figure 7.1: (a) Example of a raw image for turbine frequency f_{wind}=11 Hz. Only the image portion contained between the two red lines was used. (b) Quotient image $^{F}/_{F_{\text{ref}}} = {}^{c}/_{c_{\text{b}}}$ obtained by matching the average bulk brightness. Note the large noise on either side of the laser sheet where virtually zero signals are divided. Images are stretched in horizontal direction for clarity.

7.1.2 Relative coordinates and image averaging

Over the wavy water surface, the choice of coordinate system is not unique. A Cartesian laboratory reference frame would suit to represent tracer distribution sufficiently far away from the water. On the other hand, close to the surface on scales similar to the wave amplitudes, it would certainly have a limited physical meaning. A mathematically rigorous choice of reference frame would be curvilinear coordinates, which are locally orthogonal with the vertical axis locally perpendicular to the water surface. This choice would require rather cumbersome geometric image transformations to be determined for each individual image. As wave slopes do not significantly exceed $ak = 0.2$ (see sec. 5.3), the merit of this procedure for the physical interpretation of concentration profiles is anyhow questionable. For this work, I chose an intermediate way in which the vertical coordinate was linearly shifted according to the height of the water surface and the lateral coordinate was kept, i.e.

$$\zeta = z - z_{\text{surf}} \quad \text{and} \quad \xi = x. \tag{7.3}$$

From each image, a profile was calculated by horizontally averaging in this relative coordinate system,

$$c(\zeta) = \sum_{\xi} c(\xi, \zeta). \tag{7.4}$$

Series of images could further be averaged depending on the scope of the specific analysis. For the sake of notational simplicity, I will retain x, z as coordinates instead

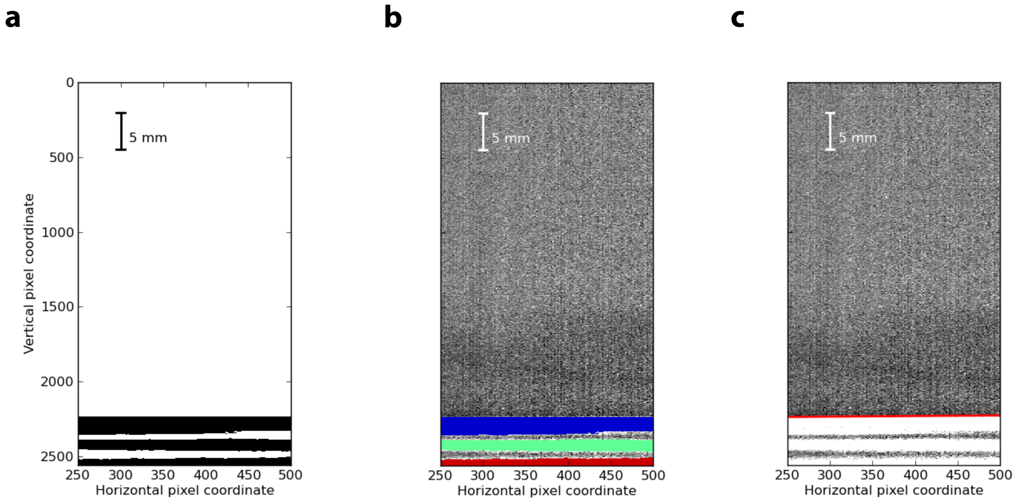

Figure 7.2: (a) Example for an air-sided binary image obtained from a quotient image $^{F}/_{F_{\mathrm{ref}}}$ applying a threshold of 2. (b) The three largest connected objects in the binary image, identified as potential surface candidates. The blue one is selected for its highest center of masscenter of mass\relax . (c) The detected water surface defined as the upper edge of the selected binary object.

of ξ, ζ, implicitly intending relative height with respect to the water surface.

7.1.3 Surface detection

To apply the averaging procedure described above, the water surface needed to be detected in each image. In sec. 4.2, I have shown that the position of the surface is sufficiently well defined based in a threshold criterion. Since the detection was performed on quotient images $^{F}/_{F_{\mathrm{ref}}} = {}^{c(x,z)}/_{c_{\mathrm{b}}}$, values fluctuated around ${}^{c(z)}/_{c_{\mathrm{b}}} = 1$ and a threshold of 2 proved to be robust and effective.

The detection algorithm performed the following successive steps. First, a binary image was created in which pixels with values above the threshold were set to 1 and all others to 0. Connected pixels were joined to objects applying the structure element

1	1	1
1	1	1
1	1	1

The so-identified objects were regarded as potential surface candidates. An example of such a binary image is shown in Fig. 7.2 (a).

Under certain conditions, reflections were visible in the image which could potentially have led to spurious surface detection. Such reflections are seen in Fig. 7.1 (a) and (b) and consequently in the binary image Fig. 7.2 (a). Note that due to the limited resolution of the figures, small structures appear connected to larger ones. The here

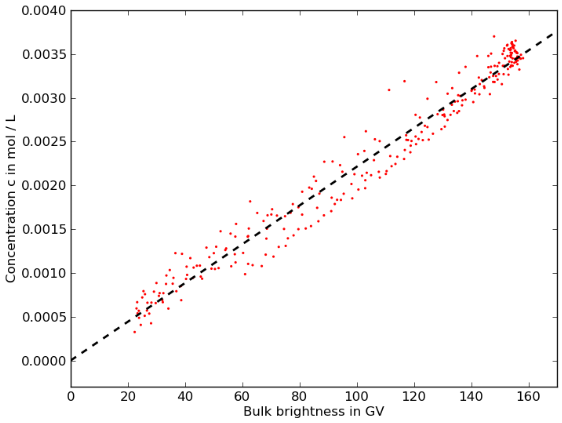

Figure 7.3
Calibration plot relating $F_b'/\epsilon_{air} F_b = c$ to the bulk brightness F_b. For the extinction coefficient, ϵ_{air}=11.7 L/mol/cm was used (*Lozano et al.*, 1992). The dashed line is a linear fit to the calibration data points.

shown binary image actually contains almost 60 separate objects corresponding to pixel values above the threshold. Two selection criteria were applied. First, the surface was expected to be continuous, extending almost across the entire image. The size of the corresponding object in the binary image should therefore be large compared to most reflections. Correspondingly, only the largest five binary objects were admitted as surface candidates. An example is shown in Fig. 7.2 (b). Second, by geometric considerations, reflections could only originate from the water patch between the laser sheet and the camera and thus result in bright spots beneath the height of the water surface in the image. Among candidate objects, the one with the highest center of masscenter of mass\relax was preferred. From this, the physical water surface was determined as the position of their upper edge, as illustrated in Fig. 7.2 (c). The here described algorithm proved to be very robust and detection precision was as good as 1 px.

7.1.4 Absolute concentrations

The reference images provided a simple way to obtain a calibration curve to convert image brightness in physical tracer concentration. This was possible because the camera observed the brightness decay due to Lambert-Beer absorption over a certain height. Since the extinction coefficient is known, the concentration could be derived from this decay.

In the reference images, the tracer concentration is homogeneous and the fluorescent brightness as a function of vertical coordinate is given as

$$F(z) = c_b I(z) = c_b I_0 \exp\left(-\epsilon_{air} c_b z\right) . \tag{7.5}$$

In particular, one can define the bulk fluorescent brightness

$$F_b \equiv F(z_b) = c_b I_0 \exp\left(-\epsilon_{air} c_b z_b\right) , \tag{7.6}$$

where z_b denotes the height of the bulk. The derivative at $z = z_\mathrm{b}$ is then

$$F'_\mathrm{b} \equiv \frac{\partial F}{\partial z}(z = z_\mathrm{b}) = -\epsilon_\mathrm{air} I_0 c_\mathrm{b}^2 \exp\left(-\epsilon_\mathrm{air} c_\mathrm{b} z_\mathrm{b}\right) = -\epsilon_\mathrm{air} c_\mathrm{b} \cdot F_\mathrm{b}. \tag{7.7}$$

In other words, from the relation

$$c_\mathrm{b} = \frac{-F'_\mathrm{b}}{F_\mathrm{b}\epsilon_\mathrm{air}} \quad \longleftrightarrow \quad F_\mathrm{b}, \tag{7.8}$$

a calibration curve can be obtained relating image brightness to concentration. Numerically, the derivative F'_b was calculated as tangent fit to the brightness profile $F(z)$ in the bulk portion of the image. The set of reference images covered the entire brightness, i.e. concentration range encountered in any data image. The obtained calibration curve is shown in Fig. 7.3 together with a linear fit $c = a \cdot F_\mathrm{b}$, with $a = 2.21 \times 10^{-5}$ mol/L/GV.

Absolute concentration profiles could then be calculated from relative brightness profiles and bulk brightness values as

$$c(z) = \frac{F(z)}{F_\mathrm{ref}(z)} \cdot F(z = z_\mathrm{b}) \cdot a, \tag{7.9}$$

with $F(z)$ and $F_\mathrm{ref}(z)$ data and reference profiles, respectively, as in eq. (7.2). One should note that absolute concentrations could also directly be obtained from each single data profile by performing the above described tangent fit in the bulk portion. While both methods in principle yield the same result, this latter approach is less robust due to local fluctuations in single images.

7.2 Water-sided profiles

The data processing procedure for the water-sided images was similar as for the air side and consisted of the following subsequent steps, which I explain in detail in the following sections:

1. The water surface was automatically detected in each image with a dedicated low-level image processing routine.
2. From each image, a vertical fluorescent brightness profile was obtained by horizontally averaging in coordinates relative to the surface.
3. Concentration profiles were calculated by fitting an exponential model combined with Lambert-Beer absorption to the vertical brightness distribution averaged over 16 000 pixel columns corresponding to 10 s time steps.
4. This procedure yielded a time series of surface and bulk concentration as well as characteristic boundary layer scale.

7.2.1 Surface detection and image averaging

To obtain mean brightness profiles, images had to be averaged horizontally across the laser sheet in coordinates relative to the water surface. To this end, the water surface had to be detected automatically in each individual image. This was achieved by low-level image processing departing from the observation that fluorescence is brightest right at the surface and that for the occurring wave slopes, the condition of total reflection was always fulfilled. The principle idea was to identify the surface as the longest (horizontally) and at the same time brightest structure in the image. The implementation of the algorithm is shortly explained in the following.

First, the dark image is subtracted and vignetting is corrected for with a flat field image recorded off an Ulbricht sphere. The image is smoothened to suppress small scale noise and local maxima are determined column-wise and used to form a binary image.

To remove isolated pixels resulting from noise, a Hit-or-Miss filter with the structure element

0	0	0
0	1	0
0	0	0

is applied to the binary image. Since local maxima are determined independently for each column, binary pixels along the water surface might be shifted vertically relative to each other and would therefore not combine to a single labeled structure. Therefore, three consecutive dilatations were applied using the following two structure elements which were adapted to the curvy elongated shape of the wavy surface:

0	0	0
1	1	1
0	0	0

1	0	0	0	1
1	1	1	1	1
1	0	0	0	1

In the dilated binary image, connected pixels are combined to labeled objects and for each of them, the area and mean brightness is determined and normalized to the greatest occurring value, respectively. An example of a structured image is shown in Fig. 7.4 (a) where the fluorescence brightness is given in false colors. The object with the largest sum of normalized area and mean brightness is selected as water surface.

Due to the dilatations, the surface objects were typically 3 to 5 pixels wide and their geometrical centerline was defined as physical water surface to achieve pixel precision. This is shown in Fig. 7.4 (b) for the example image in (a). Taking the centerline as estimate of the surface is reasonable as the brightness is expected to be symmetric around the water surface due to total reflection.

All models for concentration profiles referenced in sec. 2.4 are applicable to mean tracer distributions. On the other hand, invasion of acetone in water takes place

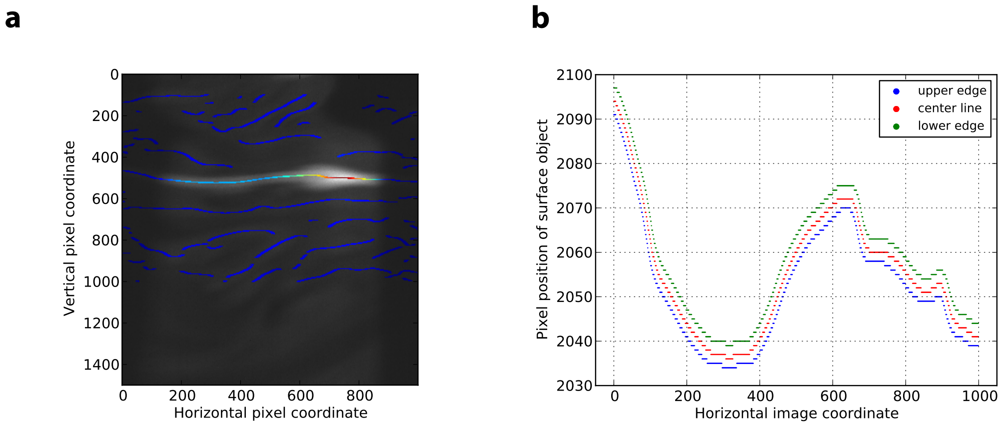

Figure 7.4: (a) Example for a water-sided image with the dilated local maxima overlaid as color image. (b) Upper and lower edge of the surface object and the geometric centerline used as an estimate of the water surface position.

on fairly short time scales, i.e. on the order of minutes. As a compromise, intensity profiles were calculated by averaging horizontally in coordinates relative to the water surface and over 20 consecutive images, i.e. over a total of $20 \times 800 = 16000$ image columns. Only for lower wind speeds of up to $u_* = 10\,\mathrm{cm/s}$ and consequently lower water drift velocities, subsequent images overlapped by about 15 %, but turbulent structures had considerably changed. For higher wind speeds, there was no overlapping between pictures. According to Taylor's principle of frozen turbulence, each mean brightness profile was thus based on 1.6×10^4 realizations of the statistical ensemble describing the turbulent mixing. It was therefore reasonable to apply mean profile models to this averaged, but still temporary data.

7.2.2 Implicit dependence: concentration and fluorescent brightness

In the LIF experiments conducted in this work, the tracer gas acetone is also the absorbing substance at the same time. This is different in studies where a water soluble fluorescent dye is illuminated by a laser and the concentration of some tracer gas, typically oxygen, is measured through the quenching effect (*Friedl*, 2013; *Münsterer and Jähne*, 1998; *Walker and Peirson*, 2008, e.g.). As the acetone concentration decreases further away from the water surface, the Lambert-Beer absorption decreases accordingly yielding a non-monoexponential profile. For an arbitrary concentration profile $c(z)$, the differential irradiance decrease is

$$\mathrm{d}I = -\epsilon I(z) c(z)\,\mathrm{d}z. \tag{7.10}$$

Defining

$$\mathrm{d}\tilde{z} \equiv c(z)\,\mathrm{d}z \tag{7.11}$$

eq. (7.10) can be re-written as

$$\mathrm{d}I(\tilde{z}) = -\epsilon I(\tilde{z})\,\mathrm{d}\tilde{z}. \tag{7.12}$$

Upon integration, this yields the irradiance profile for general tracer distributions,

$$I(z) = I_0 \exp\left(-\epsilon \int_0^z c(z')\,\mathrm{d}z'\right). \tag{7.13}$$

Leaving aside optical vignetting by the objective, which is anyhow corrected for, the camera essentially observes the spatial distribution of the fluorescent brightness $F(z)$. This is proportional to the product of irradiance and tracer concentration, so that in general

$$F(z) = I_0 c(z) \cdot \exp\left(-\epsilon \int_0^z c(z')\,\mathrm{d}z'\right). \tag{7.14}$$

For the sake of simplicity, all constant factors are summarized in I_0. The task therefore consists in extracting the tracer concentration profile according to the above equation. One possible attempt could be to solve eq. (7.14) iteratively by adjusting an estimated profile $c_{\text{est}}(z)$ which minimizes the difference $F_{\text{observed}}(z) - F(z; c_{\text{est}})$. At $z = 0$, the fluorescent brightness is simply given as $F(z = 0) = I_0 \cdot c_s$, suggesting an optimization routine that follows the integration. The pre-factor unfortunately is not known to good precision, as it depends on the exact local irradiance, absorption cross section of acetone, quantum efficiency, and the optical characteristics of the camera system. A global, parallel optimization approach, on the other hand, would require a suitable scheme by which to adjust the estimated profile $c_{\text{est}}(z)$ at each z during iteration while retaining realistic smoothness and good converging properties. To come along these numerical, algorithmic difficulties, I decided to adopt a simpler, yet suitable approach, which is explained in the following section.

7.2.3 Implementation and stability of fit approach

The concentration was a-priori parametrized by an exponential function as

$$c(z) = c_b + (c_s - c_b) \exp\left(-\frac{z}{z^*}\right), \tag{7.15}$$

Such an exponential profile corresponds to the prediction by the surface renewal model (see sec. 2.4) for free surface boundary conditions, but here it is used as a generic functional description for the vertical tracer distribution close to the water surface without explicitly intending the conceptual validity of the surface renewal model. It contains all relevant parameters, i.e. two concentration values (c_b and c_s) and a scale parameter (z^*), to characterize the tracer profile which can independently of any model assumed to gradually decay from its surface value towards the well-mixed water bulk (in an invasion experiment).

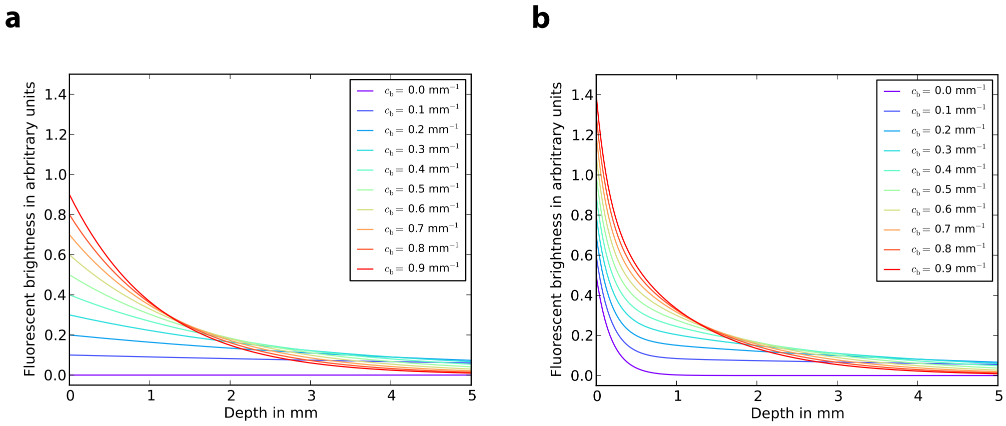

Figure 7.5: Fluorescence model profile for a range of realistic values of $\tilde{c}_b$ for a trivial homogeneous tracer distribution (a) and a profile with a boundary layer width of $z^* = 200\,\mu\mathrm{m}$ (b).

With eq. (7.15) and eq. (7.14), an explicit form of the fluorescence profile can be given in terms of the model parameters,

$$F(z) = I_0 \left[c_b + (c_s - c_b) \exp\left(-\frac{z}{z^*}\right) \right] \cdot \exp\left[-\epsilon c_b z - \epsilon (c_s - c_b) z^* \left(1 - \exp\left(-\frac{z}{z^*}\right)\right) \right]. \tag{7.16}$$

Observing that I_0 is anyhow a free parameter that may contain an additional factor of ϵ, the concentration terms can be redefined as $\tilde{c}_b \equiv \epsilon c_b$ and $\tilde{c}_s \equiv \epsilon c_s$. This provides an explicit expression with four free parameters which can be used with any standard least-square algorithm.

The fluorescence model profile is shown in Fig. 7.5 for different realistic values of $\tilde{c}_b$ for a homogeneous tracer distribution (a) and a profile with a boundary layer width of $z^* = 200\,\mu\mathrm{m}$ (b).

It should be observed, that eq. (7.16) contains two scale parameters, i.e. z^* and $(\epsilon c_b)^{-1}$, related to the extent of the diffusive sublayer and the degree of light absorption, respectively. If both scales coincide, i.e. $(\epsilon c_b)^{-1} \approx z^*$, the two parameters are essentially degenerated and the least-square fit is expected to become instable. For an extinction coefficient of acetone of $\epsilon \approx 1.52\,\mathrm{L/(mol\,mm)}$ (see sec. 3.1.4) and a rather thick boundary layer of $z^* = 1\,\mathrm{mm}$ occurring at the lowest wind speeds, the above condition would require a concentration of $c_b \approx 0.5\,\mathrm{mol/L}$. This is equivalent to a total amount of 600 g of acetone in the water which was never reached in any experiment.

When an invasion experiment approaches an equilibrium state in the absence of influx and leakage, the flux across the air-water interface ceases and $(c_s - c_b) \to 0$. In this case, eq. (7.16) reduces to

$$F(z) = I_0 c_b \exp(-\epsilon c_b z), \tag{7.17}$$

and becomes insensitive to the fit parameter c_s. To guarantee anyhow sensible results, the fit is pre-conditioned by the value c_b obtained from fitting eq. (7.17) to the bulk portion ($z \ll z^*$) of the fluorescence profile. Indeed, for $z/z^* \gg 1$, again eq. (7.16) reduces to eq. (7.17), as can be easily checked.

The complete fit routine therefore consists of two consecutive steps. First, the bulk tracer concentration c_b is obtained by fitting eq. (7.17) to the brightness profile in the range of $4\,\mathrm{mm} < z < 8\,\mathrm{mm}$ corresponding to the bulk portion of the image. In a second step, c_b is used as a fixed value and the full function eq. (7.16) with only three free parameters is fitted to the entire brightness profile up to the surface. This proved to give stable results even in near-equilibrium conditions.

7.2.4 Absolute concentrations

For the water-sided profiles, conversion into physical values with unit mol/L was straight forward. Indeed, the model-based fit approach in the previous section already includes a description of the Lambert-Beer absorption. Physical concentrations were obtained by dividing the fit parameters (ϵc_b) and (ϵc_s) by the extinction coefficient for acetone, $\epsilon = 1.52\,\mathrm{L/(mol\,mm)}$ (see sec. 3.1.4).

7.2.5 Systematic error due to limited optical resolution

As explained in sec. 2.4.1, the water-sided diffusive sublayer is expected to become as thin as 80 µm-100 µm for the highest wind speeds in the wind-wave tank used in this work. On the other hand, the effective resolution of the camera system is limited by optical aberration. To quantify the impact of this limitation on the experimental results and to possibly correct for them, I estimated the systematic error induced in the profile parameters due to the optical imperfections of the system. In this context it is useful to observe that the total reflection angle for a light ray at the phase boundary water-air is about 49°. For a camera observing the water surface from underneath at a angle of $-10°$ from the horizontal plane, water surface slopes of at least $\tan(39°) = 0.8$ would be required for the surface to become transparent. Such values are never reached in any wind condition as is evident from the wave slope measurements presented in sec. 5.3. In other words, the water surface always acts as a perfect mirror when observed by the camera.

Secondly, it should be noted that optical aberration amounts to a smoothing of the image, i.e. a spatial convolution. This has the mathematical property of conserving image brightness. For a narrow, pronounced brightness profile such as in Fig. 7.5 (b), optical aberration would therefore lead to a mere spatial redistribution of the brightness. Without correction for this effect, the maximum value at the surface would however be systematically underestimated. I quantified this by creating a synthetic brightness profile according to eq. (7.16), reflecting it at $z = 0$, and applying a spatial convolution with a Gaussian function of varying FWHM. The result is shown for exemplary concentration parameters in Fig. 7.6 (a). For unrealistically

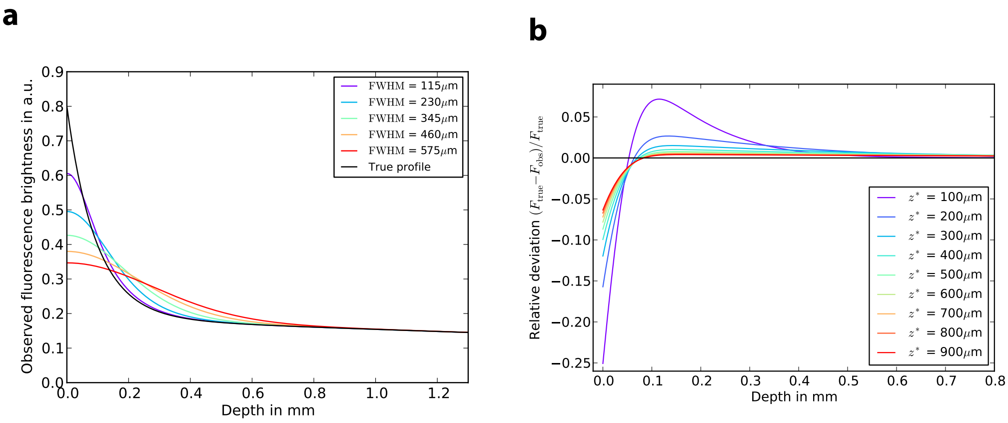

Figure 7.6: (a) Simulated fluorescence profiles for $\epsilon c_\mathrm{b} = 0.2\,\mathrm{mm}^{-1}$, $\epsilon c_\mathrm{s} = 0.8\,\mathrm{mm}^{-1}$, and $z^* = 0.1$ mm for different degrees of optical smoothing. (b) Relative systematic deviation of the observed fluorescence profile for a Gaussian smoothing function with a FWHM of 120 µm for different boundary thickness z^*. *No* correction for optical smoothing is applied.

strong optical smoothing, the observed fluorescence profile is significantly altered with respect to the ground truth. For reasonable value for the FWHM of the Gaussian smoothing kernel, the surface appears systematically darker but the overall brightness profile is still preserved.

Optical aberration affects the profile stronger the thinner the boundary layer is. To obtain a quantitative impression of this dependence, I created synthetic observed fluorescence profiles for a fixed FWHM of 120 µm and different values of the boundary layer scale z^*. The relative deviation from the ground truth profile is depicted in Fig. 7.6 (b). For the thinnest expected boundary layers (see sec. 2.4.1), the water surface might appear up to 25 % darker due to optical smoothing if no correction is applied.

7.2.6 Correction for optical sharpness

The brightness conserving properties and the total reflection at the water surface suggest a simple method to compensate for the systematic underestimation of the surface brightness due to optical aberration. During an iteration step of the least-square fit algorithm, after calculating the model profile for a set of test parameters, (c_s, z^*, I_0), but before passing the result to the optimization routine, the model profile is reflected around $z = 0$ and convolved with a Gaussian kernel of fixed FWHM. In this way, optical aberration is explicitly taken into account and the systematic error in the retrieved concentration profile parameters is minimized. The smoothing scale was estimated from target images and manually set rather than adding an additional free parameter to the algorithm. Depending on how correct the smoothing scale is chosen, the fit parameters retain a certain degree of systematic deviation. This is illustrated in Fig. 7.7, where concentration profiles with different values of z^* and

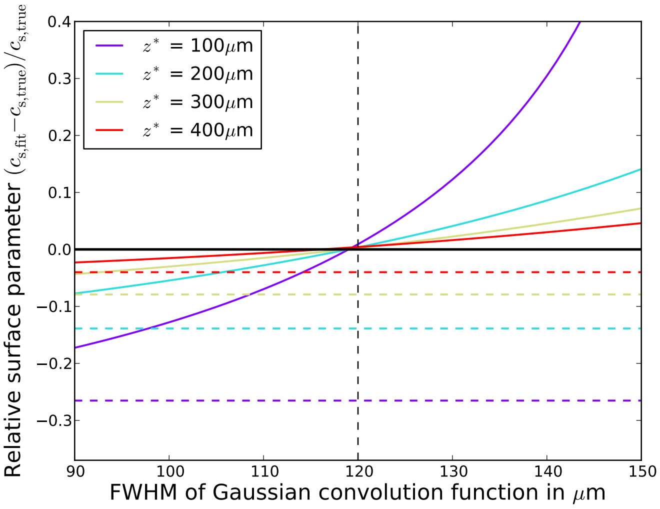

Figure 7.7
Relative deviation of the surface concentration ϵc_{s} retrieved from a synthetic profile for different values of z^*. The dashed lines correspond to the systematic error when no correction for the optical aberration is done. The solid lines show the systematic error if the fit function is smoothened with a Gaussian kernel of a certain size prior to the least-square optimization.

smoothened with a FWHM of 120 µm were used as ground truth. The dashed lines correspond to the relative systematic error in the retrieved surface concentration c_{s} when no correction for the optical aberration is done. The solid lines shows the relative systematic error with optical correction as a function of applied kernel size. Evidently, for an adequately chosen FWHM value, the systematic error in c_{s} can efficiently be reduced. A rather conservative choice of the smoothing scale is preferable, however, as for too large values, c_{s} may easily be overestimated greatly. Based on tests with recorded images, I have chosen a FWHM of 100 µm. According to this analysis, measured water-sided surface concentrations are estimated to be precise to about 10 % or better.

7.3 Eddy statistics

The surface detection algorithm explained in sec. 7.2.1 can be modified to yield useful information about the eddy distribution underneath the water surface. The physical reasoning is that streaks in the fluorescent image correspond to connected regions of locally enhanced tracer concentrations. These are originally detached from the surface and carried downwards into the bulk. Statistically, the distribution of streaks should therefore provide a good estimate in the occurrence of turbulent eddies.

Practically, the same steps outlined in sec. 7.2.1 to find local maxima and to reduce erroneous detections were performed resulting in binary objects which represent the streaks. This was shown in Fig. 7.4 (a). For all objects, their upper edge was detected with a gradient mask and for all edge pixels, their vertical position relative to the water surface above was calculated. This could be performed on a series of images yielding a distribution of vertical distance of streaks from the interface. Following the above argumentation, this procedure allowed to estimate the minimal approach distance of turbulent eddies to the water surface under different forcing conditions. The results were particularly useful for interpreting the mechanisms leading to a reduction of gas exchange in the presence of surfactants (see sec. 8.5).

7.4 Mass balance method

A commonly used approach to determine transfer resistances, or equivalently transfer velocities, is to monitor the well mixed bulk tracer concentration in a wind-wave tank (e.g. *Krall*, 2013; *Nielsen*, 2004). As explained in sec. 2.3, the so-determined resistances are of integral character and provide no direct insight in the local, near-surface turbulence. Nonetheless, this approach provides a straight forward complementary method that has also been used in this work. Here, I shortly outline the formulae needed for the data analysis in this work.

The wind-wave tank is thought of as an air and a water compartment of respective volumes V_{water} and V_{air}, separated by an interface of area A. In closed conditions, i.e. neglecting leakage and with acetone injection turned off, water and air-sided concentrations are coupled through two differential equations. In matrix form they read

$$\begin{pmatrix} \dot{c}_{\mathrm{air}} \\ \dot{c}_{\mathrm{water}} \end{pmatrix} = A \cdot \begin{pmatrix} -\frac{k}{V_{\mathrm{air}}} & \frac{k}{\alpha_{\mathrm{H}} V_{\mathrm{air}}} \\ \frac{k}{V_{\mathrm{water}}} & -\frac{k}{\alpha_{\mathrm{H}} V_{\mathrm{water}}} \end{pmatrix} \begin{pmatrix} c_{\mathrm{air}} \\ c_{\mathrm{water}} \end{pmatrix} \tag{7.18}$$

This can be solved by computing the eigenvalues of the matrix and posing the initial conditions $c_{\mathrm{air}}(t=0) = c_{\mathrm{air},0}$ and $c_{\mathrm{water}}(t=0) = c_{\mathrm{water},0}$, yielding

$$c_{\mathrm{air}}(t) = \frac{c_{\mathrm{water},0} + V_{\mathrm{air}}/V_{\mathrm{water}}\, c_{\mathrm{air},0}}{\alpha_{\mathrm{H}} + V_{\mathrm{air}}/V_{\mathrm{water}}} + \frac{\alpha_{\mathrm{H}} c_{\mathrm{air},0} - c_{\mathrm{water},0}}{\alpha_{\mathrm{H}} + V_{\mathrm{air}}/V_{\mathrm{water}}} \exp\left[-kA\left(\frac{1}{V_{\mathrm{air}}} + \frac{1}{\alpha_{\mathrm{H}} V_{\mathrm{water}}}\right) t\right] \tag{7.19}$$

$$\begin{aligned} c_{\mathrm{water}}(t) = & \frac{c_{\mathrm{water},0} + V_{\mathrm{air}}/V_{\mathrm{water}}\, c_{\mathrm{air},0}}{1 + V_{\mathrm{air}}/(V_{\mathrm{water}}\alpha_{\mathrm{H}})} \\ & - \frac{V_{\mathrm{air}}}{V_{\mathrm{water}}} \cdot \frac{\alpha_{\mathrm{H}} c_{\mathrm{air},0} - c_{\mathrm{water},0}}{\alpha_{\mathrm{H}} + V_{\mathrm{air}}/V_{\mathrm{water}}} \exp\left[-kA\left(\frac{1}{V_{\mathrm{air}}} + \frac{1}{\alpha_{\mathrm{H}} V_{\mathrm{water}}}\right) t\right]. \end{aligned} \tag{7.20}$$

From an exponential fit to the decay, the integral transfer velocity $k = R^{-1}$ can thus be easily determined. The parameters V_{water}, V_{air}, A, and α_{H} are given in sec. 4.1.1 and sec. 3.1.4.

8

Results

8.1 Air-sided profiles

Air-sided profiles were obtained from quotients of data images and reference images, consequently yielding normalized concentrations $^{c(z)}/_{c_\mathrm{b}}$ denoted as $\bar{c}^+$. The visualization concept was described in sec. 3.1.6 and the implementation in the data processing routines in sec. 7.1.1. In this section, I summarize aspects that may be deduced from the concentration profiles alone, i.e. without regarding the simultaneously observed water side. For nomenclature, I refer to chap. 2.

In sec. 2.4.1, I explained how concentration profiles can be calculated based on a parametrization of the turbulent diffusivity $K_\mathrm{diff}(z)$ which interpolates between pure diffusion close to the boundary and the linear dependence on z leading to the logarithmic shape (see sec. 2.2.1). A basic assumption of this approach is the conceptual equivalence of momentum and mass transport through the turbulent boundary. To my best knowledge, profiles of passive scalars have so far not been observed experimentally down to scales of the diffusive sublayer.

8.1.1 Comparison with wind profiles

If momentum and mass transfer are assumed conceptually equivalent, a diffusive sublayer should exist below $z^+ \approx 11 (\equiv {}^{z_{11} u_*}/_{\nu})$ and a logarithmic sublayer for about $(z_{11} < z < 0.15\delta)$, where δ is the overall thickness of the air-sided boundary layer.

To make the analogy clear, I restate the relevant equations from sec. 2.2. According to eq. (8.1), the wind profile derived from Reichardt's turbulent viscosity model is

$$\bar{u}(z^+) - u_{\text{plate}} = \frac{\tau_s}{\rho u_*} \underbrace{\int_0^{z^+} \frac{\nu}{\nu + K_{\text{turb}}(z^+)} dz^+}_{\mathcal{R}(z^+)}, \tag{8.1}$$

where I have included explicitly a term to allow for a bottom plate moving relative to the airflow. In terms of momentum transport, its value determines the strength of the momentum sink and for $u_{\text{plate}} = 0$, the wind profile decays to zero in the laboratory frame. If on the other hand, the plate moves with exactly the bulk wind speed U_0, no momentum is dissipated and $\bar{u}(z) = U_0$, i.e. the profile is flat.

In analogy, for a non-vanishing surface concentration one has according to eq. (2.33),

$$c(z) - c_s = \frac{j_s \nu}{\mathrm{D} u_*} \cdot \underbrace{\int_0^{z^+} \frac{\mathrm{D}}{\mathrm{D} + K_{\text{diff}}(z^+)} dz^+}_{\mathcal{D}(z^+)}. \tag{8.2}$$

The term $\mathcal{D}(z^+)$ contains all the scaling properties of the profile and can be calculated numerically by integration.

To compare profiles for different wind speeds and to retrieve the transfer resistance, knowledge of the surface concentration is necessary. Different from the velocity of the moving bottom plate in the case of wind profiles, it is not easily measurable as separate experimental parameter because it depends on the unknown relative flux in the underlying water. Therefore, c_s has to be determined from the profiles themselves.

To investigate the scaling properties and self-similarity of the concentration profiles, I exploited their presumed characteristic shape within the diffusive and logarithmic sublayer, respectively. The exact scaling procedures are explained in the following two sections. Equation (8.2) is used in sec. 8.1.4 to fit full Deacon profiles. I present the deduced transfer resistances in sec. 8.6.

8.1.2 Profile scaling - diffusive sublayer

Very close to the surface, i.e. for $z \to 0$, the integrand in eq. (8.2) is 1 and thus $\mathcal{D}(z^+) \approx z^+$. In this regime, eq. (8.7) reduces to a linear expression of the form

$$\bar{c}^+(z) = A \cdot z + B. \tag{8.3}$$

The two parameters A and B can be used to scale and non-dimensionalize the profiles as

$$c_{\text{lin}}(z/\delta) \equiv \frac{\bar{c}^+(z/\delta) - B}{A}. \tag{8.4}$$

By this definition, $c_{\text{lin}}(0) = 0$.

Figure 8.1 shows measured non-dimensional concentration profiles $c_{\text{lin}}(z/\delta)$ for

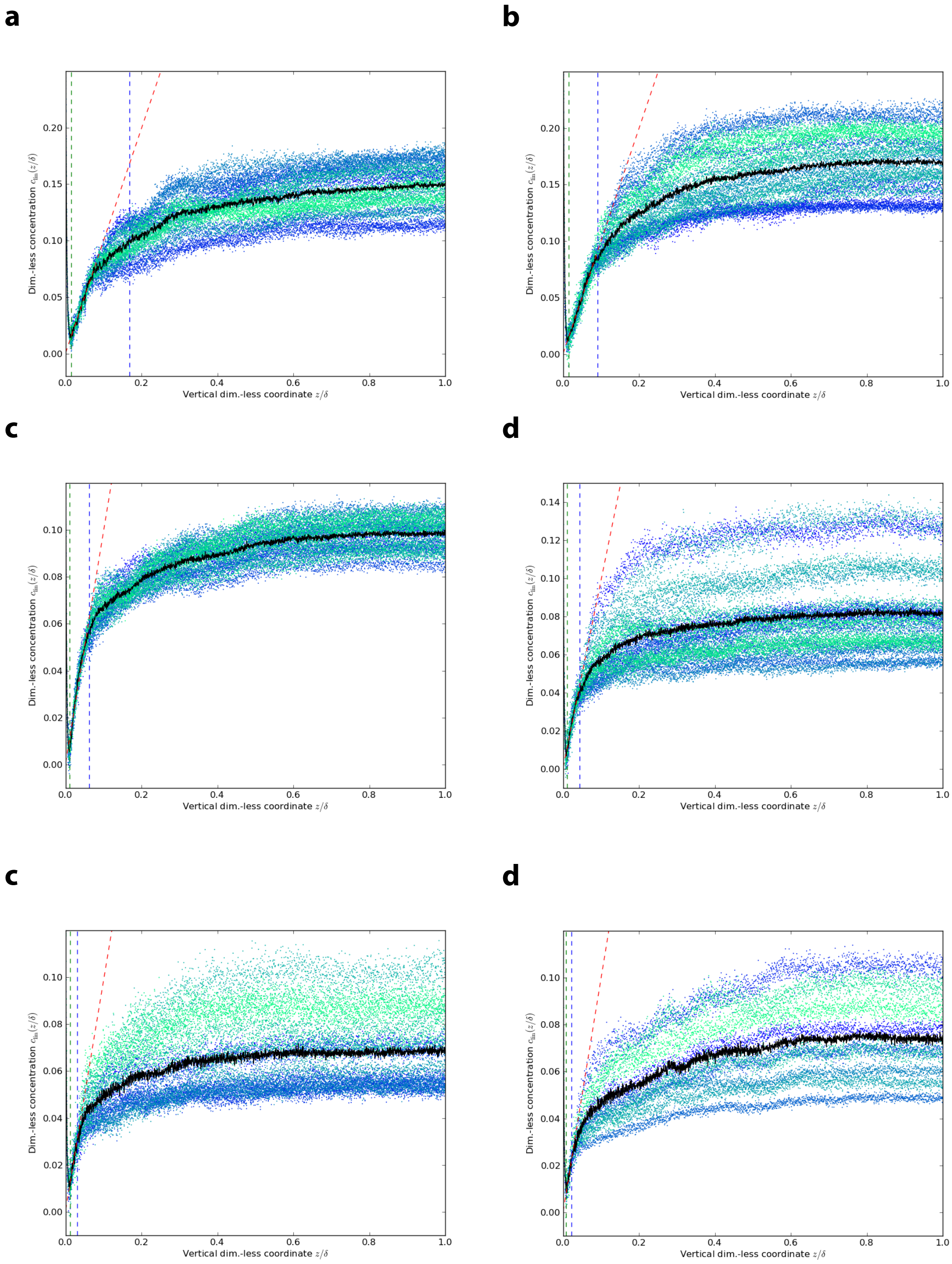

Figure 8.1: Air-sided concentration profiles $c^+(z) = {}^{(c(z)-c_s)}/_{c_b}$ scaled by a tangent fit to the diffusive sublayer, i.e. $c_{\text{lin}}(z/\delta) = \frac{\bar{c}^+(z/\delta)-B}{A}$. The surface gradient is shown as a red dashed line. The green dashed line indicates the coordinate of minimal measured concentration and the blue one $z^+ = 11$. Turbine frequencies are (a)-(f): 5, 8, 11, 15, 18, 21 Hz.

different wind speeds. The blue shades indicate profiles averaged over 10 s and the black curve shows the average over a series of 3 min. The surface gradient was fitted for $z^+ < 11$ and is shown as a red dashed line. The green dashed line indicates the coordinate of minimal measured concentration and the blue one the theoretical transition from diffusive to turbulent regime ($z^+ = 11$).

It should be noted that for the lowest wind speed (a), the measured profile levels off more quickly than at higher wind speeds. Specifically, the mean profile value at $z^+ = 11$ is less than extrapolated by the gradient. This is to be ascribed to the non-developed turbulent flow under these conditions. Indeed, it is easily checked that $z_{11} > 0.15\delta$ so that no logarithmic sublayer is expected to exist.

Figure 8.2 shows the same data and fitted gradients, however in logarithmically scaled vertical coordinate z. In this representation, the diffusive ($z < z_{11}$) and the logarithmic sublayer ($z_{11} < z < 0.15\delta$) are visible. Below a certain minimal distance, measured concentrations are biased by the overlaying recorded brightness originating from the water side (see sec. 4.2). I will comment on this in sec. 8.1.7.

Matching profiles based on their surface gradient has two major drawbacks. First, the linear approximation is valid only asymptotically for $z \rightarrow 0$ and the numerical fit result of eq. (8.3) will conceptually depend on the choice of the upper boundary (here z_{11}). Second, the diffusive sublayer becomes thinner for higher winds so that effectively ever fewer data points are available causing the approach to be less robust.

8.1.3 Profile scaling - logarithmic sublayer

Analogously to wind profiles (see sec. 2.2.1), also concentration profiles within the turbulent boundary layer are expected to have a distinct logarithmic shape in the sublayer for ($z_{11} < z < 0.15\delta$), i.e.

$$\bar{c}^+(z) = A\log(z) + B. \tag{8.5}$$

Since it is much wider than the diffusive sublayer and thus contains more data points, this regime should be well-suited for scaling measured profiles.

The above expression can be re-ordered to yield

$$c_{\log}(z/\delta) \equiv \frac{\bar{c}^+(z/\delta) - B}{A}. \tag{8.6}$$

By determining A and B from a logarithmic fit for $z_{11} < z < 0.15\delta$ and scaling the vertical coordinate by the boundary layer thickness δ determined from wind profiles (see sec. 5.1), the profiles $c_{\log}(z/\delta)$ should become self-similar.

This is shown in Fig. 8.3 for six wind speeds. The blue shades indicate profiles averaged over 10 s and the black curve shows the average over a series of 3 min. The data are taken from the initial stage of an invasion experiment since at later times, the water-sided brightness overlays the signal in the diffusive sublayer (see sec. 8.1.7). The height $z/\delta = 1$ corresponds to the beginning of the well-mixed bulk region.

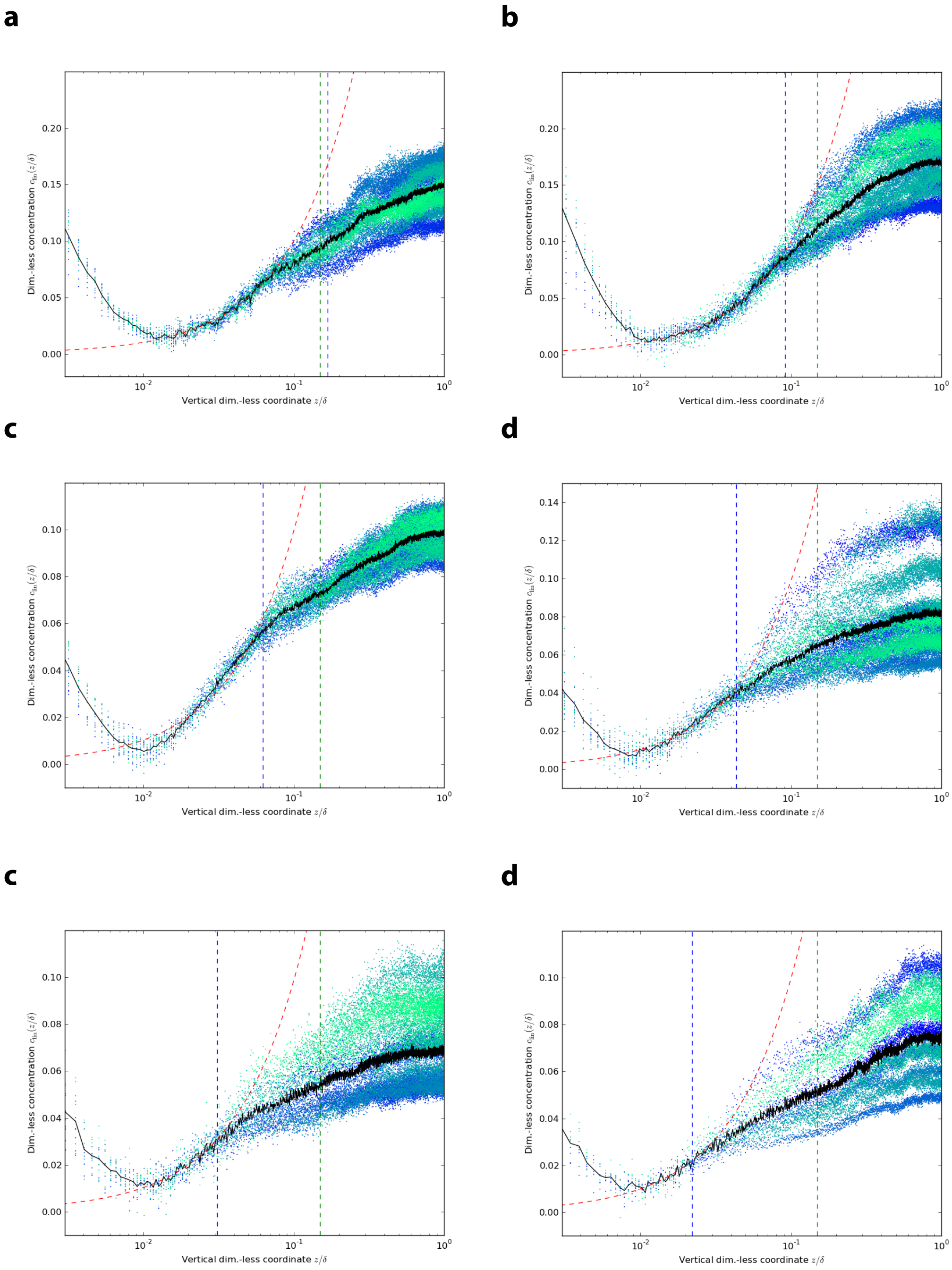

Figure 8.2: The figures depict the same data as in Fig. 8.1, with the vertical coordinate scaled logarithmically. The surface gradient is shown as a red dashed line. The blue dashed line indicates $z^+ = 11$ and the green one $z = 0.15\delta$. Turbine frequencies are (a)-(f): 5, 8, 11, 15, 18, 21 Hz.

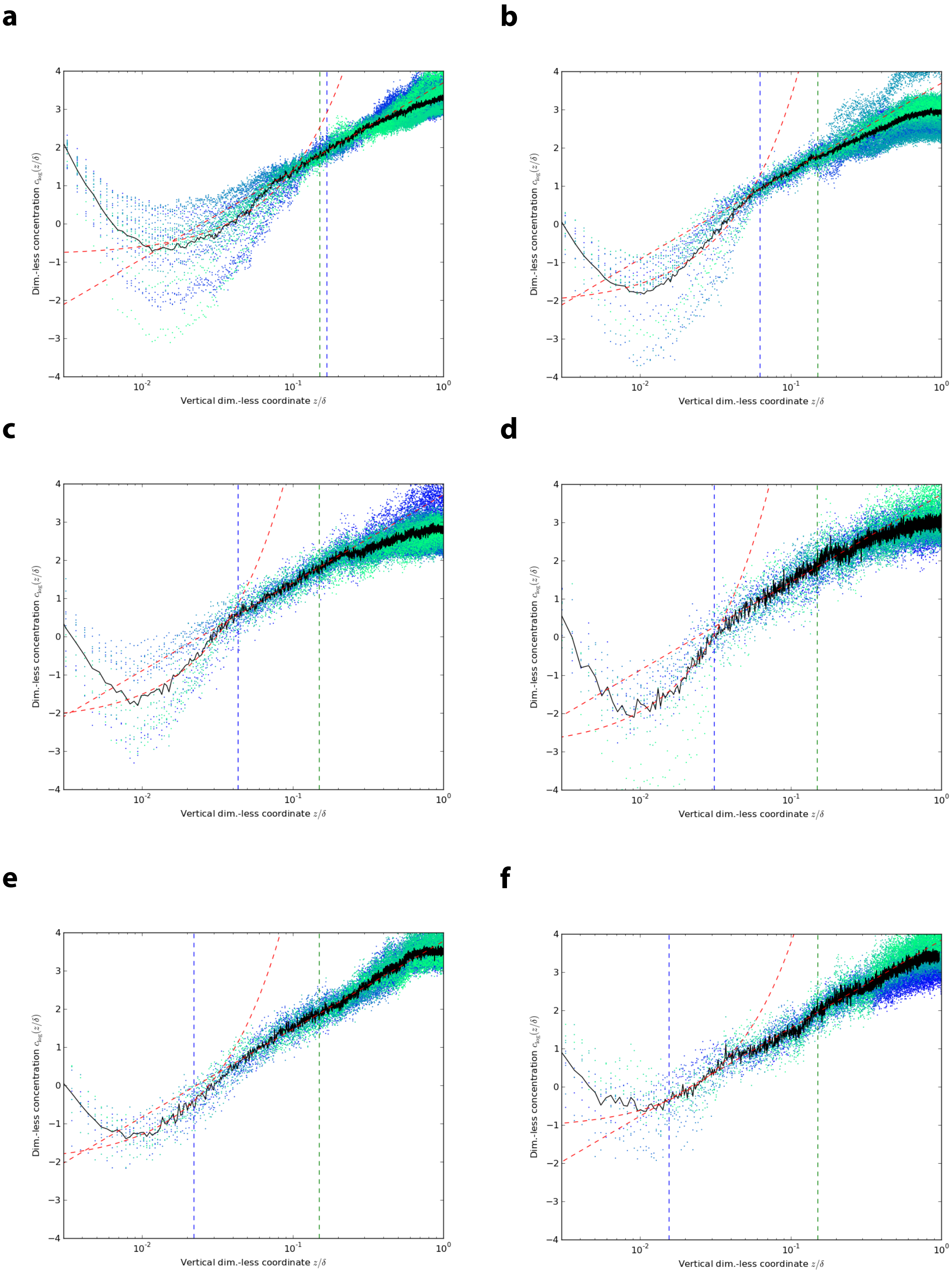

Figure 8.3: Air-sided concentration profiles scaled by a fit to the logarithmic sublayer. The logarithmic portion is shown as a straight red dashed line. Additionally the surface gradient of the average profile (black) is shown as curved red dashed line. The blue dashed line indicates $z^+ = 11$ and the blue one $z = 0.15\delta$. Turbine frequencies are (a)-(f): 5, 8, 11, 15, 18, 21 Hz.

The two dashed red lines indicate the logarithmic and the linear regime, respectively. For (a)-(e), their point of intersection matches well the expected scale of transition z_{ll}, indicated by the blue dashed line. This demonstrates, that profiles resulting from scalar mass transport show analogous scaling behavior as wind profiles resulting from momentum transport. The green dashed line represents $z = 0.15\delta$, i.e. the upper boundary of the logarithmic sublayer. Indeed, roughly above, the averaged profiles start to become more shallow towards the upper edge of the turbulent boundary layer at $z = \delta$, especially for low and intermediate wind speeds. In (e) and (f), the logarithmic sublayer appears to extend beyond $z = 0.15\delta$. For these higher wind speeds, the diffusive sublayer appears less pronounced or almost inexistent in (f). This might be due to the overlaying water-sided brightness (see sec. 8.1.7), but could also indicate an alternation of the flow profile above the wavy surface. I will discuss this in sec. 9.1.

8.1.4 Matching Deacon model profiles

Under the assumption of stationarity, the mass flux j_s can be expressed in terms of transfer resistance, i.e. $j_\mathrm{s} = R_\mathrm{a}^{-1}(c_\mathrm{b} - c_\mathrm{s})$. For the normalized concentrations $\bar{c}^+ = {}^{c}/_{c_\mathrm{b}}$ extracted from the quotient images (see sec. 7.1.1), eq. (8.2) can then be stated in the compact form

$$\bar{c}^+ = \frac{(c_\mathrm{b} - c_\mathrm{s})\nu}{c_\mathrm{b} u_* \mathrm{D} R_\mathrm{a}} \cdot \mathcal{D}(z^+) + \frac{c_\mathrm{s}}{c_\mathrm{b}}. \tag{8.7}$$

It should be noted that the surface concentration influences both offset and overall slope of the normalized concentration profiles. The above expression can be used to match measured profiles with Deacon's model and to retrieve transfer resistances therefrom.

In practice, I used the following rather technical procedure. According to eq. (8.7), two parameters γ_1 and γ_2 are necessary such that

$$\bar{c}^+ = \gamma_1 \mathcal{D}(z^+) + \gamma_2. \tag{8.8}$$

The function $\mathcal{D}(z^+)$ is evaluated numerically at those heights corresponding to the data points $z = {}^{zu_*}/_{\nu}$ and a standard least-square algorithm is used to fit this to the data and obtain γ_1 and γ_2. According to the coefficients in eq. (8.7), the air-sided transfer resistance R_a can be calculated as

$$R_\mathrm{a} = \frac{1 - \gamma_2}{\mathrm{D} u_* \gamma_1} \nu. \tag{8.9}$$

I present the transfer resistances determined by this approach in sec. 8.6. It should be noted that by using information from the logarithmic sublayer, the results are less susceptible to bias due to water-sided fluorescence. It should also be observed that resistances obtained by fitting Deacon's model to the data do not entirely depend on the assumption of diffusive transport at the surface, as the diffusive sublayer

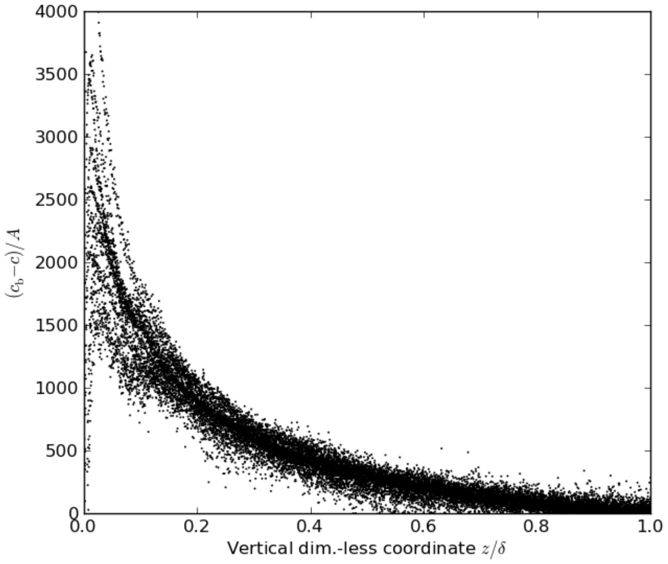

Figure 8.4
Scaled air-sided concentration profiles $(c_\mathrm{b}-c)/\Omega$ as a function of dimensionless height z/δ. The parameters were obtained by a fit to the outer layer, $\bar{c}(z) = \Omega\,(z-\delta)^2 + c_\mathrm{b}$. Profiles match reasonably well for $z > 0.1\delta$, asserting the self-similarity in the outer layer.

contributes only partially to the air-sided resistance. The slope, containing the mass flux as factor, is chosen such that model and data profile match up to the upper edge of the logarithmic sublayer. In this sense, this approach is conceptually more robust than fitting the surface gradient only, as explained in sec. 8.1.1. Since $j = R^{-1}(c_\mathrm{b} - c_\mathrm{s})$, the resistance does depend, however, on the extrapolated surface concentration.

8.1.5 Scaling of the outer layer (wake)

For wind profiles, the logarithmic sublayer extends to about 15 % of the total turbulent boundary layer thickness, i.e. up to $z < 0.15\delta$ (see sec. 2.2). Beyond, no *ab initio* model description is available, but empirically, the outer layer was found to be self-similar. The obvious question arises, whether concentration profiles associated with mass transport show an equivalent behavior.

For the determination of the friction velocity u_* in sec. 5.1, I used a quadratic function as simplest self-similar expression. In analogy to eq. (5.1), I fitted the following function to concentration profiles for all wind speeds used in this work,

$$\bar{c}(z) = \Omega\,(z-\delta)^2 + c_\mathrm{b} \tag{8.10}$$

and used the retrieved parameters to rescale the profiles. Figure 8.4 depicts the scaled concentration $(c_\mathrm{b}-c)/\Omega$ as a function of dimensionless coordinate z/δ. The plot suggests self-similarity in the wake-region ($z/\delta > 0.15$). Closer to the surface, some discrepancies are visible. These are partially to attributed to the non-developed turbulent flow for lower wind speeds and partially to the profiles at higher wind speeds which appear flatter than expected from smooth wall flow.

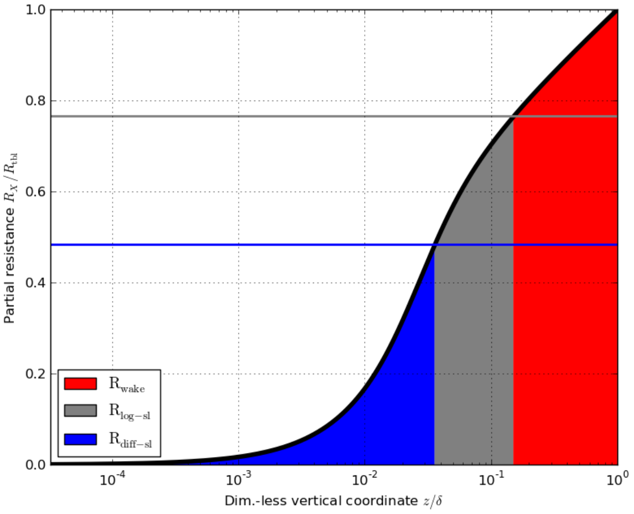

Figure 8.5
Sketch to illustrate the partitioning of resistance within the air-sided turbulent boundary layer. The black line is a theoretical Deacon profile for $u_* = 10$ cm/s. The three sublayers are indicated by the color filling and the horizontal lines show the resistance up the corresponding height above the water surface.

Summarizing, the analysis based on experimental results presented in the preceding sections demonstrates that indeed air-sided scalar transport may be treated in close analogy to momentum transport.

8.1.6 Distribution of resistance within the air-sided turbulent boundary layer

In sec. 2.3, I underlined the point of view that concentration profiles essentially describe the vertical distribution of transfer resistance. In this light, an interesting question is to analyze the contribution of the three sublayers to the total resistance of the air-sided boundary layer.

A concentration profile varies from c_s at the surface to the value c_b which is reached at $z = \delta$. Normalizing with these two parameters yields a function defined on the unity interval which is equivalent to the relative resistance distribution (see eq. (2.27) in sec. 2.3).

$$\frac{R(z)}{R_{\mathrm{tot}}} = \frac{c(z)}{c_b - c_s} \quad \in [0, 1] \tag{8.11}$$

In Fig. 8.5, this is shown as an example based on the Deacon profile for acetone, a friction velocity u_* of 10 cm/s and a boundary thickness δ of 40 mm. For simplicity and the lack of any theoretical description of the outer layer, I used a logarithmic shape also for $z > 0.15\delta$.

To each layer, a partial resistance can be attributed by the following definitions:

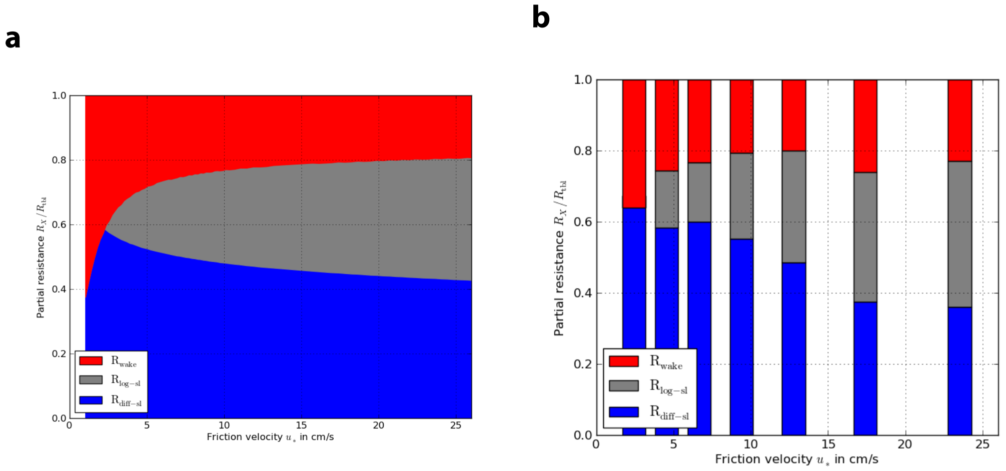

Figure 8.6: (a) Theoretical partitioning of resistances within the air-sided turbulent boundary layer for a Deacon profile as depicted in Fig. 8.5 and extending the logarithmic form in to outer layer. (b) Resistance partitioning calculated from logarithmically scaled profile depicted in Fig. 8.3.

$$R_{\text{diff.}} \equiv \frac{R(z_{11})}{R_{\text{tot}}} = \frac{c(z_{11})}{c_b - c_s} \tag{8.12}$$

$$R_{\text{log.}} \equiv \frac{R(z = 0.15\delta) - R(z = z_{11})}{R_{\text{tot}}} = \frac{c(z = 0.15\delta) - c(z_{11})}{c_b - c_s} \tag{8.13}$$

$$R_{\text{outer}} \equiv \frac{R(z = \delta) - R(z = 0.15\delta)}{R_{\text{tot}}} = \frac{c(z = \delta) - c(z = 0.15\delta)}{c_b - c_s} \tag{8.14}$$

This is indicated in Fig. 8.5 by the three different colors.

It is well-known from boundary layer theory that for increasing wind speed the logarithmic sublayer expands downwards causing the diffusive sublayer to become slimmer (e.g. *Schlichting*, 2000). Also, the overall thickness of the turbulent boundary layer δ generally depends on wind speed, fetch and roughness. Indeed, a slight increase of δ has been observed from wind profile measurements with the onset of waves (see sec. 5.1).

To determine the relative resistance contributions defined in eq. (8.12), I used the logarithmically scaled profiles, such as shown in Fig. 8.3. The upper value c_b at $z = \delta$ could readily be taken from the data and the surface concentration c_s was extrapolated from the linear fit shown as curved dashed red lines in the plots. The values $c(z_{11})$ and $c(0.15\delta)$ were taken at the corresponding wind speed dependent coordinates.

The result is shown in Fig. 8.6 (a) together with the theoretical values obtained from Deacon's model profile shown in Fig. 8.5. The agreement is quite satisfying and confirms the theoretical expectation that for growing wind speed, i.e. thickening

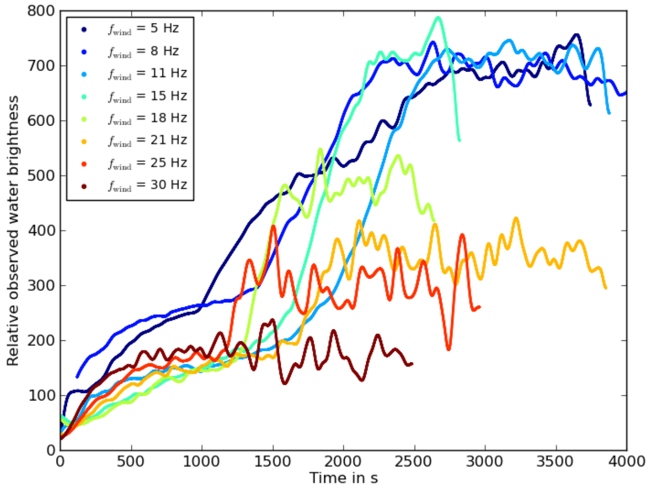

Figure 8.7
Brightness in the region underneath the detected surface coordinates in the air-sided images, normalized to the bulk brightness. For lower wind speeds, the brightness ratio approaches a value between 700 and 800, i.e. approximately the solubility of acetone.

logarithmic sublayer, the diffusive contribution to the air-sided resistance plays an inferior role. Because δ also grows with fetch, under field conditions, the diffusive impact on the air-sided transport should often be expected to become negligible.

In a laboratory experiment, the size of the turbulent boundary layer is limited by the geometry of the wind-wave facility and in particular by the height of the air compartment.

8.1.7 Bias by water-sided brightness

Due to the high solubility of acetone, its concentration in the aqueous phase, and consequently also the fluorescent brightness projected onto the camera sensor by optical refraction at the surface, is up to 800 times higher. This overlays the air-sided signal and thus induces a bias on the measured surface-near concentration values. Additionally, optical aberration of the camera objective causes some blurring of the high brightness contrast at the air-water interface. For a more detailed description of the geometric properties, I refer to sec. 4.2 where I have analyzed the dependence of this optical effect on parameters such as water surface angle and laser sheet width.

During an invasion experiment, acetone continuously accumulates in the aqueous phase resulting in a rise in concentration which causes the water-sided fluorescence to become brighter. A typical raw image can be seen in Fig. 7.1 of sec. 4.2. To obtain a qualitative impression of the time evolution of the water-sided brightness observed by the air-sided camera, I determined the maximum brightness in the region underneath the detected surface coordinates and normalized to the air-sided bulk brightness. The result is shown in Fig. 8.7. For lower wind speeds, the brightness ratio approaches a value between 700 and 800, i.e. approximately the solubility of acetone. At higher wind speeds, values are systematically lower. This might to some extent be associated with optical distortion of the light originating from the water. It

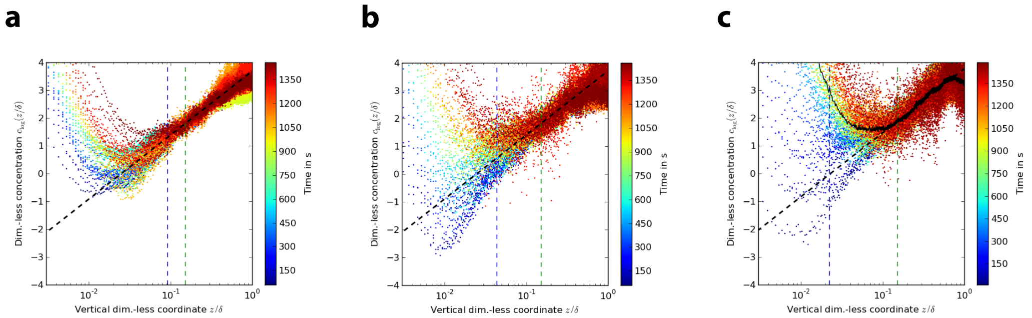

Figure 8.8: Air-sided concentration profiles, scaled according by their logarithmic sublayer as explained in sec. 8.1.3, for different instances during the course of an invasion experiment. Time is color-coded, in seconds. Each profile is an average over 50 images, i.e. 25 s. Blue and green dashed lines depict $z^+ = 11$ and $z = 0.15\delta$, respectively.

seems reasonable that this spreads out the observed spot on the surface resulting in a less pronounced signal in the projected air-sided image. On the other hand, also water-sided surface concentrations were generally observed to be much lower under more energetic conditions (see sec. 8.3.3) which would explain the dimmer signal.

In Fig. 8.8, air-sided profiles are shown at different times during an invasion experiment for f_{wind}=8 Hz (a), 15 Hz (b), and 21 Hz (c). To match the profiles, I used the procedure explained in sec. 8.1.3. Note the logarithmic scale on the abscissa. As time progresses, the minimum distance of unbiased signal moves upwards as expected. Also, at higher wind speeds profiles are more biased. Recalling the dependence of refraction on water surface angle demonstrated in sec. 4.2, this is probably due to increased wave slopes.

Two conclusions can be drawn from these figures. First, to analyze the air-sided profiles in terms of structure and scaling properties down into the diffusive sublayer, data from the initial stage of an invasion experiment are best suited. Second, despite the growing bias, the outer layer ($z > 0.15\delta$) is still clearly captured even at high wind speeds and large times. This allows to estimate the surface concentration based on the value at $z = 0.15\delta$ and the scaling properties described in sec. 8.1.6.

8.2 Water-sided profile parameters

Images of the water-sided tracer distribution were recorded with the set-up described in sec. 4.3.3. Because acetone is fluorescent tracer and absorber at the same time, the observed brightness profiles depend implicitly on the unknown distribution of acetone. I explained this in detail in sec. 7.2.2. To address this issue, I used an exponential function to describe the tracer concentration profile and derived a model for the observed brightness thereof which could then be fitted to the data. The implementation along with considerations regarding correction for optical aberration were presented in sec. 7.2.3. Shortly speaking, the water-sided images yield three physical parameters, the bulk and surface concentration, c_b and c_s, respectively,

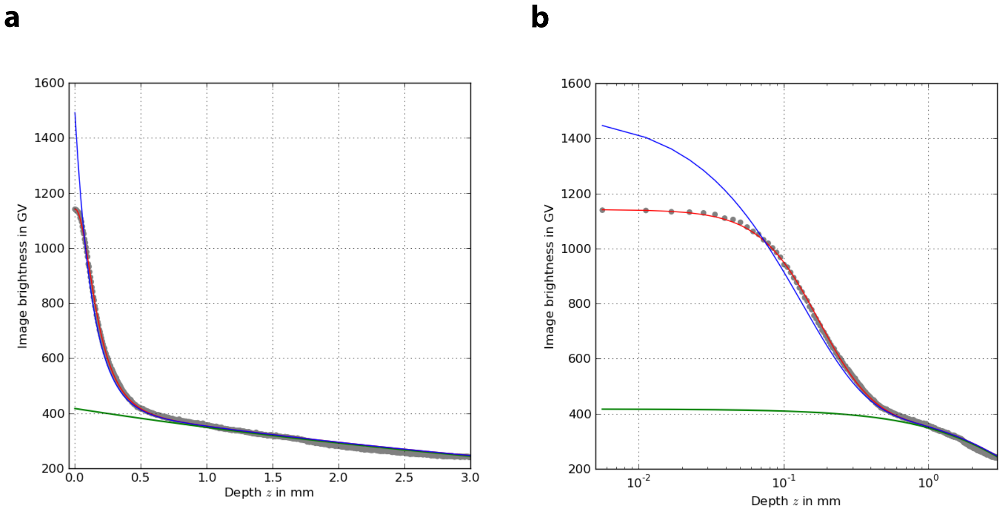

Figure 8.9: Example of a water-sided brightness profile in linear (a) and logarithmic (b) scale. Data points are shown as gray dots. Green line: fit to bulk portion of profile; red line: convolved best fit function; blue line: optically corrected best fit brightness profile.

and a scale parameter z^* characteristic for the thickness of the diffusive sublayer.

Figure 8.9 shows an example of a water-sided brightness profile for a turbine frequency of $f_{\mathrm{wind}} = 25\,\mathrm{Hz}$, in linear scale (a) and in logarithmic scale (b). Data points are depicted as gray dots. The green curve shows the fit result to the bulk portion of the profile, the red line the overall fit, convolved with a Gaussian function to correct for optical aberration, and the blue curve is the optically corrected fitted brightness profile. In general, the fit routine proved to be robust under forced invasion conditions, i.e. with continuous acetone influx. Once tracer injection was turned off, the surface concentration quickly approached the bulk value. As explained in sec. 7.2.2, for $c_s = c_b$, the fit is insensitive to the parameters c_s and z^*. Thus for this later stage during an experiment, only the bulk concentration provides sensible physical information.

8.2.1 Comparison with oxygen profiles

In the same wind-wave facility and under similar wind conditions, oxygen profiles were measured in the framework of a Bachelor thesis supervised during my PhD. For details about instrumentation and experiments, I refer to *Platt* (2011). The method has been extensively used, e.g. by *Friedl* (2013); *Herlina and Jirka* (2008); *Schulz and Janzen* (2009); *Woodrow and Duke* (2001). In short, a phosphorescent dye is mixed into the water and illuminated with a blue laser. The emitted light is quenched in the presence of oxygen and from the light attenuation, its local concentration can be retrieved. Here, Platt's averaged oxygen profiles are used for comparison with the parameters obtained in this work. This is shown in Fig. 8.10. In order to simulate the same data processing, an exponential function was fitted to the oxygen profiles and

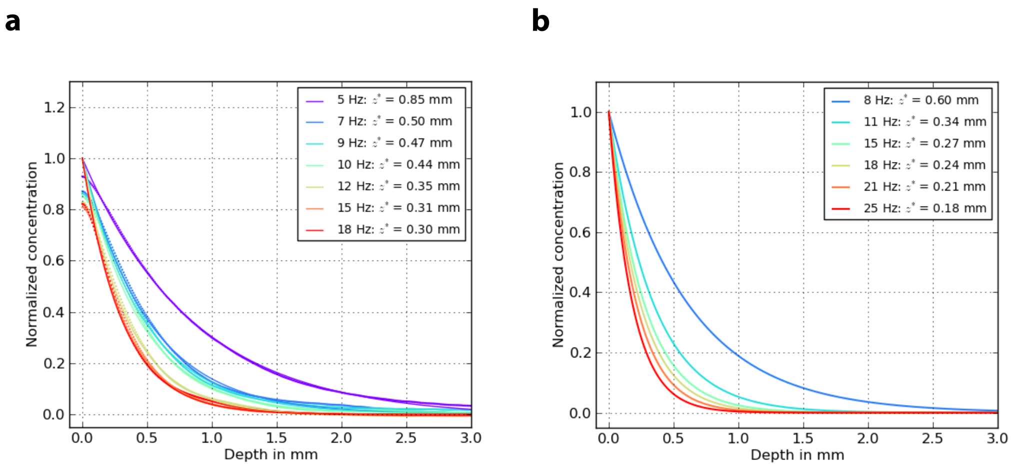

Figure 8.10: (a) Water-sided oxygen concentration profiles measured with the quenching technique described in *Platt* (2011), shown for reference. Dots are data points. Solid lines are exponential profiles fitted including optical correction. (b) Acetone profiles reconstructed based on z^*.

optical aberration was included in the same way as in this work. Note that profiles are normalized to $c_b = 0$ and $c_s = 1$. Profiles appear generally steeper for acetone, but it should be kept in mind that the exponential shape has been a-priori imposed. The precise distribution might in reality vary slightly. The effect can also be due to a different dynamical behavior of the molecules compared to oxygen. Overall agreement of the retrieved scale parameters z^* is good, however, suggesting the validity of the method used in this work.

8.2.2 Stationarity

Conceptually, the transfer resistance is introduced as a macroscopic quantity relating a concentration gradient Δc with a mass flux j given certain fluid mechanical conditions. Either based on empirical findings or theoretical models, such conditions may be described with parameters such as wind speed, friction velocity, wave slope. This has been explained in more detail in sec. 2.3. In any case, the assumption of stationarity tacitly lies at the base of the definition. In other words, given a concentration gradient, the resulting mass flux is assumed to be independent of time.

In the limiting case of pure diffusion, this is necessarily not satisfied. In fact, the diffusion equation admits only linear terms in the concentration profile under the requirement of stationarity,

$$0 \overset{!}{=} \frac{\partial c}{\partial t} = D\frac{\partial^2 c}{\partial z^2}. \tag{8.15}$$

On the other hand, a linear profile leads to $j = -D{}^{\partial c}\!/\!{}_{\partial z} \neq 0$ even at the bottom of the tank which certainly violates physically sensible boundary conditions. Generally, for pure diffusion, a concentration profile must evolve in time. *Danckwerts* (1951)

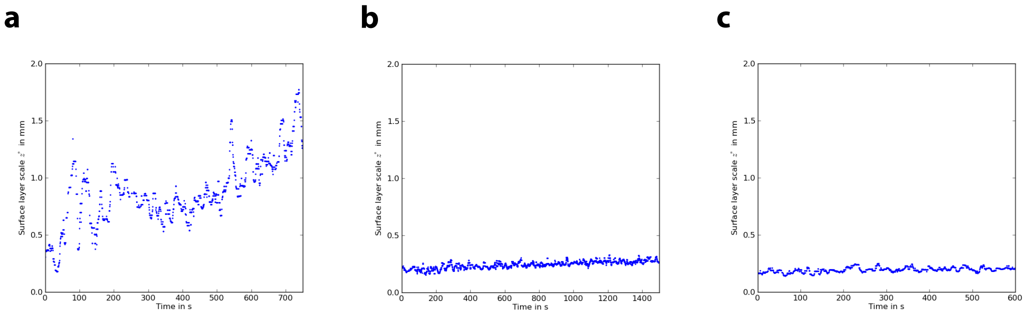

Figure 8.11: Water-sided boundary layer scale parameter z^* over time for three different wind settings, $f_{\text{wind}} = 5\,\text{Hz}$ (a), 15 Hz (b), and 21 Hz (c). For the lowest wind speed, z^* increases in time suggesting non-stationary flux conditions.

gives a solution to the above equation, e.g. assuming a constantly saturated surface and finds $c \propto \mathrm{erfc}\left({}^{z}/_{2\sqrt{Dt}}\right)$. In other words, the saturated layer grows in time and the flux decreases.

It is only in turbulent conditions, i.e. upon adding a depth dependent term $K_{\text{diff}}(z)$ to the diffusion equations, as explained in sec. 2.4.1, that a (quasi-) stationary concentration profile is possible. Experimentally, there should be a transition from purely diffusive to turbulent conditions.

This can be observed from the time evolution of the scale parameter z^*, shown in Fig. 8.11. In (a), the wind speed is very low ($f_{\text{wind}} = 5\,\text{Hz}$) causing minimal shearing of the water body. The water-sided boundary layer scale z^* constantly increases in time, characteristic for a diffusion dominated regime. Similarly, under these conditions, there is no logarithmic sublayer in the air-flow yet (see sec. 8.1.3). Panel (b) corresponds to turbulent condition in the air-sided flow ($f_{\text{wind}} = 15\,\text{Hz}$) so that water flow is expected to be turbulent to some degree due to the surface shear exerted by the wind. For (c), $f_{\text{wind}} = 21\,\text{Hz}$, waves already reach slopes of $ak \approx 0.2$ and show some skewness (see sec. 5.3) suggesting that tracer is almost homogeneously mixed into the deeper water bulk by turbulence. In good conceptual agreement, z^* grows only slightly in time in (b) and is constant in (c).

Similar complementary conclusions can be drawn from the surface concentration c_s, shown in Fig. 8.12, under modulated wind speeds (see sec. 6.2) alternating from $f_{\text{wind}} = 5\,\text{Hz}$ and 25 Hz. Acetone was injected at a constant rate of 2.2×10^{-3} mol/s. For low wind speed, the surface concentration quickly increases while the bulk concentration remains constant, implying a higher mass flux at the surface than in the lower layers. Once the wind speed is increases, turbulence and possibly wave-induced coherent flow rapidly transports tracer into the bulk, thus re-setting the surface concentration to a lower value.

The non-stationarity implies that averaged fluxes under modulated conditions not only depend on the magnitude of the parameters used to characterize flow conditions, but also on the modulation frequency T^{-1}. In the simple example above, assuming constant bulk concentrations in either phase, one can assign two characteristic

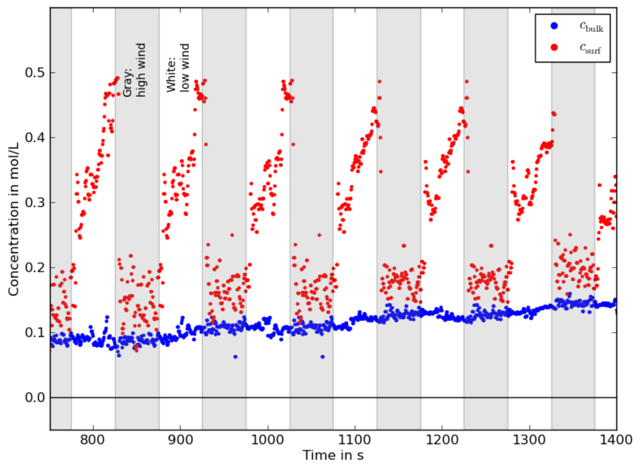

Figure 8.12
Evolution of water-sided surface (red) and bulk (blue) concentration under oscillating wind conditions. Gray shaded bars correspond to high wind ($f_{\mathrm{wind}} = 25\,\mathrm{Hz}$) and white bars to low wind ($f_{\mathrm{wind}} = 5\,\mathrm{Hz}$).

fluxes, j_1 and j_2, to the two wind speeds. If both conditions were stationary, the average flux would just be the arithmetic mean $j = (j_1 + j_2)/2$, independent of T. If instead condition 1 is non-stationary, the flux will decrease in time described by some function $f(t)$, with $f(0) = 1$. The average flux over a modulation period T is then

$$j_T = \frac{j_2}{2} + j_1 \cdot \frac{1}{T} \int_0^{T/2} f(t')\,\mathrm{d}t'. \tag{8.16}$$

In other words, the average flux does depend on the modulation frequency T^{-1} and decreases as T increases.

The tacit assumption of stationarity should be carefully considered in field studies, however, where variable wind and turbulence conditions are inevitable. It should be stated for completeness here that the above considerations also hold if turbulence is not induced by wind. Also, the reasoning is very similar to the concept of the surface renewal model by *Danckwerts* (1951), outlined in sec. 2.4, but conceptually different. The surface renewal model is an attempt to describe turbulent mixing into the water bulk based on the statistical intermittent nature of turbulence. The time scales involved are short compared to other time scales of the transport phenomenon and the result is a statistically averaged, observable transfer velocity and concentration profile. Here, the modulation period T is macroscopic and describes the transition from one statistical condition to the other.

The effect of non-stationarity is also seen in the time evolution of resistance partitioning, presented in sec. 8.4.

8.3 Absolute concentrations and full profiles

In sec. 7.1.4 and sec. 7.2.4, I explained how measured concentration profiles could be converted into absolute concentrations. As water and air-sided images were recorded simultaneously, this offers the unique possibility to match profiles across the air-water interface and to obtain timely information on the local surface-near concentrations during a gas invasion experiment.

8.3.1 Proof-of-principle

To assess the consistency of the absolute concentrations in the water, I compared the integrated amount of tracer with the known injection rate. In well-mixed conditions, the bulk concentration c_b determined from the water-sided profiles provides an estimate of the average concentration in the water compartment of the wind-wave facility. With the known volume of 23 l, the total amount N in mol at a given time t is simply $N = c_\mathrm{b} \cdot V_\mathrm{water}$. On the other hand, for a constant injection rate $\dot{N}_\mathrm{inj}$ of 2.2×10^{-3} mol/s, the injected amount of acetone is $N_\mathrm{inj} = 2.2 \times 10^{-3}\,\mathrm{mol/s} \cdot t$. The injection rate was known to about 10 % precision (see sec. 6.1.1).

In Fig. 8.13, this is shown for six exemplary wind speeds. The shaded cone indicates the approximate injected amount. The blue line reflects the amount of acetone in the water and the black curve the amount in the air (with respect to the right ordinate). For conditions (c)-(f), measured and injected amount coincide reasonably well with the given uncertainties. For low wind speed in (a) and (b), the concentrations deduced from the profiles overestimate the injected amount. This is to be attributed to the non-stationary nature of the mass transport at these low wind speeds, discussed in sec. 8.2.2. In those conditions, the tracer is not perfectly mixed throughout the full water body and concentrations are systematically higher closer to the surface in the region observed by the camera. Indeed, after injection is turned off, the estimated amount starts to drop towards the attended value as tracer is slowly mixed into the deeper bulk water. Even at higher wind speeds, a slight decrease is still visible.

A proof-of-principle of the conversion to absolute concentrations for the air-side is given in Fig. 8.14. Here, the $c_\mathrm{b}^\mathrm{water}$ was divided by the solubility α_H to yield air-equivalent value. In equilibrium, both should match which is satisfied to about 10 %. Considering the uncertainty on the solubility of acetone of similar order (see sec. 3.1.4), this seems acceptable.

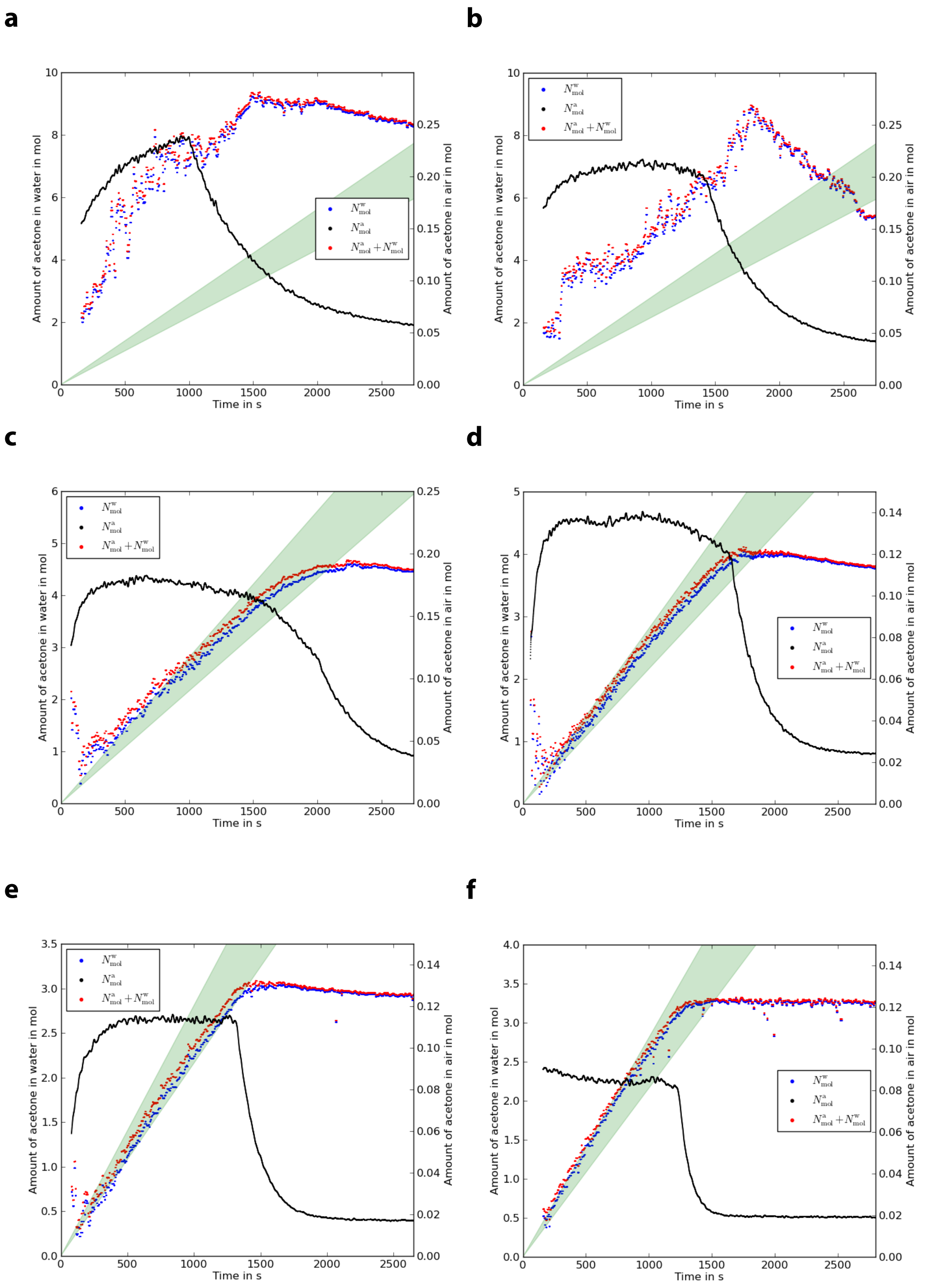

Figure 8.13: Time evolution of total amount of acetone in the air and water compartment. Calculated from bulk concentrations by multiplying with respective volume, $N = c \cdot V$. The green-shaded cone indicates the total amount estimated from the approximate acetone influx as $N = j \cdot t$. For f_{wind}=5 Hz (a) and f_{wind}=8 Hz (b), the amount of tracer in the water increases faster than expected, indicating that transport is not entirely homogeneous in depth so that tracer accumulates faster in the 20 mm beneath the surface observed by the camera than it is transported into the deeper bulk. The other four figures are for 11 Hz (c), 15 Hz (d), 18 Hz (e), and 25 Hz (f).

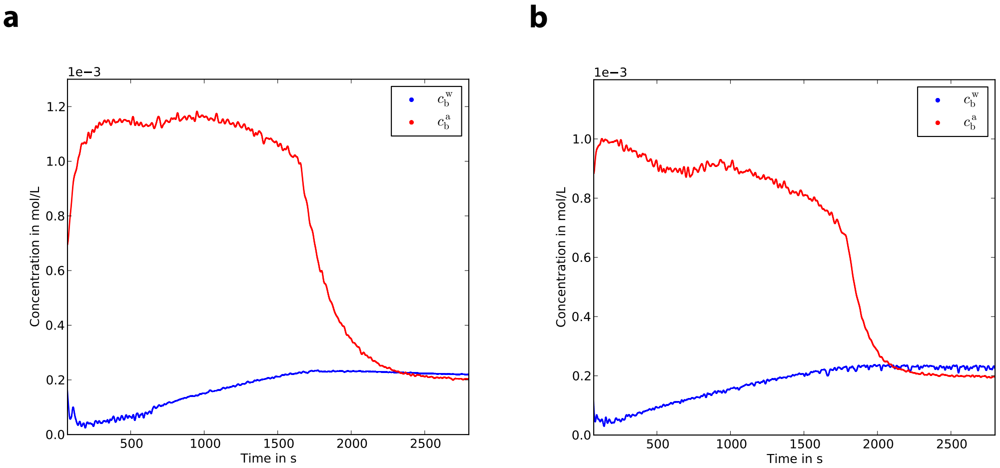

Figure 8.14: Two exemplary plots of air (red) and water-sided (blue) bulk concentrations over time. The water-sided values are divided by the solubility α_H to convert to air-equivalent concentrations. In equilibrium, both values match to about 10 %, validating the procedure to convert to absolute concentrations.

8.3.2 Matched water and air-sided profiles

By converting concentrations into absolute values and by scaling the water-sided profiles with the solubility α_H, full profiles across the air-water interface were obtained. This is shown in Fig. 8.15 for six different wind speeds. Gray dots are air-sided data points, the blue curve is the exponential model profile with experimentally determined parameters, and the red curves represent Deacon's model fitted according to the procedure described in sec. 8.1.4. For $f_{\text{wind}} = 5\,\text{Hz}$, the gradient is depicted instead, as at this low wind speed, no logarithmic sublayer exists and Deacon's profile does not describe the data (see sec. 8.1.3). The profiles are obtained by averaging data from the first three minutes of an invasion experiment.

Having in mind that concentration profiles are essentially resistance distributions, it can immediately be asserted that for acetone, both phases contribute to similar proportions to the overall resistance of the air-water boundary. This is in accordance with the estimates presented in sec. 2.5 and thereby explicitly confirms the concept of resistance partitioning across the interface. It should be noted that the reconstructed surface concentrations do not exactly match as would be expected when assuming instantaneous thermodynamic equilibrium at the phase boundary. One reason could be a systematic underestimation of the water-sided surface concentration, possibly due to insufficient optical resolution. Also, the air-sided profiles are intrinsically biased close to the surface, as explained in sec. 8.1.7. The fitted Deacon profiles compensate for this by extrapolating into the diffusive sublayer.

On the other hand, the discontinuity might have a physical reason. In particular, it might suggest that an additional interface resistance has to be taken into account. I will discuss this in detail in sec. 9.3. It should be noted that the here depicted profiles

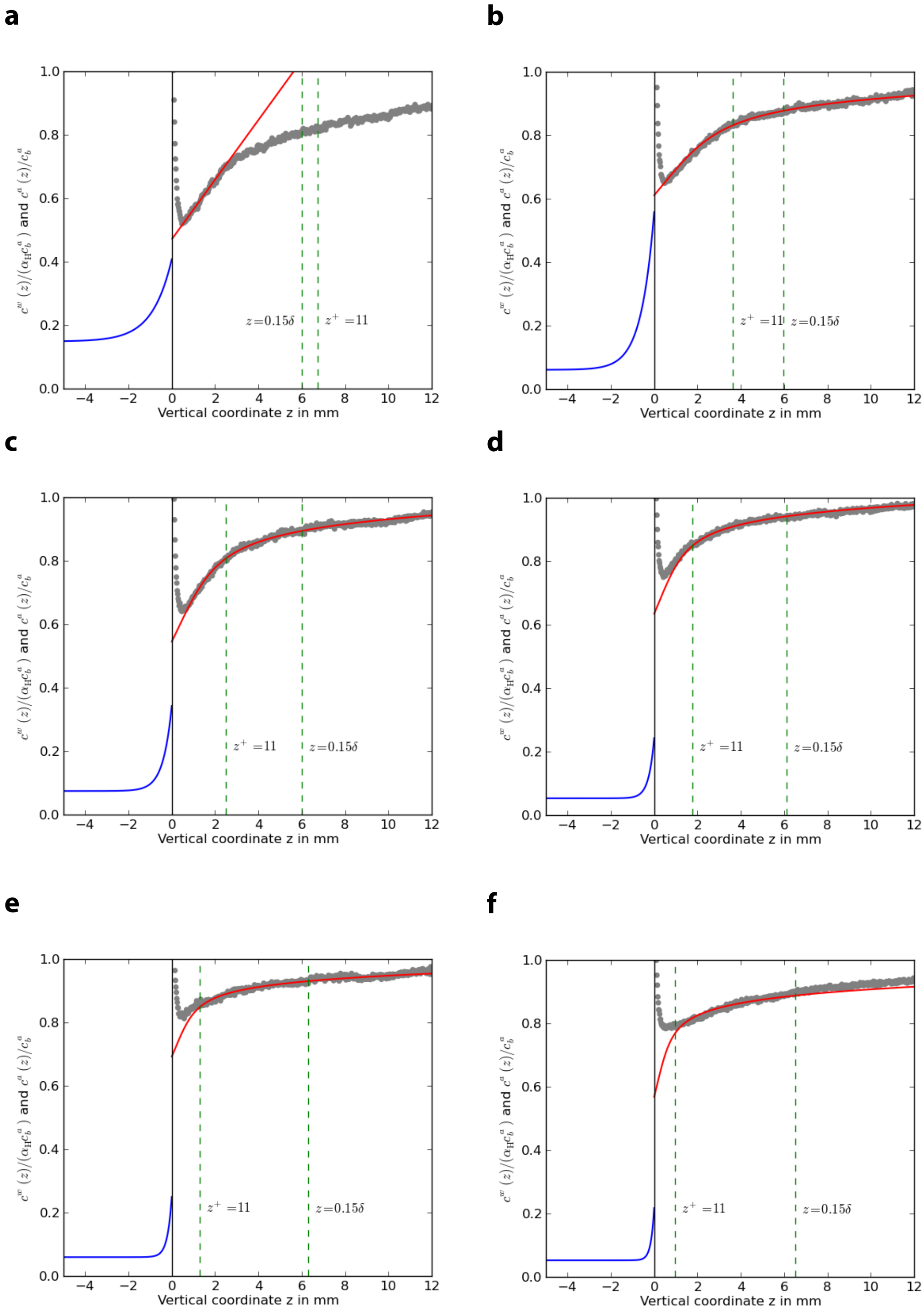

Figure 8.15: Full air-water concentration profiles for different wind speeds normalized to the air-sided bulk concentration. Air-sided data points are shown as gray dots. The red line is the fitted Deacon profile; the blue line the reconstructed water profile. Green dashed lines indicate characteristic scales in the air-sided boundary layer. Turbine frequencies are (a)-(f): 5, 8, 11, 15, 18, 21 Hz.

are normalized to the air-sided bulk concentration. Therefore, they only contain information on the relative resistance partitioning but not on the overall absolute resistance. This is instead presented in sec. 8.6.

8.3.3 Matched air and water-sided concentrations

The full matched profiles provide a unique momentary view of the tracer distribution across the air-water interface. The time evolution of absolute tracer concentrations in the bulk and at the surface is shown in Fig. 8.16 for six different wind speeds. For each data point in these time series, 20 subsequent profiles corresponding to 10 s were averaged. Water-sided bulk and surface concentration as well as air-sided bulk concentration were readily obtained from the corresponding parameters and profiles, respectively. The air-sided surface value is increasingly biased during an invasion experiment (see sec. 8.1.7). It was therefore reconstructed in the following three different ways. For the red data points, Deacon's model was fitted to the averaged profiles and c_s was determined as described in sec. 8.1.4. For the black and green lines, the scaling properties of the air-sided turbulent boundary layer were exploited. In sec. 8.1.6, I have shown that the relative resistances and concentrations at specific points within the boundary layer are in fixed relation to each other characteristic for the wind speed. For example according to Fig. 8.6, at $u_* = 13\,\mathrm{cm/s}$, $c(z = 0.15\delta) - c_\mathrm{s} = 0.8(c_\mathrm{b} - c_\mathrm{s})$ so that $c_\mathrm{s} = {}^{(c(0.15\delta)-0.8c_\mathrm{b})}/_{0.2}$, and analogously for $c(z_{11})$. Since the concentration profiles remain less affected by the water-sided brightness at $z = 0.15\delta$, especially $c(z = 0.15\delta)$ provides a relatively robust estimate of the surface concentration c_s. This latter approach relies on the scaling properties of the turbulent boundary layer in a similar way as the fit routine used in sec. 5.1 to extract u_* from wind profiles.

Figure 8.16 shows that all three methods yield consistent results compared among each other. For higher wind speeds, the value retrieved from $c(z_{11})$ is overestimated due to the brightness induced bias (see sec. 8.1.7). When tracer injection is turned off, the air-sided signal quickly starts to decay. This portion is used to calculate the total transfer resistance from mass balance considerations (see sec. 7.4). The air-sided bulk concentration assumes a roughly constant plateau value characterized by the balance of acetone influx and transport into the water. Consequently, this steady state concentration is lower for higher wind speeds, i.e. faster transport into the water. The precise value varies in time as the acetone filling in the bubbling flask (see sec. 6.1.1) decreases causing the injected air to be less saturated. The air-sided surface concentration during the exponential decay lies above the bulk values. This is because the fluorescent brightness quickly becomes dimmer while the water-sided fluorescence remains unchanged causing the bias to be relatively higher. As already seen in the profiles in sec. 8.3.2 and discussed there, c_s^a and c_s^w do not match. Generally, c_s^w is lower for increasing wind speed possibly due to a more efficient transport of acetone away from the water surface.

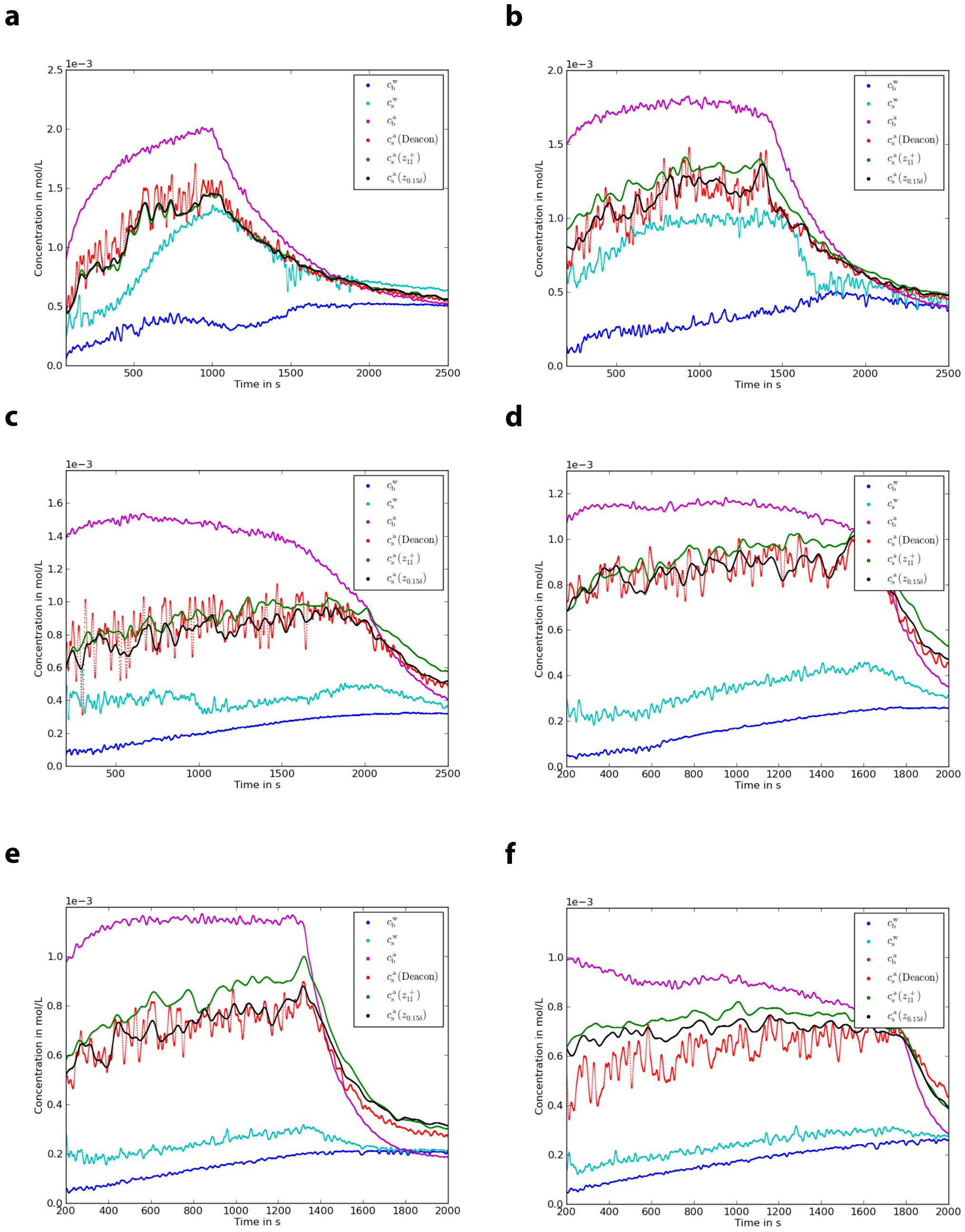

Figure 8.16: Absolute concentrations over time for different wind speeds. Water-sided values are divided by solubility α_H. Air-sided surface concentrations (red, green, black) were determined by three different methods (see text). Turbine frequencies are (a)-(f): 5, 8, 11, 15, 18, 21 Hz.

8.4 Partitioning of resistances

From the simultaneously measured absolute concentrations, the resistance partitioning across the air-water interface can be calculated. The individual contributions are given by

$$\frac{R_\mathrm{w}}{R_\mathrm{tot}} = \frac{c_\mathrm{s}^\mathrm{water} - c_\mathrm{b}^\mathrm{water}}{c_\mathrm{b}^\mathrm{air} - c_\mathrm{b}^\mathrm{water}} \tag{8.17}$$

$$\frac{R_\mathrm{a}}{R_\mathrm{tot}} = \frac{c_\mathrm{b}^\mathrm{air} - c_\mathrm{s}^\mathrm{air}}{c_\mathrm{b}^\mathrm{air} - c_\mathrm{b}^\mathrm{water}} \tag{8.18}$$

The value of $c_\mathrm{s}^\mathrm{air}$ was determined by the three methods described in the previous section. Figure 8.17 shows the relative resistances over time for different wind speeds under continuous acetone injection. The three air-sided contributions agree well, again underlining the validity of the approach. For higher wind speeds, R_a determined from the concentration at $z^+ = 11$ is affected by water-sided brightness.

For the two lowest wind speeds, the effect of non-stationarity, discussed in sec. 8.2.2, is visible. Initially, the air-sided resistance is larger, but in time the water-sided contribution grows as tracer accumulates near the surface and the flux ceases. Again, for higher wind speeds the resistances do not add up to one as expected suggesting either methodological systematics, explained in sec. 8.3.2, or an additional interface resistance, discussed in 9.3.

8.5 Surfactants

Identical invasion experiments were performed with Triton-X added to the water, as explained in sec. 6.3, to investigate the effect of surfactants on gas exchange and the partitioning of resistances. Figure 8.18 shows full, continuous concentration profiles across the air-water interface generated in the same way as for clean water. Evidently, the air-sided profiles are much less pronounced compared to their water-sided counterparts. In other words, the water-sided resistance is comparatively larger with Triton-X added to the water than in the clean case. This effect has already been observed in other studies, e.g. by *Kräuter* (2011) and *Mesarchaki et al.* (2014). Interestingly, the resistance is greater not only under energetic wind conditions, associated with the formation of waves in clean water (Fig. 8.18 d, e, f), but also for lower wind speeds. This suggests that the suppression of waves is not the principal mechanism by which surfactants affect the transfer velocities in this experiment.

It seems instead more plausible that near surface turbulence is damped by additional surface stress associated with gradients in the surface tension $\partial\sigma/\partial x$, as proposed by *Davies* (1966). In this way, surfactants modify the dynamic tangential boundary conditions, as I have explained in sec. 2.2.3. *McKenna and McGillis* (2004) have

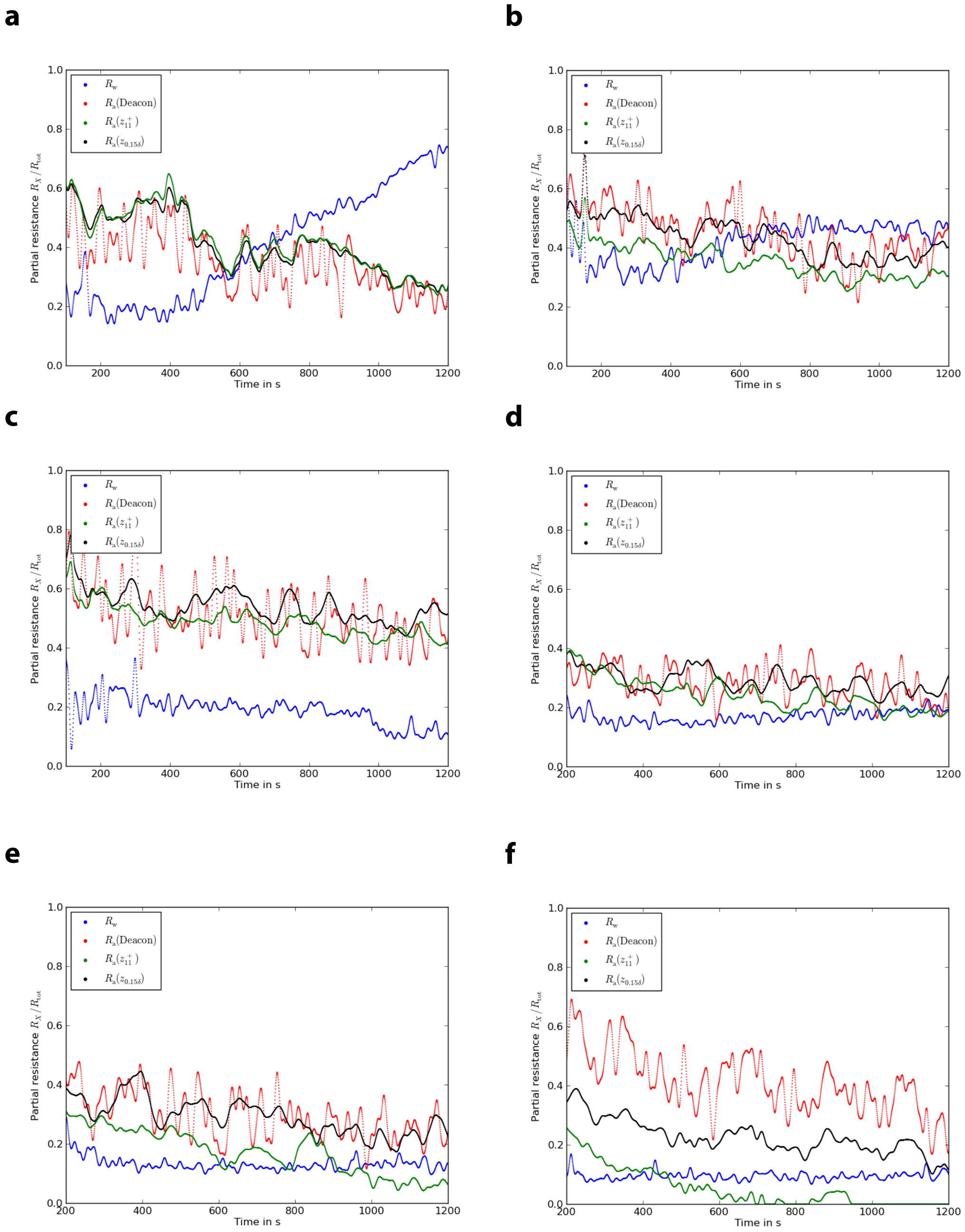

Figure 8.17: Relative contributions to the overall resistance of the air-water interface. Air-sided values (red, green, black) were determined by three different methods (see text). Note that in (a) the water-sided relative resistance grows in time due to non-stationarity (see sec. 8.2.2). Turbine frequencies are (a)-(f): 5, 8, 11, 15, 18, 21 Hz.

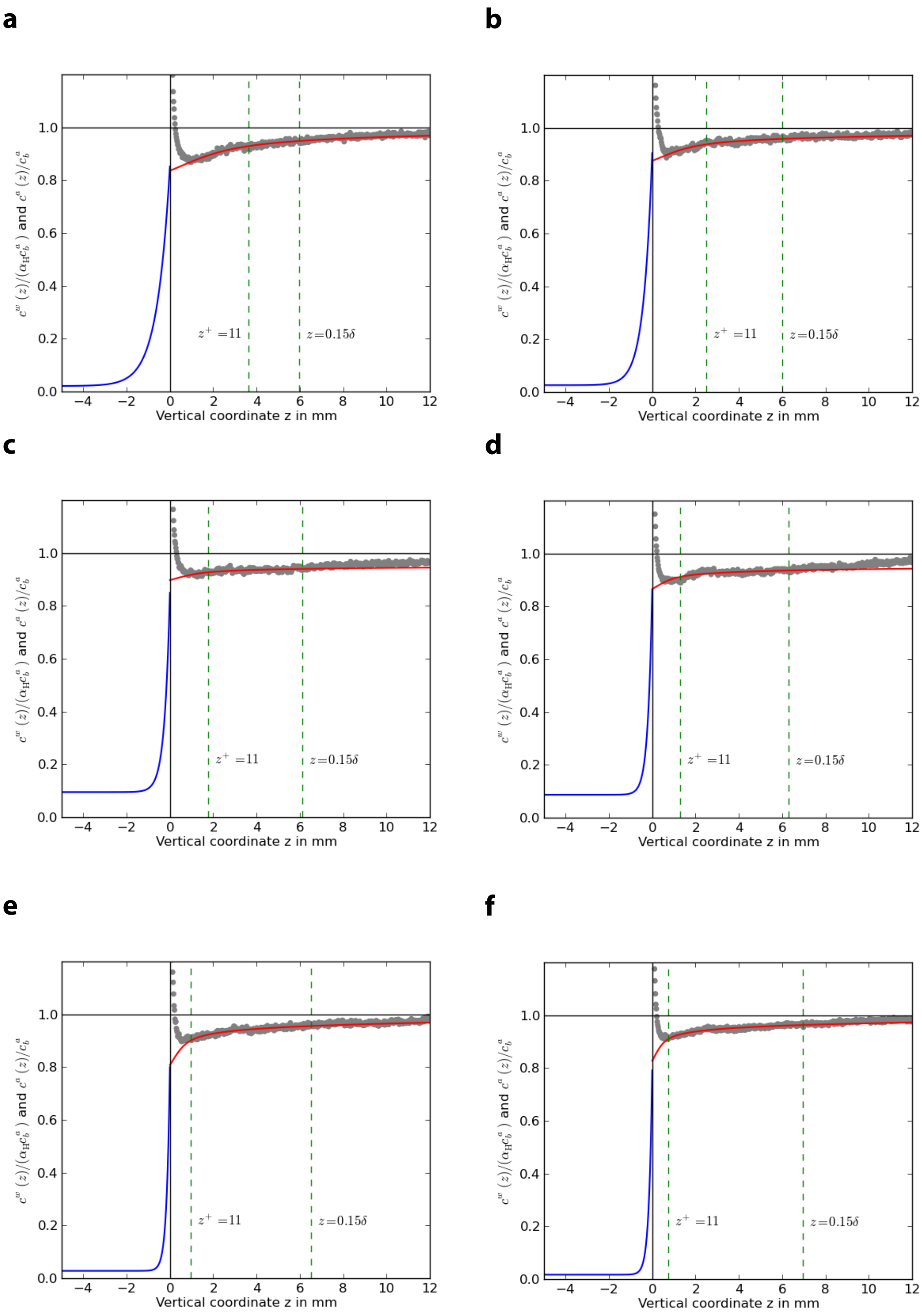

Figure 8.18: Full air-water concentration profiles for different wind speeds and Triton-X added to the water normalized to the air-sided bulk concentration. Air-sided data points are shown as gray dots. The red line is the fitted Deacon profile; the blue line the reconstructed water profile. Green dashed lines indicate characteristic scales in the air-sided boundary layer. Turbine frequencies are (a)-(f): 8, 11, 15, 18, 21, 25 Hz.

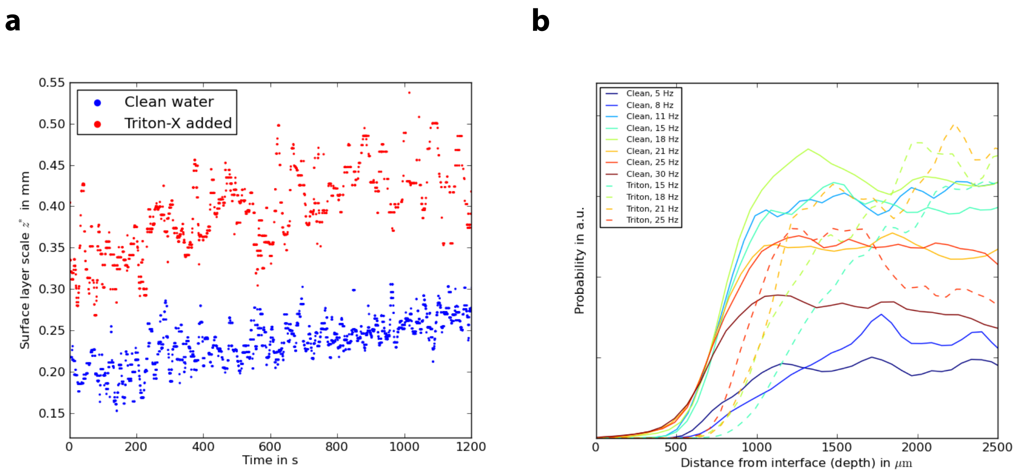

Figure 8.19: (a) Water-sided boundary layer scale parameter z^* in mm over time for clean water (blue) and Triton-X added (red). Note the stronger increase in time suggesting that non-stationarity is more pronounced with Triton-X. (b) Vertical distribution of schlieren, serving as proxy for turbulent eddies, relative to the water surface for clean water (solid) and with Triton-X (dashed).

shown experimentally that the presence of surfactants is correlated with a vanishing of surface velocity divergences. In consequence, the air-water interface resembles a rigid wall rather than a free surface, as in the clean water case. *Tsai* (1996) finds from the results of direct numerical simulations that the apparent viscous sublayer becomes thicker in the presence of surfactants and that vortices are less connected to the interface, as it frequently occurs in free turbulent flow.

In this work, no explicit flow visualization was performed. Some insight can anyhow be gained from the following observations. In Fig. 8.19 (a), a comparison of the water-sided boundary layer scale z^* as a function of time is shown for clean water (blue) and water with additional Triton-X (red), both at $f_{\text{wind}} = 15\,\text{Hz}$. For the latter case, the overall thickness is larger by about a factor of 2 which can be attributed to Tsai's observation of a wider viscous sublayer.

In sec. 7.3, I have explained how information can be gained from the water-sided images about the probability to observe streaks in a certain relative depth underneath the water surface. As such streaks reflect locally enhanced concentration fields swept away from the surface by the turbulent flow, statistically they should reflect the occurrence of eddies at a given distance from the interface. In Fig. 8.19 (b), the streak distribution is shown for different wind speeds with clean water (solid) and with Triton-X added (dashed), generated from 400 water-sided images, corresponding to 200 s. Evidently, the minimal approach distance of turbulent eddies is much larger with surfactants, supporting the simulation results of *Tsai* (1996). In both cases, eddies come closer to the surface with increasing wind speed.

Concluding, Triton-X leads to a thicker water-sided boundary layer and the suppression of turbulent eddies close to the water surface. I will discuss these aspects

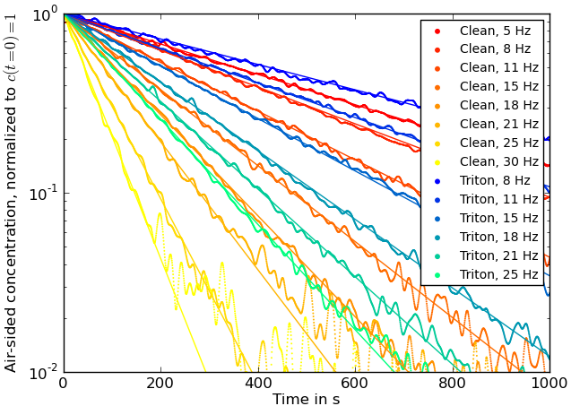

Figure 8.20
Exponential decay over time of air-sided bulk concentration for various wind speeds and surface conditions, normalized to $c(t=0)$. The straight lines indicate fit results according to the mass balance method explained in sec. 7.4.

in more detail in sec. 9.2.

8.6 Summary: Measured transfer resistances

The visualization experiments allowed to determine absolute and relative transfer resistances in various ways, as described in the previous sections of this chapter. Here, I summarize and compare the results and comment on their possible implications in chap. 9. The reported resistances are based on data averaged over 10 min of an invasion experiment under roughly constant acetone injection. It should be kept in mind that transfer velocities can be easily determined as the inverse, $k = R^{-1}$.

In Fig. 8.21, I present a comparison of (partial) resistances as a function of air-sided friction velocity u_* for clean water (a) and with Triton-X added (b). Numerical values are given for concentrations measured in the gas phase (air-equivalent, see sec. 2.5). As explained in sec. 2.3, air and water-sided resistances can be summed to supposedly yield the total resistance. They are therefore shown as stacked columns. Groups of columns are aligned with the abscissa according to their left edge.

The gray bars represent values obtained from the exponential brightness decay after acetone injection was turned off according to the mass balance method explained in sec. 7.4. They reflect the total average resistance of the air-water boundary. The exponential decay of concentrations is shown in Fig. 8.20. The volume of the air compartment of the wind-wave tank enters the mass balance fit as parameter. It sets the accuracy of the resistances to about 5 %

Red bars show the air-sided resistance derived by fitting Deacon's model to the measured concentration profiles, as explained in sec. 8.1.4. According to eq. (8.9), D, ν and u_* directly enter the formula as parameters, resulting in about 5 % uncertainty. Another 5 % uncertainty is estimated to derive from the fit procedure itself. In this context, it should also be noted that the Deacon profile assumes the diffusive sublayer to exist just like above a smooth wall. At higher wind speeds, the observed concentration profiles appeared however flatter than the model prediction sec. 8.1.3.

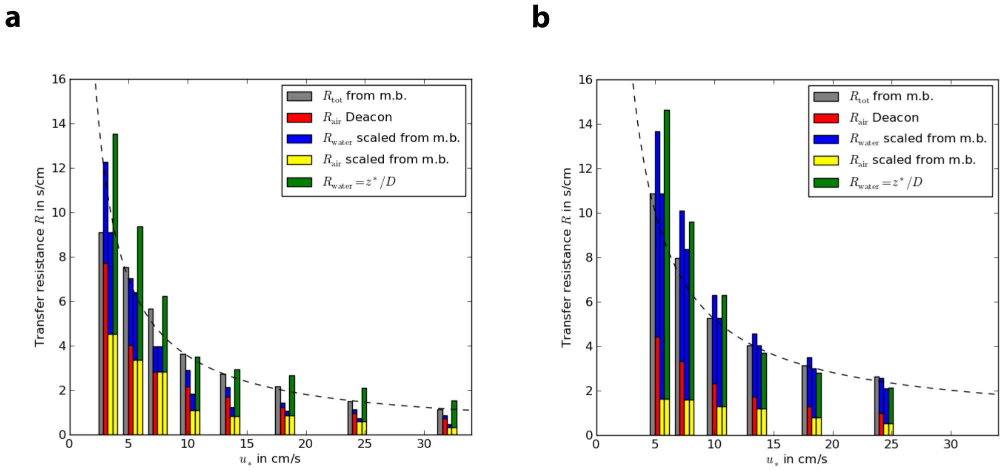

Figure 8.21: Partial and total transfer resistances determined by different methods (see text) as a function of friction velocity u_*. Groups of columns are aligned with the abscissa according to their left edge. (a) clean water and (b) with Triton-X added.

If this is not due to biased concentrations, the air-sided resistances are expected to be overestimated by 10 to 20 %. Based on the data, an affirmative or negative conclusion is not possible.

Yellow and blue bars depict the air and water-sided contribution, respectively, obtained as proportion of the mass balance value according to the partitioning described in sec. 8.4. Specifically, the partial contributions, depicted in Fig. 8.17, were multiplied with the total average resistance. For the lower wind speeds, where effects of non-stationarity had been observed, temporal average values were used. Uncertainties are difficult to estimate as they mainly depend on the unknown systematic optical errors.

Finally, the scale parameter z^* was used to provide an independent estimate of the water-sided transfer resistance. To that end, mass flux was assumed to be entirely diffusive at the surface, so that $j = -D\,{}^{\partial c}\!/\!_{\partial z}$ at $z = 0$ (cf. sec. 2.4). For the exponential profile used as model distribution, this yields $R_{\rm w} = {}^{z^*}\!/\!_{D}$ and is shown as green bars in Fig. 8.21. At low wind speeds, effects of non-stationarity were observed, causing z^* to increase in time. Again, the temporal average was used. The resistances derived from z^* are seemingly overestimated in the case of clean water. This indicates that the exponential model might not accurately reflect surface concentration gradient. Also systematic errors due to limited optical resolution cannot fully be excluded despite the adopted correction procedures. These resistances should be regarded as references only.

As expected, resistances strongly decay with increasing wind speed. The turbulent diffusivity model predicts an inverse proportionality to the friction velocity u_*. To quantify the relationship, I fitted the following reciprocal expression to $R_{\rm tot}$ exploiting the readily available parameter (u_*):

$$R_{\mathrm{tot}}(u_*) = \frac{A}{u_*} + B. \tag{8.19}$$

The resistance for the lowest wind speed was excluded as the turbulent flow is not fully developed. The fit result is shown as dashed line. The parameters are $A = 34.77$, $B = 0.066\,\mathrm{s/cm}$ for clean water, and $A = 48.0$, $B = 0.414\,\mathrm{s/cm}$ for Triton-X. The parameter B plays the role of an additive resistance as will be discussed in sec. 9.3.

With Triton-X, resistances in general are about 30 % higher than in clean water. Notably, the air-sided resistances determined by fitting Deacon's model are almost identical. This is certainly expected, at least for smooth water surface, as the turbulence in the water should not affect the air flow. In other words, surfactants influence the water-sided mass transport only. Additional observations regarding the underlying mechanism have been presented in sec. 8.5. There is some controversy about the conceptual impact of surfactants on gas exchange and about adequate parameterizations. I discuss this aspect in more detail in sec. 9.2.

Not all sums of and water-sided resistance yield the full total value recovered from the mass balance calculation. This is related to the non-matching surface concentrations described in sec. 8.3.2. If experimental systematics cannot fully account for this discrepancy, it suggests that an additional transfer resistance has to be considered equivalent in magnitude to the observed difference. This hypothesis will be discussed in sec. 9.3.

8.7 Turbulent Schmidt number

One objective of this thesis was to experimentally investigate the commonly assumed analogy between momentum and mass transport through the turbulent air boundary layer. As explained in sec. 2.4.1, this is nurtured by the near equality of kinematic viscosity and diffusion constant for many gases.

The measured air-sided acetone profiles show indeed to good precision the same scaling properties as wind profiles for the given friction velocities. In particular, the model of turbulent diffusivity by *Deacon* (1977) proved to describe the data well up to intermediate wind speeds. This also implies that rigid wall boundary conditions, which are at the base of this parametrization, are a correct description of the water surface. It should be noted, however, that for testing the analogy I assumed a-priori the turbulent Schmidt number $\mathrm{Sc}_{\mathrm{turb.}}$ to be one (see sec. 2.4.1).

For $\mathrm{Sc}_{\mathrm{turb.}} \neq 1$, the turbulent diffusivity within the logarithmic sublayer would read (see eq. (2.19))

$$K_{\mathrm{diff}}(z^+)/\nu = \mathrm{Sc}_{\mathrm{turb.}}{}^{-1}\kappa z^+, \tag{8.20}$$

and consequently the additional factor would appear in the logarithmic scaling in eq. (8.5) as

$$\bar{c}^+(z) = \mathrm{Sc}_{\mathrm{turb.}}{}^{-1}A\log(z) + B. \tag{8.21}$$

It seems tempting to explicitly determine the value of $\mathrm{Sc}_{\mathrm{turb.}}$ from the air-sided concentration profiles. However, the prefactor A also contains the acetone flux, or equivalently, the resistance. Without an independent measurement, $\mathrm{Sc}_{\mathrm{turb.}}$ can therefore not be retrieved.

A possible approach is to compare resistances calculated with the mass balance method, $R_{\mathrm{tot}}^{\mathrm{m.b.}}$ and by fitting Deacon's profile to the air-sided data $R_{\mathrm{tot}}^{\mathrm{Deacon}}$. If fetch dependence is not too strong, both methods should yield similar results, i.e. their ratio should be one. At most, the profile-derived resistances should be somewhat smaller given their local character and the general tendency that turbulent mixing becomes stronger with increasing fetch (at least not the contrary).

I explained the procedure of fitting Deacon's profile to the data in sec. 8.1.4. The air-sided resistance was retrieved from the two fit parameters according to eq. (8.9), which I restate here

$$R_{\mathrm{a}} = \frac{1-\gamma_2}{\mathrm{D}u_*\gamma_1}\nu. \tag{8.22}$$

By the partitioning across the air-water interface (see sec. 8.4), the total resistance can be obtained thereof as

$$R_{\mathrm{tot}}^{\mathrm{Deacon}} = \frac{c_{\mathrm{b}}^{\mathrm{air}} - c_{\mathrm{b}}^{\mathrm{water}}}{c_{\mathrm{b}}^{\mathrm{air}} - c_{\mathrm{s}}^{\mathrm{air}}} \cdot \frac{1-\gamma_2}{\mathrm{D}u_*\gamma_1}\nu = \frac{1 - {c_{\mathrm{b}}^{\mathrm{water}}}/{c_{\mathrm{b}}^{\mathrm{air}}}}{\mathrm{D}u_*\gamma_1}\nu, \tag{8.23}$$

with $\gamma_2 = {c_{\mathrm{s}}^{\mathrm{air}}}/{c_{\mathrm{b}}^{\mathrm{air}}}$.

Since in the initial phase of an invasion experiment the water-sided bulk concentration is still low, an approximative version of the above expression can be obtained by neglecting $c_{\mathrm{b}}^{\mathrm{water}}$. Equation (8.23) reduces to

$$R_{\mathrm{tot}}^{\mathrm{Deacon,app.}} = \frac{\nu}{\mathrm{D}u_*\gamma_1}. \tag{8.24}$$

This does not depend on the water-sided concentration and thereby reduces systematic errors.

Figure 8.22 (a) shows a comparison of total resistances, non-dimensionalized by u_*, obtained from eq. (8.23) and eq. (8.24). In particular for higher winds, where the turbulent contribution to diffusivity becomes important, the values derived from a model fit are systematically higher than the mass balance results. This trend is seen both, for the exact and the approximative formulæexcluding systematic errors in $c_{\mathrm{s}}^{\mathrm{air}}$ to be at the root of this discrepancy. Following the above argumentation, it should rather be attributed to a non-zero turbulent Schmidt number.

For clarity, I restate the integral eq. (8.2) explicitly including $\mathrm{Sc}_{\mathrm{turb.}}$,

$$c(z) - c_{\mathrm{s}} = \frac{j_{\mathrm{s}}\nu}{\mathrm{D}u_*} \cdot \int_0^{z^+} \frac{\mathrm{D}}{\mathrm{D} + \mathrm{Sc}_{\mathrm{turb.}}{}^{-1} K_{\mathrm{diff}}(z^+)} dz^+. \tag{8.25}$$

Outside the diffusive sublayer, i.e. $z^+ \gg 11$, molecular diffusion is negligible compared to turbulent mixing so that D can be omitted from the denominator and $\mathrm{Sc}_{\mathrm{turb.}}$

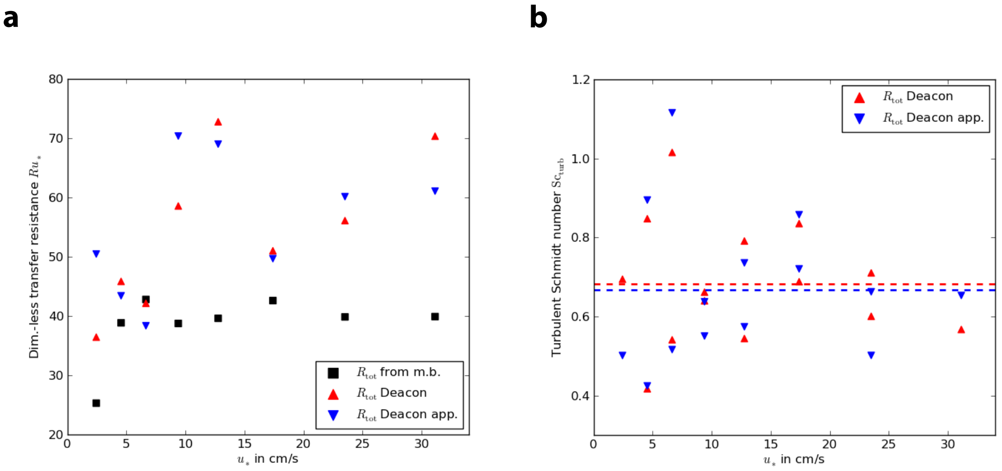

Figure 8.22: (a) Total dimensionless resistance $R_{\text{tot}}u_*$, obtain from mass balance fit (black squares), by scaling up air-sided resistances obtained from precise Deacon fit (red upwards triangles) and by approximating $c_b^w \approx 0$ (blue downwards triangles). (b) Estimate of turbulent Schmidt number $\text{Sc}_{\text{turb.}}$ obtained as ratio of resistances from mass balance and from air-sided profiles. The dashed lines indicate the average for both datasets.

can be pulled out of the integral. Consequently, the turbulent Schmidt number appears as additional factor in eq. (8.22). Therefore, the ratio of $R_{\text{tot}}^{\text{m.b.}}$ and $R_{\text{tot}}^{\text{Deacon}}$, where for the latter $\text{Sc}_{\text{turb.}} = 1$ had been used, should yield an estimate of $\text{Sc}_{\text{turb.}}$. This is shown in Fig. 8.22 (b) for the exact and approximative form of $R_{\text{tot}}^{\text{Deacon}}$. The plot does not imply any functional dependence on friction velocity, but u_* should simply be regarded as data index. Here, all values for clean water and with surfactants are used. The dashed lines indicate the average ratio, i.e. the best estimate of $\text{Sc}_{\text{turb.}}$, which is about 0.7. This is in agreement with the value mentioned by *Deacon* (1977). Scatter is considerable, but as *Monin and Yaglom* (2007) point out, experimental data on concentration profiles of passive admixture (including heat) close to a boundary are very rare and generally poor. The here obtained estimate should therefore be considered as rather valuable.

9

Discussion

Some of the experimental findings have already been discussed in the previous chapter. Here, I concentrate on three aspects which emerge from the experimental results of this work and which deserve particular attention.

9.1 Diffusive sublayer and surface roughness

Uncertainty has arisen regarding the precise shape of the diffusive sublayer for higher wind speeds. The experimental data suggest a flatter decay of acetone profiles than expected from the turbulent diffusivity model (see sec. 8.1.3). I have already discussed the influence of water-sided fluorescent brightness on the air-sided signal and this undoubtedly limits interpretation of data close to the surface. Nonetheless, it is worthwhile considering a possible physical reason for the observed discrepancy. Indeed, the turbulent diffusivity model inherits the assumption of smoothness of the boundary from the wall flow in hydrodynamics. However, wave slope measurements have shown that for the higher wind speeds in question, considerable wave steepness of $ak \approx 0.2$ occurs so that roughness may be a relevant factor influencing the near surface tracer distribution. In Fig. 9.1, I compare an estimate of the aerodynamic roughness, taken as three times the standard deviation of the wave amplitudes, with the viscous length. Intuitively, if roughness elements protrude throughout the viscous, or diffusive, sublayer they should potentially alter it. *Schlichting* (2000) gives as criterion for intermediate roughness $4\nu/u_* < h_0 < 60\nu/u_*$ for a flow over a fixed rough surface. This is met for higher wind speeds in the wind-wave tank. This treatment assumes the rough surface too be fixed.

Sullivan et al. (2000) performed DNS of turbulent airflow over an idealized sinusoidal water wave with steepness $ak = 0.1$ and $ak = 0.2$. A water wave constitutes

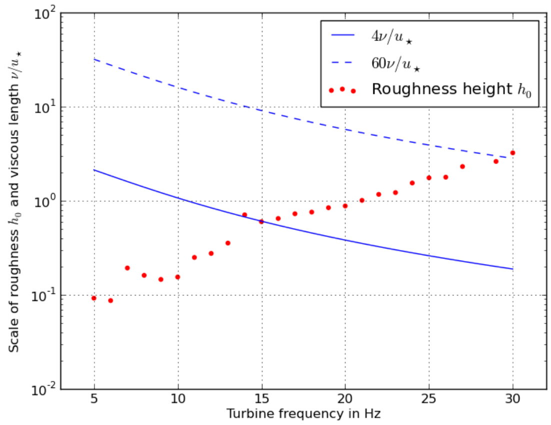

Figure 9.1
Comparison of roughness height h_0, obtained as three times the standard deviation of the wave amplitudes, with multiples of viscous length. According to *Schlichting* (2000), $^{4\nu}/_{u_*} < h_0 < ^{4\nu}/_{u_*}$ corresponds to an intermediate roughness regime.

a complicated system in that the roughness elements (the waves) move with phase velocity c while the no-slip condition matches the air-flow to the fluid surface velocity, dictated by the orbital motion underneath the waves. It is for this reason that the authors parametrize the relative motion of the rough boundary by the so-called wave-age, defined here as $^{c}/_{u_*}$. Interestingly, the viscous sublayer virtually disappears in the simulated wind profiles for $ak = 0.2$ and small, but none-zero wave age. The smallest value tested by the authors is $^{c}/_{u_*} = 3.9$, roughly corresponding to the value estimate that I obtained for the wind-wave tank (see sec. 5.2). Although results of DNS generally have to be considered with care, the possibility should not be precociously rejected that roughness due to waves have caused the observed alteration of concentration profiles for higher wind speeds on scales of the diffusive sublayer. For a decisive conclusion on this question, dedicated flow visualization experiments, e.g. PIV, are probably more suited than the here presented visualization technique.

A precise knowledge of the flow structure above small scale water waves would be of interest as this impacts the momentum dissipation, thus the dynamic interaction of the wind and wave field. This was not the scope of this thesis however. In terms of mass transfer resistance on the other hand, the possibly altered structure of the diffusive sublayer over waves is of minor significance for the following reason. The length of 120 cm of the wind-wave tank used in this work is certainly short compared to scales relevant to typical situations on the open ocean. It is also known from boundary layer theory (e.g. *Schlichting*, 2000) that the overall width δ of the turbulent boundary grows monotonously with fetch. In view of the resistance distribution within the boundary layer, verified from the experimental results, it can be concluded that the diffusive contribution to the air-sided resistance does not play any significant role. In other words, in a field measurement it would be sufficient to probe the concentration profile within the logarithmic sublayer.

9.2 Surfactants and boundary conditions

Simultaneously to concentration profiles in the air, the water-sided acetone distribution was visualized. While concentration fields were not explicitly captured, parameters describing a model profile yielded some valuable insight into the coupled mass transport through the air-water interface. Conversion to absolute concentrations allowed to match profiles at the phase boundary. While the water side alone has been observed, e.g. by *Friedl* (2013); *Herlina and Jirka* (2008); *Janzen et al.* (2010); *Jirka et al.* (2010); *Schulz and Janzen* (2009); *Woodrow and Duke* (2001), to my best knowledge this is the first time that both phases were simultaneously investigated bringing about some interesting results.

For clean water, air and water-sided boundary layer contribute to roughly equal proportions to the overall resistance as expected from the solubility of acetone of $\alpha_{\mathrm{H}} \approx 800$ (see sec. 2.5). These results explicitly confirm the conceptual model by *Liss and Slater* (1974) that resistances are partitioned across the phase boundary according to the solubility. As a tendency, the aqueous component decays more rapidly with increasing wind speed than the gaseous which is in accordance to recent mass balance based observations by *Mesarchaki et al.* (2014) and *Kräuter* (2011). Furthermore, the experiments with surfactants added to the water (Triton-X) showed a considerable increase of the water-sided resistance only, while the air-sided value, as expected, remained basically constant. This itself is no surprising discovery, obviously. Significant is the observation that surfactants affect the mass transport at any wind speed and in particular in the flat water as well as wavy regime.

Indeed, there has been disagreement (and a clear full picture is maybe still lacking) on the mechanism by which surfactants suppress gas exchange. Experimental investigations by *Jähne* (1985) *Broecker et al.* (1978) have demonstrated the enhancing effect of waves on gas exchange. Motivated by this supposition, *Frew et al.* (2004) have suggested that it is the dynamic damping of waves due to surfactants which leads to an increase of the resistance. Consequently, surfactants should attenuate gas exchange only in a regime in which waves would normally develop in clean water. This is, however, incompatible with the findings in this work (see sec. 8.5). A more consistent description is provided based on the so-called eddy-renewal model, initially proposed by *Fortescue and Pearson* (1967) and *Lamont and Scott* (1970) and elaborated by *Csanady* (1990). The conceptual idea is that turbulent eddies reach a region close to the aqueous diffusive sublayer and locally transport mass into the deeper bulk water. The sublayer is thereby momentarily thinned, leading locally to steeper surface gradients and higher fluxes. Subsequently, the diffusive sublayer is replenished from the air phase. The intermittent nature of this process motivates to picture it as random surface renewal event. It should be noted, however, that the early conceptual description of *Danckwerts* (1951), while sharing the name, does not provide a concrete renewal mechanism and is in that sense less complete. Inevitably, locally downwards pointing velocity due to an eddy is related to non-vanishing divergence and vorticity close to the surface, whose amplitude and direction is influenced by the boundary conditions. This is explained in detail in *Csanady* (1990).

Two specific cases are the free surface and rigid wall (see sec. 2.2.3). In short, the former allows eddies to reach closer to the air-water interface thereby enhancing the scalar transport. A surface active substance adds an internal tangential stress to the otherwise stress-free clean surface, the so-called Marangoni stress $\tau = {}^{\partial\sigma}\!/_{\partial x}$. Here, σ is the surface tension. If surfactants are abundant, the internal stresses can virtually immobilize the water surface, like a rigid wall. This is the mechanism which *Csanady* (1990) proposes.

McKenna and McGillis (2004) have performed PIV based visualization experiments in a grid stirred tank and found marked surface divergence and vorticity, even in the absence of waves. With surfactants added to the water, the divergences (almost) vanished and transfer velocities, measured in parallel, were significantly lower.

In my experiments, although not specifically designed for flow visualization, I could show that Triton-X leads to a systematic shift of the eddy depth distribution indicating an increase of the minimal distance to the water surface at which eddies occur (see sec. 8.5). This is in conceptual accordance with Csanady's model and the results of *McKenna and McGillis* (2004). It also agrees with the theoretical considerations of *Davies* (1966). In short, surfactants reduce surface mobility, thus causing a change of boundary conditions which suppress surface divergence and reduce the eddy renewal. As a consequence, transfer resistance increases.

It should be noted that Csanady's divergence model based on stagnation point flow yields a transfer resistance dependent on the Schmidt number as

$$R \propto \mathrm{Sc}^n, \tag{9.1}$$

with $n = {}^1\!/_2$ for a free surface (clean water) and $n = {}^2\!/_3$ for a rigid wall (strong surfactant) effect. The former corresponds to the prediction of surface renewal models (*Danckwerts*, 1951; *Fortescue and Pearson*, 1967, e.g.) and the later well reflects results of laboratory measurements of flow over solid surfaces (*Deacon*, 1981).

Depending on concentration and effectiveness of a surface active substance, the resemblance to the rigid wall case might be only approximate. To this end, *McKenna and McGillis* (2004) use Csanady's model to provide a formula which interpolates the Schmidt number exponent between the free and the rigid wall case based on the magnitude of surface stress.

It should be pointed out that the choice of n is related to the boundary condition and in this sense suited to account for effects of surfactants. On the other hand, it is conceptually independent of the geometric shape the water surface. In other words, a clean water surface is anyhow free in the above sense, be it smooth or wavy. From this point of view and from the above considerations, no change in Schmidt number exponent should be expected at the transition to a wavy regime in clean water. Laboratory measurements in wind flumes may easily lead to this erroneous conclusion, however, for the following reason. As *Jähne et al.* (1984) point out, contamination of wind-wave tanks with surface active material is a frequent issue in experimental routine. When measuring at low wind speeds, the anyhow smooth water surface makes it difficult to identify such a contamination. At stronger winds, straining forces will eventually disrupt the surfactant film and possibly wash part of it into the deeper water. In the latter case, the effectiveness of the contamination will also depend on the re-adsorption rate at the surface. In any way, the water surface becomes increasingly "free". Boundary conditions then allow for stronger surface divergence and eddy renewal, leading to enhanced transfer rates. The Schmidt number exponent is observed to shift from $2/3$ to $1/2$. It is then tempting to deduce a conceptual relationship with the onset of waves, while these merely cause the unobserved change of boundary conditions.

9.3 Additional interface resistance - a hypothesis

The full air-water concentration profiles showed a discontinuity at the water surface, particularly with clean water and for higher winds (see sec. 8.3.2). This is contrary to the assumption that at the surface concentrations obey Henry's law (see sec. 2.5). Comments regarding experimental systematics have already been made in the previous chapter. The water-sided surface concentration might be underestimated as an effect of optical aberration in the images, as discussed in sec. 7.2.5. This is in principle corrected for in the data processing routine. In the air, the brightness bias leads to an overestimation of the observed surface concentration. Likewise, fitting the Deacon profile corrects for this by effectively extrapolating the diffusive sublayer. If waves cause indeed alterations of the air-sided concentration profile, as discussed in sec. 9.1, the profile discontinuity would still be larger.

Therefore, it seems appropriate to provide a hypothesis on possible physical effects explaining the observations. If concentration profiles reflect the vertical distribution of transfer resistance (see sec. 2.3) then a gap at the surface suggests that an additional resistance has to be attributed to the interface itself.

In models describing the uptake of substances and aerosol particles by droplets, e.g. in clouds or fog, such an interface term is indeed included. A recent review on the matter can be found in *Davidovits et al.* (2006). It should be noted though that a small droplet is much different from the open water in terms of turbulence. *Woolf* (2002) has already speculated on the relevance of an interface resistance for gas exchange at the sea surface and more detailed explanations can be found therein. I will shortly outline the possible mechanisms and their implications.

Two effects can be identified regarding the surface kinetics. First, a gas molecule striking the water needs to be geometrically incorporated into the uppermost molecule layers. According to *Pollack* (1991), the opening of a surface cavity to accommodate a monomolecular gas requires energy, typically 30 times greater than the kinetic energy at room temperature. This leads to an inhibited adsorption[1]. For larger molecules such as acetone this mechanism is presumably even more pronounced. As a consequence, the effective adsorption rate $^{\mathrm{d}n}/_{\mathrm{d}t}$ is smaller than expected from ideal gas theory by a factor γ, i.e.

$$\frac{\mathrm{d}n}{\mathrm{d}t} = \gamma \frac{p}{\sqrt{2\pi m k T}}, \tag{9.2}$$

with m the mass of one molecule, p the pressure, T the temperature, and k the Boltzmann constant. Such a formulation is used, e.g. in *Knipping et al.* (2000). The factor γ is often termed mass accommodation coefficient in literature. *Pollack* (1991) conceptually relates it to the work W required for opening the surface cavity as $\gamma = \exp\left(^{-W}/_{kT}\right)$, where W however remains to be determined. In short, the mass accommodation coefficient cannot easily be deduced from first principles but needs to be determined experimentally.

The second inhibiting effect regards the mobility of a molecule very close to the interface. Woolf argues that diffusion might be different compared to the free liquid due to altered geometry and a change in intermolecular forces. The spectroscopic study by *Tarbuck and Richmond* (2006) provides evidence for modified relative orientation of molecules and the formation of complex structures in the presence of SO_2 and CO_2. *Venables and Schmuttenmaer* (2000) report changes in the hydrogen bonding environment in mixtures of water and acetone based on spectroscopic data and molecular dynamics simulations. This active field of research is certainly too ample to be discussed here, but in essence dynamical effects in the liquid on molecular scales close to the surface might be of importance.

Conceptually, both above explained mechanisms motivate the inclusion of a resistance to account for interface processes, specifically

$$R_{\mathrm{tot}} = R_{\mathrm{a}} + \frac{1}{\alpha_{\mathrm{H}}} R_{\mathrm{w}} + R_{\mathrm{IF}}. \tag{9.3}$$

Krop (2003) performed a theoretical study in the framework of linear non-equilibrium thermodynamics on the relevance of an interface resistance for describing transfer velocities. He applied his approach to data by *Liss and Slater* (1974) and found good agreement.

According to eq. (9.3), the interface process becomes increasingly relevant with enhanced transport in the two fluid compartments as forcing, e.g. by wind, increases and for higher solubility. Woolf limits his analysis to sparingly soluble gases controlled by the water side and concludes that for $\alpha_{\mathrm{H}} = 1$, γ must be of order 10^{-5} for the interface resistance to be relevant in comparison.

He uses transfer velocities of sulfur hexafluoride and chlorinated volatiles mea-

---

[1] Note that while describing a non-equlibrium process, mass accommodation is also related to equilibrium concentration ratios (*Pollack*, 1991).

sured by *Alaee et al.* (1995) and estimates the order of magnitude of the interface resistance by fitting the following expression,

$$k_{600} = \left(\frac{100}{u_*^{\mathrm{water}}} + R_{\mathrm{IF}} \right)^{-1} . \tag{9.4}$$

Note that data are scaled to Schmidt number 600, i.e. $k_{600} = (\mathrm{Sc}/600)^{1/2} k$, and are measured in the water. To convert them into air-equivalent values, the solubility α_{H} has to be multiplied (see sec. 2.5).

Depending on the dataset, Woolf finds values of 13.3 s/cm to 37 s/cm. In much the same way, the offset $B = 0.066$ s/cm which I used in eq. (8.19) also assumes the role of an interface resistance. Scaled to Schmidt number 600 and divided by α_{H}, it is $R_{\mathrm{IF}} = 50$ s/cm. Considering that the acetone is of similar size as the volatiles considered by Woolf, the agreement seems plausible.

In Fig. 8.21, a discrepancy between R_{tot} obtained from mass balance calculations and the value determined as sum of air and water-sided resistances was observed. If this difference is to be attributed to an interface resistance, it would suggest an order of 0.3 s/cm, i.e. greater than the value B obtained as offset from averaged mass balance calculations. I will comment on the comparability on local and averaged measurements further down. In any case, an interface resistance might lie at the root of the non-continuous concentration profiles.

It is worthwhile discussing briefly the relevance of an interface resistance for laboratory and field experiments. At sufficiently high turbulent mixing, one expects measured transfer velocities to level off like in the data considered by Woolf. As conditions become more energetic, an interface resistance implies an upper limit on transfer rates. Certainly, wave breaking will also set in, giving rise to an enhancement of mass transport.

In the intermediate regime, a plateau should be visible when transfer velocities are depicted relative to a forcing parameter such as U_0 or u_*. Some examples of this kind can indeed be found, notably the studies by *Asher and Wanninkhof* (1995); *Donelan and Drennan* (1995); *Komori and Shimada* (1995). For reference, I show their results in Fig. 9.2.

The most striking results are those by *Komori and Shimada* (1995) in (a, solid circles). There is a clear plateau followed by a fast incline at $U_0 \approx 10$ m/s associated with wave breaking. In the data by *Asher and Wanninkhof* (1995) in (b), white capping sets in at about $U_0 \approx 13$ m/s and the authors depict a model (solid line) supposedly accounting for it. Nonetheless, it can not be negated that data would also allow to suggest a leveling off, as qualitatively indicated by the red line. Lastly, also the plot (c, open circles) from *Donelan and Drennan* (1995) shows a similar behavior.

At the same time, other experimental findings do not suggest such a plateau so clearly. In this context, two observations should be made, similar to the argumentation presented in *Komori and Shimada* (1995). First, an interface resistance would gain relevance under stronger forcing when resistances associated with the fluid

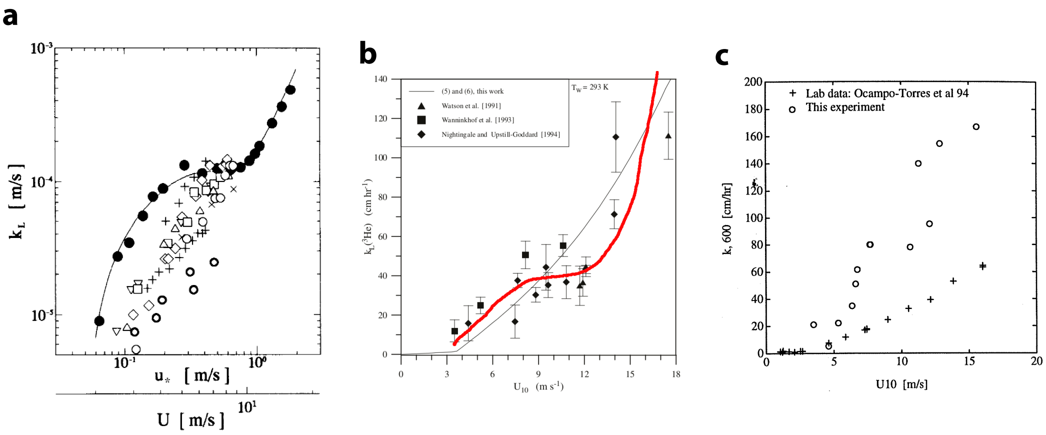

Figure 9.2: Experimental data on transfer velocities. (a) by *Komori and Shimada* (1995) for CO_2 (solid circles), (b) by *Asher and Wanninkhof* (1995) for Helium; red line indicates hypothesized qualitative dependence if interface resistance is included, and (c) by *Donelan and Drennan* (1995) for CO_2 (open circles). The plots are shown to illustrate how an interface resistance could be reconciled with experimental data, or vice versa, how the latter might even suggest such a term.

mixing decrease, as outlined above. On the other hand, waves notably grow with fetch while mass balance methods effectively yield transfer velocities averaged over the entire length of a wind-wave tank. In particular in long facilities, this might mask the existence of a plateau. Secondly, *Komori and Shimada* (1995) argues that the inhomogeneous distribution of gas in depth is source of systematic underestimation of transfer rates at low wind speeds. A conclusive answer seems difficult, but the results of this thesis are in favor of an interface resistance model.

Assuming an interface resistance entirely dominated by the adsorption process and neglecting possible reduced mobility in the water, the mass accommodation coefficient can be estimated according to eq. (9.2). Using $B = 0.066\,\mathrm{s/cm}$ as value for R_{IF}, one obtains $\gamma \approx 1.8 \times 10^{-3}$ and attributing the discontinuity in the full profiles in sec. 8.3.2 to $R_{\mathrm{IF}} \approx 0.3\,\mathrm{s/cm}$, leads to $\gamma \approx 4 \times 10^{-4}$. *Duan et al.* (1993) measured $\gamma \approx 5 \times 10^{-3}$ for the adsorption on small falling droplets. An exact quantitative comparison seems difficult, but the rough order of magnitude agreement is plausible.

Surface kinetics as possible source of resistance to gas transfer to a liquid has also come to the attention among some physical chemists. *Noyes et al.* (1992, 1996); *Rubin and Noyes* (1992) measured the uptake of gases such as CO_2 and N_2 in a small closed container about half filled with gas and half with water. Turbulence was created by mechanically stirring the water. The experimental design owed to their usual field of research. The authors observed a steady increase in gas transfer with increasing stirring rates which leveled off beyond a certain threshold before rising again once vigorous steering caused deformation and disruption of the water surface. This tendency shows surprising resemblance in particular to the data by *Komori and Shimada* (1995) described above. Assuming interface processes to contribute the only relevant resistance at high stirring rates, the authors determine $\gamma \approx 5 \times 10^{-8}$ for CO_2 and yet an order of magnitude less for N_2.

As the authors themselves admit, neglecting transport phenomena in the fluids and exclusively considering the interface process is certainly idealized and does not fully describe the underlying physics. Realistically, mass transport prescribed by the boundary layer flow in liquid and gaseous phase (depending on solubility) will contribute to resistance as well as interface dynamics. The results of my visualization experiments would reconcile such a proposition.

10

Conclusion

The scope of this thesis was the development and application of a visualization technique to study the distribution of a passive admixture in the air above the water surface. Experiments were conducted in a laboratory wind-wave tunnel. Specifically, vertical concentration profiles of a tracer gas were recorded. To this end, supersaturation in the air compartment was imposed by deliberate injection resulting in a mass flux into the water. A unidirectional wind field created shear-induced turbulence in the water and waves at sufficiently high wind speeds. Interest in this topic had arisen because of the conceptual importance of air-sided transport processes for gas exchange across the interface between atmosphere and ocean.

The developed technique is based on the principle of LIF by which molecules fluoresce when excited by laser light of a suitable wavelength. As tracer gas, acetone was selected since it met a series of required criteria. In terms of gas exchange, it is an interesting substance as the transport is controlled equally by the gaseous and aqueous phase due to its solubility. Acetone can be excited in the ultraviolet regime and emits in the blue range of the spectrum. As source of illumination, a pulsed 266 nm Nd:YAG UV laser was used pointing downwards into the wind-wave tank. The laser was formed to a sheet and spatially filtered to remove higher modes. The fluorescent brightness was observed with a camera from the cross-wind direction, i.e. perpendicular to the main air-flow. Special attention was paid to optical effects at the sidewalls of the tank and at the refracting water surface. This was important because of the weak signal originating from the air-sided fluorescence compared to the high brightness in the water.

Relative acetone concentration profiles in the air were recorded, normalized to their value in a height above the water surface where tracer was well-mixed. This was achieved by calculating quotients of images and reference images. By this approach, effects which contribute to the spatial modulation of the observed fluorescent brightness like vignetting, Lambert-Beer absorption, and marginal saturation, were automatically considered. At the same time, concentration profiles could be converted to absolute values by a calibration procedure based on the characteristic Lambert-Beer decay in the reference images. An automatic algorithm was developed which allowed to detect the water surface in individual images and to express and average profiles in coordinates relative to the water surface.

The visualization technique was extended to simultaneously obtain information on water-sided acetone profiles. A numerical approach was developed to resolve the implicit dependence of fluorescent brightness and tracer concentration. This allowed to determine the characteristic boundary layer scale z^* and the concentrations in the bulk and at the surface. In this context, correction for optical aberration was included in the data processing routines and their effectiveness was analyzed. As in the air-sided images, the position of the water surface was automatically detected with the help of dedicated image processing routines developed for this purpose. By a simple modification of the algorithm, the vertical distribution of tracer streaks was retrieved and used as proxy for turbulent eddies.

Invasion experiments were conducted in which acetone was continuously injected into the air compartment of a wind-wave tank. This caused a supersaturation in the air and thus forced a mass flux into the water. Wind speed was varied in a range from 1.5 to 6.5 m/s. To study the influence of surface active material on the gas exchange, the detergent Triton-X was added to the water in some experiments.

Measured air-sided concentration profiles were analyzed in terms of their scaling properties and good similarity to wind profiles was found. This confirms experimentally the assumed conceptual analogy between mass and momentum transport in the air. The scaling was also used to deduce the partitioning of transfer resistances within the air-sided turbulent boundary layer. Comparison with theoretical predictions showed good agreement. The turbulent diffusivity model by *Deacon* (1977) was used as a fit function to obtain air-sided transfer resistances. The influence of fluorescence originating from acetone in the water on the air-sided signal was discussed. For greater wind speeds accompanied by steeper ($ak \approx 0.2$) and asymmetric waves, the measured air-sided concentration profiles in the region of the diffusive sublayer were shallower than expected from theory for smooth wall flow. This is partially attributed to experimental systematics. DNS by other authors suggest alterations of wind profiles induced by water waves of similar amplitude as in this work (a few mm). No assertive conclusion could be reached based on the experimental data. For the dynamic interaction of wind and waves, these small scales are presumably important suggesting the use of dedicated flow field visualization in future experimental studies. Based on the resistance partitioning within the air-sided turbulent boundary layer it was concluded, however, that the diffusive sublayer does not play a major role for gas exchange, especially under field conditions.

The surfactant Triton-X was found to suppress gas exchange by about 30 % regardless of the wind speed regime. It was concluded that wave damping was not the principal causal factor as suggested previously by some other studies. The statistical distribution of acetone streaks in depth relative to the water surface showed that the presence of Triton-X was concurrent with a layer below the surface privy of turbulent eddies which was wider than in clean water. It was further concluded that surfactants lead to a transition of boundary conditions from free surface to rigid wall. This is in accordance with other theoretical and experimental studies which have identified surface divergence as a potentially relevant parameter. This suggests the complementary use of techniques to visualize the surface flow structure in future laboratory studies. These include PIV or the use of thermographic imagers.

Conversion of concentration profiles to absolute concentrations and use of the solubility α_{H} allowed to represent them as continuous distributions across the air-water interface. When normalized to the difference of air and water-sided bulk concentrations, these full profiles allowed to investigate the resistance partitioning across the phase boundary. Results generally agreed with previous studies of other authors confirming acetone to be controlled almost equally by the gaseous and aqueous phase. Normalized profiles were found not to be continuous at the water surface which was particularly evident for higher wind speeds. Systematic experimental errors were discussed as possible cause for this discrepancy. At the same time, a physical explanation for the observations was attempted. As hypothesis was proposed that an additional transfer resistance might need to be considered to account for processes at the water surface not described by fluid mechanics. Specifically, this refers to the adsorption and solvation of gas molecules at the air-water interface. A short review of existing literature on the matter was provided and selected exemplary experimental results of other authors were shown to illustrate the possible signature of an interface resistance in gas exchange data. Figures of merit based on the current results were compared with another publication and a reasonable agreement was found. The analysis supports the proposed hypothesis that additional physical process might need to be considered to fully and coherently describe gas exchange, but for an affirmative conclusion, further investigations are desirable.

List of symbols

I_{sat} Saturation laser irradiance. 29, 31

$K_{\mathrm{diff}}(z^{+})$ Turbulent contribution to vertical scalar flux. 16, 17, 74, 101, 102

$K_{\mathrm{diff}}(z)$ Turbulent contribution to vertical scalar flux. 16, 17, 73, 87, 120

$K_{\mathrm{turb}}(z^{+})$ Turbulent contribution to vertical momentum flux. 12, 13, 74

$K_{\mathrm{turb}}(z)$ Turbulent contribution to vertical momentum flux. 12, 13, 16, 120

R_{IF} Transfer resistance associated to the air water interface.. 110–112

R_{a} Transfer resistance associated to the air sided fluid.. 21, 22, 79, 95, 102, 110

R_{tot} Total transfer resistance, i.e. of air and water-sided boundary together.. 101–103

R_{w} Transfer resistance associated to the water sided fluid.. 21, 22, 95, 100, 110

U_0 Free stream air flow velocity. 12, 47, 74, 111

V_{air} Volume of the air compartment. 36, 72

V_{water} Volume of the water compartment. 36, 72, 89

Φ_{f} Quantum efficiency of fluorescence, i.e. ratio of emitted to absorbed photons.. 25–28

α_{H} Solubility (a.k.a. Partitioning coefficient) $c_{\mathrm{water}} = \alpha_{\mathrm{H}} \cdot c_{\mathrm{air}}$. 21, 26, 28, 38–40, 72, 89, 91, 94, 107, 110, 111, 117

$\langle c'w' \rangle$ Turbulent contribution to vertical scalar flux. 16

$\langle u'w' \rangle$ Turbulent contribution to vertical momentum flux. 12

$\bar{c}(z)$ Mean concentration profile. 80, 120

$\bar{c}^{+}$ Normalized mean concentration profile, $\bar{c}^{+}(z) = {}^{\bar{c}(z)}/_{c_{\mathrm{b}}}$. 73–76, 79, 101

$\bar{u}(z^{+})$ Mean velocity profile in dimensionless units. 13, 74

$\bar{u}(z)$ Mean velocity profile. 13, 74, 120

δ Width of the turbulent boundary layer.. 11, 12, 15

ϵ_{air} Optical extinction coefficient of acetone vapor, intended at $\lambda = 266\,\text{nm}$. 28, 30, 63, 64

ϵ_{water} Optical extinction coefficient of dilute acetone in water, intended at $\lambda = 266\,\text{nm}$. 28

$\frac{\partial \bar{c}}{\partial z}$ Gradient of the mean concentration profile, $\bar{c}(z)$. 16

$\frac{\partial \bar{u}}{\partial z}$ Gradient of the mean velocity profile, $\bar{u}(z)$. 12

κ Von Karman constant, typical literature values are $\kappa \approx 0.370.41$. 11, 12, 16, 101, 120

D Diffusion constant, usually in cm^2/s. 8–10, 16, 17, 19, 20, 74, 79, 99, 102, 120

Re Reynolds number, $\text{Re} \equiv {}^{UL}/_{\nu}$.. 8, 120

$\text{Sc}_{\text{turb.}}$ Turbulent Schmidt number, defined as ratio of turbulent viscosity and diffusivity, $\text{Sc}_{\text{turb.}} = {}^{K_{\text{turb}}(z)}/_{K_{\text{diff}}(z)}$. 101–103, 120

Sc Schmidt number, defined as ratio of kinematic viscosity and diffusion constant, $\text{Sc} = {}^{\nu}/_{\text{D}}$. 8, 16, 17, 108, 111, 120

${}^{c}/_{u_*}$ A parameter quantifying empirically the wave age, with c the wave's phase velocity and u_* the friction velocity.. 47

ν_{air} Kinematic viscosity of air. 17

ν_{water} Kinematic viscosity of water. 17

ν Kinematic viscosity, defined as $\nu = {}^{\mu}/_{\rho}$. 8–13, 16, 73, 74, 79, 99, 101, 102, 105, 106, 120, 121

ρ Density. 8

σ_{cs} Absorption cross section. 25, 28, 29

τ_{s} Vertical momentum flux at the surface. 11, 13, 74, 121

τ Vertical momentum flux. 13

ak Wave slope, with a the wave's amplitude and $k = {}^{2\pi}/_{\lambda}$. 49–51, 61, 87, 105, 106, 116

c_{b} Bulk concentration of the tracer.. 19–21, 32, 33, 39, 59–64, 67–70, 73, 75, 79–82, 84–86, 89, 93, 95, 102, 103, 120

c_s Surface concentration of the tracer.. 19–21, 39, 67–71, 74, 75, 79–82, 84–87, 93, 95, 102

f_laser Flash frequency of the pulsed UV laser. 29

f_wind Frequency of the wind turbine in Hz. 47, 48, 50, 51, 61, 84, 85, 87, 88, 90, 91, 98

j_s Vertical scalar flux at the surface. 17, 74, 79, 102

j Vertical scalar flux. 15, 16

n_water Refractive index of water. 39

u_* Friction velocity defined from moment flux at the boundary as $\tau_\mathrm{s} = \rho u_*^2$. 11–13, 17, 19, 39, 45–47, 66, 73, 74, 79–81, 93, 99–103, 105, 106, 111, 120, 121

z^* Characteristic scale of an exponential profile, $c(z) \propto \exp(z/z^*)$.. 20, 39, 40, 67–71, 85–87, 98, 100, 116

z^+ Dimensionless vertical coordinates $z^+ = {}^{zu_*}/_{\nu}$. 11–13, 16, 17, 73–79, 84, 95, 101, 102, 119, 120

z_{11} Scale of transition between diffusive and logarithmic sublayer, $z^+ = {}^{z_{11}u_*}/_{\nu} = 11$. 73, 76, 79, 82, 93

List of abbreviations

DNS direct numerical simulation. 3, 13, 14, 105, 106, 116

FWHM full width at half maximum. 40, 44, 50, 69–71

GV gray value. 57

ISC intersystem crossing. 24, 27

LIF laser induced fluorescence. 5, 23–26, 36, 37, 51, 66, 115

LSG laser-slope-gauge. 48

mss mean square slope. 45, 50, 51

Nd:YAG neodymium-doped yttrium aluminum garnet. 27, 36, 60, 115

PIV particle imaging velocimetry. 11, 47, 106, 108, 117

PLIF planar laser induced fluorescence. 26

QS Q-switch. 36, 52

Bibliography

Alaee, M., M. A. Donelan, and W. M. J. Strachan (1995), Wind and wave effects on mass transfer velocities of halomethanes and SF_6 measured in a gas transfer flume, in *Air-Water Gas Transfer, Selected Papers, 3rd Intern. Symp. on Air-Water Gas Transfer*, edited by B. Jähne and E. Monahan, pp. 617–626, AEON, Hanau.

Ambrose, D., C. Sprake, and R. Townsend (1974), Thermodynamic properties of organic oxygen compounds xxxiii. the vapour pressure of acetone, *The Journal of Chemical Thermodynamics*, *6*(7), 693 – 700, doi:http://dx.doi.org/10.1016/0021-9614(74)90119-0.

Asaki, T. J., D. B. Thiessen, and P. L. Marston (1995), Effect of an insoluble surfactant on capillary oscillations of bubbles in water: Observation of a maximum in the damping, *Physical Review Letters*, *75*, 2686–2689, doi:10.1103/PhysRevLett.75.2686.

Asher, W., H. Liang, C. Zappa, M. Loewen, M. Mukto, T. Litchendorf, and A. Jessup (2012), Statistics of surface divergence and their relation to air-water gas transfer velocity, *Journal of Geophysical Research*, *117*(C5), C05,035, doi:10.1029/2011JC007390.

Asher, W. E., and R. Wanninkhof (1995), The effect of breaking waves on the analysis of dual-tracer gas exchange measurements, in *Air-Water Gas Transfer, Selected Papers, 3rd Intern. Symp. on Air-Water Gas Transfer*, edited by B. Jähne and E. Monahan, pp. 517–528, AEON, Hanau.

Balschbach, G. (2000), Untersuchungen statistischer und geometrischer Eigenschaften von Windwellen und ihrer Wechselwirkung mit der wasserseitigen Grenzschicht, Dissertation, Institut für Umweltphysik, Fakultät für Physik und Astronomie, Univ. Heidelberg.

Banerjee, S., D. Lakehal, and M. Fulgosi (2004), Surface divergence models for scalar exchange between turbulent streams, *International Journal of Multiphase Flow*, *30*(7-8), 963–977, j JUL-AUG.

Benkelberg, H. J., S. Hamm, and P. Warneck (1995), Henry's law coefficients for aqueous solutions of acetone, acetaldehyde and acetonitrile, and equilibrium constants for the addition compounds of acetone and acetaldehyde with bisulfite, *Journal of Atmospheric Chemistry*, *20*, 17–34, 10.1007/BF01099916.

Betterton, E. A. (1991), The partitioning of ketones between the gas and aqueous phases, *Atmospheric Environment. Part A. General Topics*, *25*(8), 1473 – 1477, doi: 10.1016/0960-1686(91)90006-S.

Bock, E. J., T. Hara, N. M. Frew, and W. R. McGillis (1999), Relationship between air-sea gas transfer and short wind waves, *Journal of Geophysical Research-Oceans*, *104*(C11), 25,821–25,831, doi:10.1029/1999JC900200, j NOV 15.

Bopp, M. (2011), Messung der schubspannungsgeschwindigkeit am heidelberger aeolotron mittels der impulsbilanzmethode, Bachelor thesis, Institut für Umweltphysik, Fakultät für Physik und Astronomie, Univ. Heidelberg.

Breuer, G. M., and E. K. C. Lee (1971), Fluorescence decay times of cyclic ketones, acetone, and butanal in the gas phase, *The Journal of Physical Chemistry*, *75*(7), 989–990, doi:10.1021/j100677a029.

Broecker, H. C., W. Siems, and J. Petermann (1978), The influence of wind on CO_2-exchange in an wind-wave tunnel, including effect of monolayers, *Journal of Marine Research*, *36*, 595–610.

Bryant, R. A., J. M. Donbar, and J. F. Driscoll (2000), Acetone laser induced fluorescence for low pressure/low temperature flow visualization, *Experiments in Fluids*, *28*(5), 471–476, doi:10.1007/s003480050407.

Coantic, M. (1986), A model of gas transfer across air–water interfaces with capillary waves, *Journal of Geophysical Research*, *91*, 3925–3943, doi:10.1029/JC091iC03p03925.

Crimaldi, J. P. (2008), Planar laser induced fluorescence in aqueous flows, *Exp. Fluids*, pp. 44:851–863.

Csanady, G. T. (1990), The role of breaking wavelets in air-sea gas transfer, *Journal of Geophysical Research*, *95*(C1), 749–759.

Danckwerts, P. V. (1951), Significance of a liquid-film coefficients in gas absorption, *Ind. Eng. Chem.*, *43*, 1460–1467, doi:10.1021/ie50498a055.

Davidovits, P., C. E. Kolb, L. R. Williams, J. T. Jayne, and D. R. Worsnop (2006), Mass accommodation and chemical reactions at gas-liquid interfaces, *Chemical reviews*, *106*(4), 1323–1354.

Davies, J. T. (1966), The effects of surface films in damping eddies at a free surface of a turbulent liquid, *Proceedings of the Royal Society of London. Series A. Mathematical and Physical Sciences*, *290*(1423), 515–526.

de Leeuw, G., et al. (2002), LUMINY - an overview, in *Gas Transfer at Water Surfaces, Geophysical Monograph*, vol. 127, edited by E. Saltzman, M. Donelan, W. Drennan, and R. Wanninkhof, pp. 291–294, American Geophysical Union, doi:10.1029/GM127p0291.

Deacon, E. L. (1977), Gas transfer to and across an air-water interface, *Tellus*, *29*, 363–374, doi:10.1111/j.2153-3490.1977.tb00746.x.

Deacon, E. L. (1981), Sea-air gas transfer: The wind speed dependence, *Boundary-Layer Meteorology*, *21*, 31–37.

Donelan, M. A., and W. M. Drennan (1995), Direct field measurements of the flux of carbon dioxide, in *Air-Water Gas Transfer, Selected Papers, 3rd Intern. Symp. on Air-Water Gas Transfer*, edited by B. Jähne and E. Monahan, pp. 677–683, AEON, Hanau.

Donelan, M. A., and R. Wanninkhof (2002), Gas transfer at water surfaces - conepts and issues, in *Gas Transfer at Water Surfaces*, edited by M. A. Donelan, W. M. Drennan, E. S. Saltzman, and R. Wanninkhof, pp. 1–10, American Geophysical Union, doi:10.1029/GM127p0001.

Duan, S. X., J. T. Jayne, P. Davidovits, D. R. Worsnop, M. S. Zahniser, and C. E. Kolb (1993), Uptake of gas-phase acetone by water surfaces, *The Journal of Physical Chemistry*, *97*(10), 2284–2288, doi:10.1021/j100112a033.

Duke, S. R., and T. J. Hanratty (1995), Measurements of the concentration field resulting from oxygen absorption at a wavy air–water interface, in *Air-water Gas Transfer, Selected Papers from the Third International Symposium on Air-Water Gas Transfer*, edited by B. Jähne and E. C. Monahan, pp. 627–635, AEON, Hanau.

Edson, J. B., C. J. Zappa, J. A. Ware, W. R. McGillis, and J. E. Hare (2004), Scalar flux profile relationships over the open ocean, *Journal of Geophysical Research (Oceans)*, *109*, C08S09, doi:10.1029/2003JC001960.

Feigenbrugel, V., C. Loew, S. L. Calvé, and P. Mirabel (2005), Near-uv molar absorptivities of acetone, alachlor, metolachlor, diazinon and dichlorvos in aqueous solution, *Journal of Photochemistry and Photobiology A: Chemistry*, *174*(1), 76 – 81, doi:http://dx.doi.org/10.1016/j.jphotochem.2005.03.014.

Fortescue, G. E., and J. R. A. Pearson (1967), On gas absorption into a turbulent liquid, *Chemical Engineering Science*, *22*, 1163–1176.

Frew, N. M. (1997), The role of organic films in air-sea gas exchange, in *The Sea Surface and Global Change*, edited by P. S. Liss and R. A. Duce, pp. 121–171, Cambridge University Press, Cambridge,UK, 5.

Frew, N. M., J. C. Goldman, M. R. Denett, and A. S. Johnson (1990), Impact of phytoplankton-generated surfactants on air-sea gas-exchange, *Journal of Geophysical Research*, *95*(C3), 3337–3352, doi:10.1029/JC095iC03p03337.

Frew, N. M., E. J. Bock, W. R. McGillis, A. V. Karachintsev, T. Hara, T. Münsterer, and B. Jähne (1995), Variation of air–water gas transfer with wind stress and surface viscoelasticity, in *Air-water Gas Transfer, Selected Papers from the Third International Symposium on Air-Water Gas Transfer*, edited by B. Jähne and E. C. Monahan, AEON, Hanau.

Frew, N. M., et al. (2004), Air-sea gas transfer: Its dependence on wind stress, small-scale roughness, and surface films, *J. Geophys. Res.*, *109*, C08S17, doi:10.1029/2003JC002131.

Friedl, F. (2013), Investigating the transfer of oxygen at the wavy air-water interface under wind-induced turbulence, Dissertation, Institut für Umweltphysik, Fakultät für Physik und Astronomie, Univ. Heidelberg.

Gandini, A., and P. A. Hackett (1977), Electronic relaxation processes in acetone and 1,1,1-trifluoroacetone vapor and the gas phase recombination of the acetyl radical at 22.degree.c, *Journal of the American Chemical Society*, *99*(19), 6195–6205, doi:10.1021/ja00461a005.

Grossmann, T., and J. Winkelmann (2005), Ternary diffusion coefficients of glycerol + acetone + water by taylor dispersion measurements at 298.15 k, *Journal of Chemical & Engineering Data*, *50*(4), 1396–1403, doi:10.1021/je050082c.

Hama, F. R. (1954), *Boundary-layer characteristics for smooth and rough surfaces*, Society of Naval Architects and Marine Engineers, New York.

Hansen, D. A., and E. K. C. Lee (1975), Radiative and nonradiative transitions in the first excited singlet state of symmetrical methyl-substituted acetones, *The Journal of Chemical Physics*, *62*(1), 183–189, doi:http://dx.doi.org/10.1063/1.430259.

Haußecker, H., R. Shear, W. K. Melville, and B. Jähne (1995), Horizontal and vertical spatial structures of turbulence beneath short wind waves, in *IAPSO Proceedings, XXI General Assembly, Honolulu, Hawai, August 1995, PS-10 Spatial Structure of Short Ocean Waves*, 19, p. 384.

Heicklen, J. (1959), The fluorescence and phosphorescence of biacetyl vapor and acetone vapor, *Journal of the American Chemical Society*, *81*(15), 3863–3866, doi:10.1021/ja01524a017.

Herlina, I., and G. H. Jirka (2008), Experiments on gas transfer at the air–water interface induced by oscillating grid turbulence, *J. Fluid. Mech.*, *594*, 183–208, doi:10.1017/S0022112007008968.

Higbie, R. (1935), The rate of absorption of a pure gas into a still liquid during short periods of exposure, *Trans. Am. Inst. Chem. Eng.*, *31*, 365–389.

Hirsa, A., G. M. Korenowski, L. M. Logory, S. Kim, and C. D. Judd (1995), Surfactant effects on vortex flows at a free surface and the relation to interfacial gas transfer, in *Air-Water Gas Transfer, Selected Papers, 3rd Intern. Symp. on Air-Water Gas Transfer*, edited by B. Jähne and E. Monahan, pp. 649–663, AEON, Hanau.

Ho, D. T., P. Schlosser, R. W. Houghton, and T. Caplow (2006), Comparison of SF_6 and fluorescein as tracers for measuring transport processes in a large tidal river, *Journal of Environmental Engineering*, *132*(12), 1664–1668.

Ho, D. T., R. Wanninkhof, P. Schlosser, D. S. Ullman, D. Hebert, and K. F. Sullivan (2011), Toward a universal relationship between wind speed and gas exchange: Gas transfer velocities measured with 3he/sf6 during the southern ocean gas exchange experiment, *Journal of Geophysical Research*, *116*, doi:10.1029/2010JC006854.

Ho, S. Y., R. A. Gorse, and W. A. Noyes (1975), Recent work on the photochemistry of acetone in the gaseous phase, *The Journal of Physical Chemistry*, *79*(16), 1632–1634, doi:10.1021/j100583a003.

Hühnerfuss, H., W. Walter, P. Lange, and W. Alpers (1987), Attenuation of wind waves by monomolecular sea slicks and the Marangoni effect, *Journal of Geophysical Research*, *92*, 3961–3963.

Jackson, J. D. (1998), *Classical Electrodynamics*, 3rd ed., Wiley.

Janzen, J. G., H. Herlina, G. H. Jirka, H. E. Schulz, and J. S. Gulliver (2010), Estimation of mass transfer velocity based on measured turbulence parameters, *AIChE Journal*, *56*, 2005–2017, doi:10.1002/aic.12123.

Jirka, G. H., H. Herlina, and A. Niepelt (2010), Gas transfer at the air-water interface: experiments with different turbulence forcing mechanisms, *Experiments in Fluids*, *49*(1), 319–327, doi:10.1007/s00348-010-0874-4.

Jähne, B. (1985), Transfer processes across the free water interface, Habilitation thesis, Institut für Umweltphysik, Fakultät für Physik und Astronomie, Univ. Heidelberg, iUP D-200.

Jähne, B., and K. Riemer (1990), Two-dimensional wave number spectra of small-scale water surface waves, *J. Geophys. Res.*, *95*(C7), 11,531–11,646, doi:10.1029/JC095iC07p11531.

Jähne, B., W. Huber, A. Dutzi, T. Wais, and J. Ilmberger (1984), Wind/wave-tunnel experiments on the schmidt number and wave field dependence of air-water gas exchange, in *Gas transfer at water surfaces*, edited by W. Brutsaert and G. H. Jirka, pp. 303–309, Reidel, Hingham, MA.

Jähne, B., K. O. Münnich, R. Bösinger, A. Dutzi, W. Huber, and P. Libner (1987), On the parameters influencing air-water gas exchange, *J. Geophys. Res.*, *92*, 1937–1950, doi:10.1029/JC092iC02p01937.

Knipping, E. M., M. J. Lakin, K. L. Foster, P. Jungwirth, D. J. Tobias, R. B. Gerber, D. Dabdub, and B. J. Finlayson-Pitts (2000), Experiments and simulations of ion-enhanced interfacial chemistry on aqueous nacl aerosols, *Science*, *288*(5464), 301–306, doi:10.1126/science.288.5464.301.

Komori, S., and T. Shimada (1995), Gas transfer across a wind-driven air-water interface and the effects of sea water on CO_2 transfer, in *Air-Water Gas Transfer, Selected Papers, 3rd Intern. Symp. on Air-Water Gas Transfer*, edited by B. Jähne and E. Monahan, pp. 553–569, AEON, Hanau.

Krall, K. E. (2013), Laboratory investigations of air-sea gas transfer under a wide range of water surface conditions, Dissertation, Institut für Umweltphysik, Fakultät für Physik und Astronomie, Univ. Heidelberg.

Krop, H. (2003), Thermodynamic approaches for the environmental chemistry of organic pollutants, Ph.D. thesis, Universiteit van Amsterdam.

Kräuter, C. (2011), Aufteilung des transferwiderstands zwischen luft und wasser beim austausch flüchtiger substanzen mittlerer löslichkeit zwischen ozean und atmosphäre, Diplomarbeit, Institut für Umweltphysik, Fakultät für Physik und Astronomie, Univ. Heidelberg.

Kundu, P. K. (2008), *Fluid Mechanics*, 4th ed., Academic Press, Elsevier, San Diego, CA.

Lakowicz, J. R. (2006), *Principles of Fluorescence Spectroscopy*, 3. ed., Springer, doi:10.1007/978-0-387-46312-4.

Lamont, J. C., and J. C. Scott (1970), An eddy cell model of mass transfer into the surface of a turbulent liquid, *AIChE Journal*, *16*, 513–519, doi:10.1002/aic.690160403.

Lange, P. A., B. Jähne, J. Tschiersch, and I. Ilmberger (1982), Comparison between an amplitude-measuring wire and a slope-measuring laser water wave gauge, *Rev. Sci. Instrum.*, *53*(5), 651–655, doi:10.1063/1.1137036.

Lapham, G. S., D. R. Dowling, and W. W. Schultz (2001), Linear and nonlinear gravity-capillary water waves with a soluble surfactant, *Experiments in Fluids*, *30*, 448–457.

Lee, Y. H., G. T. Tsao, and P. C. Wankat (1980), Hydrodynamic effect of surfactants on gas-liquid oxygen transfer, *AIChE Journal*, *26*(6), 1008–1012, doi:10.1002/aic.690260616.

Lewis, W. K., and W. G. Whitman (1924), Principles of gas absorption, *Industrial and Engineering Chemistry*, *16*, 1215–1220, doi:10.1021/ie50180a002.

Liss, P. S. (1971), Exchange of SO_2 between the atmosphere and natural waters, *Nature*, *233*, 327–329, doi:10.1038/233327a0.

Liss, P. S., and L. Merlivat (1986), Air-sea gas exchange rates: Introduction and synthesis, in *The role of air-sea exchange in geochemical cycling*, edited by P. Buat-Menard, pp. 113–129, Reidel, Boston, MA.

Liss, P. S., and P. G. Slater (1974), Flux of gases across the air-sea interface, *Nature*, *247*, 181–184.

Lozano, A. (1992), Laser-excited luminescent tracers for planar concentration measurements in gaseous jets, Ph.d. dissertation, Department of Mechanical Engineering, Stanford University.

Lozano, A., B. Yip, and R. K. Hanson (1992), Acetone: a tracer for concentration measurements in gaseous flows by planar laser-induced fluorescence, *Experiments in Fluids*, *13*, 369–376, doi:10.1007/BF00223244.

Lucassen, J. (1982), Effect of surface-active material on the damping of gravity waves: A reappraisal, *Journal of Colloid Interface Science*, *85*, 52–58.

Lugg, G. A. (1968), Diffusion coefficients of some organic and other vapors in air, *Analytical Chemistry*, *40*(7), 1072–1077, doi:10.1021/ac60263a006.

McGillis, W. R., J. W. H. Dacey, N. M. Frew, E. J. Bock, and R. K. Nelson (2000), Water-air flux of dimethylsulfide, *Journal of Geophysical Research*, *105*, 1187–1194, doi:10.1029/1999JC900243.

McGillis, W. R., J. B. Edson, J. E. Hare, and C. W. Fairall (2001), Direct covariance air-sea CO_2 fluxes, *Journal of Geophysical Research*, *106*(C8), 16,729–16,745, doi:10.1029/2000JC000506.

McKenna, S. P., and E. J. Bock (2006), Physicochemical effects of the marine microlayer on air-sea gas transport, in *Marine Surface Films: Chemical Characteristics, Influence on Air-Sea Interactions, and Remote Sensing*, edited by M. Gade, H. Hühnerfuss, and G. M. Korenowski, pp. 77–91, Springer Berlin Heidelberg, doi:10.1007/3-540-33271-5_9.

McKenna, S. P., and W. R. McGillis (2004), The role of free-surface turbulence and surfactants in air-water gas transfer, *Int. J. Heat Mass Transfer*, *47*, 539–553, doi:10.1016/j.ijheatmasstransfer.2003.06.001.

Mesarchaki, E., F. Helleis, K. E. Krall, C. Krauter, B. Jahne, and J. Williams (2014), A universal, experimentally derived air-water transfer model for any gas under clean and surfactant covered surfaces, *Atmos. Chem. Phys.*, submitted.

Monin, A. S., and A. M. Yaglom (2007), *Statistical Fluid Mechanics, Volume I*, Dover Publications.

Münsterer, T., and B. Jähne (1998), LIF measurements of concentration profiles in the aqueous mass boundary layer, *Exp Fluids*, *25*, 190–196, doi:10.1007/s003480050223.

Niegel, D. (2013), Messung des transferwiderstands von schwefeldioxid an der luft-wasser-grenzfläche, Master's thesis, Institut für Umweltphysik, Universität Heidelberg.

Nielsen, R. (2004), Gasaustausch - entwicklung und ergebnis eines schnellen massenbilanzverfahrens zur messung der austauschparameter, Dissertation, Institut für Umweltphysik, Fakultät für Physik und Astronomie, Univ. Heidelberg.

Nightingale, P. D., P. S. Liss, and P. Schlosser (2000a), Measurements of air-sea gas transfer during an open ocean algal bloom, *Geophysical Research Letters*, *27*, 2117–2120, doi:10.1029/2000GL011541.

Nightingale, P. D., G. Malin, C. S. Law, A. J. Watson, P. S. Liss, M. I. Liddicoat, J. Boutin, and R. C. Upstill-Goddard (2000b), In situ evaluation of air-sea gas exchange parameterization using novel conservation and volatile tracers, *Glob. Biogeochem. Cycles*, *14*, 373–387, doi:10.1029/1999GB900091.

Noyes, R. M., M. B. Rubin, and P. G. Bowers (1992), An alternative model for transport of molecules between gas and solution, *The Journal of Physical Chemistry*, *96*(2), 1000–1005, doi:10.1021/j100181a083.

Noyes, R. M., M. B. Rubin, and P. G. Bowers (1996), Transport of carbon dioxide between the gas phase and water under well-stirred conditions: Rate constants and mass accommodation coefficients, *The Journal of Physical Chemistry*, *100*(10), 4167 4172, doi:10.1021/jp952382e.

Ocampo-Torres, F. J., M. A. Donelan, N. Merzi, and F. Jia (1994), Laboratory measurements of mass transfer of carbon dioxide and water vapour for smooth and rough flow conditions, *Tellus Series B Chemical and Physical Meteorology B*, *46*, 16–32, doi:10.1034/j.1600-0889.1994.00002.x.

Platt, T. (2011), Weiterentwicklung einer hochauflösenden lif-methode zur messung von sauerstoffkonzentrationsprofilen in der wasserseitigen grenzschicht, Bachelor thesis, Institut für Umweltphysik, Fakultät für Physik und Astronomie, Univ. Heidelberg, started 11.04.2011.

Pollack, G. L. (1991), Why gases dissolve in liquids, *Science*, *251*(4999), 1323–1330, doi:10.1126/science.251.4999.1323.

Reichardt, H. (1951), Vollständige Darstellung der turbulenten Geschwindigkeitsverteilung in glatten Leitungen, *Zeitschrift für angewandte Mathematik und Mechanik*, *31*, 208–219.

Rocholz, R. (2008), Spatiotemporal measurement of short wind-driven water waves, Dissertation, Institut für Umweltphysik, Fakultät für Physik und Astronomie, Univ. Heidelberg.

Roether, W. (1983), Field measurement of air-sea gas transfer: A methodical search, *Boundary-Layer Meteorology*, *27*, 97–103, doi:10.1007/BF00119974.

Rubin, M. B., and R. M. Noyes (1992), Thresholds for nucleation of bubbles of nitrogen in various solvents, *The Journal of Physical Chemistry*, *96*(2), 993–1000, doi:10.1021/j100181a082.

Schlichting, H. (2000), *Boundary Layer Theory*, 8 ed., Springer.

Schulz, H. E., and J. G. Janzen (2009), Concentration fields near air-water interfaces during interfacial mass transport: oxygen transport and random square wave analysis, *Brazilian Journal of Chemical Engineering*, *26*, 527 – 536.

Shen, J., G. S. Triantafyllou, and D. K. P. Yue (2000), Turbulent diffusion near a free surface, *J. Fluid Mech.*, *407*, 145–166.

Siddiqui, M. H. K., M. R. Loewen, C. Richardson, W. E. Asher, and A. T. Jessup (2001), Simultaneous particle image velocimetry and infrared imagery of microscale breaking waves, *Phys.Fluids*, *13*, 1891–1903.

Siddiqui, M. H. K., M. R. Loewen, C. Richardson, W. Asher, and A. T. Jessup (2002), Turbulence generated by microscale breaking waves and its influence on air-water gas transfer, *Geophysical Monograph 127, American Geophysical Union*, pp. 11–16.

Sullivan, P. P., J. C. McWilliams, and C.-H. Moeng (2000), Simulation of turbulent flow over idealized water waves, *Journal of Fluid Mechanics*, *404*, 47–85.

Takahashi, T., et al. (2009), Climatological mean and decadal change in surface ocean pco2, and net sea-air co2 flux over the global oceans, *Deep Sea Research Part II: Topical Studies in Oceanography*, *56*, 554–577, doi:doi:10.1016/j.dsr2.2008.12.009.

Tarbuck, T. L., and G. L. Richmond (2006), Adsorption and reaction of co2 and so2 at a water surface, *Journal of the American Chemical Society*, *128*(10), 3256–3267, doi:10.1021/ja057375a.

Thurber, M. C. (1999), Acetone laser-induced fluorescence for temperature and multiparameter imaging in gaseous flows, Ph.D. thesis, STANFORD UNIVERSITY.

Tober, R., R. Anderson, and O. Shemdin (1973), Laser instrument for detecting water ripple slopes, *Appl. Opt.*, *12*, 788–794.

Troitskaya, Y. I., D. A. Sergeev, O. S. Ermakova, and G. N. Balandina (2010), Statistical properties of the atmospheric turbulent boundary layer over steep surface waves, *Doklady Earth Sciences*, *433 (Part 1)*, 922 – 926.

Träger, F. (2007), *Handbook of Lasers and Optics*, Springer Verlag, doi:10.1007/978-0-387-30420-5.

Tsai, W., and L. Hung (2007), Three-dimensional modeling of small-scale processes in the upper boundary layer bounded by a dynamic ocean surface, *Journal of Geophysical Research*, *112*, C02,019, doi:10.1029/2006JC003686.

Tsai, W.-T. (1996), Impact of a surfactant on a turbulent shear layer under the air-sea interface, *Journal of Geophysical Research*, *101*, 28,557–28,568, doi:10.1029/96JC02802.

Tsai, W.-t. (2001), On the formation of streaks on wind-driven water surfaces, *Geophysical Research Letters*, *28*, 3959–3962, doi:10.1029/2001GL013190.

Tsai, W.-t., S.-m. Chen, G.-h. Lu, and C. S. Garbe (2013), Characteristics of interfacial signatures on a wind-driven gravity-capillary wave, *Journal of Geophysical Research: Oceans*, *118*(4), 1715–1735, doi:10.1002/jgrc.20145.

Venables, D. S., and C. A. Schmuttenmaer (2000), Spectroscopy and dynamics of mixtures of water with acetone, acetonitrile, and methanol, *The Journal of Chemical Physics*, *113*(24), 11,222–11,236, doi:http://dx.doi.org/10.1063/1.1328072.

Walker, J. W., and W. L. Peirson (2008), Measurement of gas transfer across wind-forced wavy air–water interfaces using laser-induced fluorescence, *Exp Fluids*, *44*, 249–259, doi:10.1007/s00348-007-0398-8.

Wanninkhof, R. (1992), Relationship between wind speed and gas exchange over the ocean, *J. Geophys. Res.*, *97*, 7373–7382, doi:10.1029/92JC00188.

Wanninkhof, R., and W. R. McGillis (1999), A cubic relationship between gas transfer and wind speed., *Geophys. Res. Lett.*, *26*, 1889–1892, doi:10.1029/1999GL900363.

Wanninkhof, R., W. E. Asher, D. T. Ho, C. Sweeney, and W. R. McGillis (2009), Advances in quantifying air-sea gas exchange and environmental forcing, *Annu. Rev. Mar. Sci.*, *1*, 213–244, doi:10.1146/annurev.marine.010908.163742.

Warken, P. (2010), Hochauflösende lif-methode zur messung von sauerstoffkonzentrationsprofilen in der wasserseitigen grenzschicht, Diplomarbeit, Institut für Umweltphysik, Fakultät für Physik und Astronomie, Univ. Heidelberg.

Winter, R. (2011), Fluorescent tracers for air-sided concentration profile measurements at the air-water interface, Dissertation, Institut für Umweltphysik, Fakultät für Physik und Astronomie, Univ. Heidelberg.

Woodrow, P. T., and S. R. Duke (2001), Laser-induced fluorescence studies of oxygen transfer across unsheared flat and wavy air–water interfaces, *Industrial and Engineering Chemical Research*, *40*(8), 1985–1995.

Woolf, D. K. (2002), Gas transfer in energetic conditions, in *Gas Transfer at Water Surfaces*, *Geophysical Monograph*, vol. 127, edited by E. Saltzman, M. Donelan, W. Drennan, and R. Wanninkhof, pp. 205–211, American Geophysical Union, doi:10.1029/GM127p0205.

Wu, J. (1989), Suppression of ripples by surfactant - spectral effects deduced from sun-glitter, wave-stuff and mircowave measurements, *J. Phys. Oceonogr.*, *19*, 238–245.

Acknowledgments

I am very grateful to Prof. Bernd Jähne for supporting me during my PhD work, financially and scientifically.

In this context, I also acknowledge funding of the German Research Foundation (DFG) through the GRK1114 Graduiertenkolleg.

I thank Prof. Kurt Roth for co-reviewing my thesis and Prof.s Ulrich Uwer and Björn Malte Schäfer for complementing the exam commission.

Many thanks also to Karin Kruljac for any support with bureaucracy.

Thanks to all my colleagues in our group for a very enjoyable and interesting time together.

Thank you in particular to Christine, Daniel, Dasha, and Felix for proof-reading parts of my thesis, and to Wolfgang for support with anything regarding framegrabbers, hardware drivers, and Co.

Doppelkeks is a miraculous drug to get you through a long night of writing. Thanks Felix for providing me with it and not only!

E grazie per innumerevoli piccole cose a chi non vuol’ essere nominata.